Cyprus University of Technology

Faculty of Engineering and Technology

Department of Mechanical Engineering and Materials Science and Engineering

Doctoral Dissertation

IN VIVO AND *IN VITRO* STUDY OF THE EFFECT OF CARDIOVASCULAR STENTING IN HEMATOLOGICAL, HEMORHEOLOGICAL AND HEMODYNAMIC PARAMETERS

Despoina Kokkinidou

Limassol, December 2025

CYPRUS UNIVERSITY OF TECHNOLOGY

FACULTY OF ENGINEERING AND TECHNOLOGY

DEPARTMENT OF MECHANICAL ENGINEERING AND MATERIALS SCIENCE AND ENGINEERING

Doctoral Dissertation

IN VIVO AND *IN* VITRO STUDY OF THE EFFECT OF CARDIOVASCULAR STENTING IN HEMATOLOGICAL, HEMORHEOLOGICAL AND HEMODYNAMIC PARAMETERS

Despoina Kokkinidou

Supervisory Committee

Dr. Efstathios Kaliviotis, Associate Professor

Dr. Andreas Anayiotos, Professor

Dr. Konstantinos Kapnisis. Special Teaching Staff

Limassol, December 2025

Approval Form

Doctoral Dissertation

IN VIVO AND IN *VITRO* STUDY OF THE EFFECT OF CARDIOVASCULAR STENTING IN HEMATOLOGICAL, HEMORHEOLOGICAL AND HEMODYNAMIC PARAMETERS

Presented by

Despoina Kokkinidou

Supervisor: Efstathios Kaliviotis, Associate Professor, Cyprus University of Technology

Signature _____

Chair of the committee: Pavlos Stephanou, Associate Professor, Cyprus University of Technology

Signature _____

Member of the committee: Aristotle Koutsiaris, Assistant Professor, University of Thessaly

Signature _____

Cyprus University of Technology

Limassol, December 2025

Copyrights

ACKNOWLEDGEMENTS

Upon completing this thesis, I would like to express my sincere gratitude to all those who have supported and contributed to this work in their own unique way.

I am deeply grateful to my supervisors, Dr. Kaliviotis, Dr. Kapnisis and Dr. Anayiotos, for their invaluable guidance, continuous support, and encouragement throughout my research journey. Their expertise, patience and understanding during challenging periods were essential to the successful completion of this work. Their profound knowledge and rich experience have inspired me both academically and personally.

I would like to express my warm thanks to M. Chrysostomou for the valuable assistance provided during the *in vitro* experiments. I would like also to thank Eleni Demosthenous for her support with the calibration of the pressure system, as well as the volunteers who kindly participated in my experiments. My sincere thanks also go to the Bioanalysis Laboratory, to Dr. Andreas Stylianou, and to Dr. Konstantia Nathanael for their help.

I would also like to thank my company for their understanding and support as I balanced my PhD studies with work commitments and a special thanks to my friend Anna for always being there for me.

Finally, I owe my deepest thanks to my husband and my family for their unwavering love, patience and encouragement. Their belief in me made this achievement possible.

ABSTRACT

Keywords: coronary artery disease, stent, blood, hematology, hemorheology

Background: Coronary artery disease is the most common type of heart disease and cause of death worldwide. Specifically, the developing plaque formation narrows the passage of the coronary arteries, leading to a decreased supply of blood, oxygen, and other vital nutrients to the heart. Cardiovascular implantation (stent) has been used as the primary solution in restoring blood flow after arterial stenosis. Despite the wide clinical usage of stents, stent functionality is compromised by complications at the site of implantation, including thrombosis and occlusion. The usage of stenting alters the local flow conditions in the artery, and the effects of these alterations on stent thrombosis and restenosis are still not fully understood. Furthermore, there is limited information on the effect of the stent presence on specific hemorheological parameters.

Objective: This study aims to investigate the effects of stent implantation on hematological, hemorheological, and hemodynamic parameters, assessing how these alterations may compromise stent functionality and circulatory physiology.

Methods: Experimental evaluations were conducted using both *in vivo* and *in vitro* approaches. *In vivo* experiments involved implanting custom-made self-expanding nitinol stents in the common carotid artery of male mice (CD1), with blood samples collected at 5- and 10-weeks post-implantation for hematological and hemorheological analysis. *In vitro* studies involved blood flow through single and overlapping stents within polymer tubes under different flow conditions and configurations, reflecting coronary artery morphologies. Commercially available stents were placed in clear perfluoroalkoxy alkane tubing connected to a syringe-pump and pressure sensing system. Hematological and hemorheological measurements, were performed using standard techniques.

Results: Stent implantation led into notable changes in hematological and hemorheological indices. Results from the *In vivo* studies demonstrated increased hematocrit and decreased RBC deformability at 10 weeks post-implantation, contributing to elevated blood viscosity, despite a slight reduction in RBC aggregation. These alterations may be linked to inflammatory responses at the implant site.

Findings from the *in vitro* investigation revealed a significant increase in RBC aggregation, particularly among female subjects, and altered blood viscosity at higher

flow rates. The influence of stenting on the *in vitro* hemodynamics was revealed in the pressure-drop across the stented region, which was found to vary, depending on the stent configuration.

Conclusions: The presence of a stent influences specific hematological, hemorheological and hemodynamic parameters, at specific flow conditions, potentially impacting long-term stent functionality. The findings underscore the need for further investigation into the physiological consequences of stent-induced hemorheological changes to optimize stent design and improve clinical outcomes.

Στον μπαμπά μου,

TABLE OF CONTENTS

ACKNOWLEDGEMENTS v

ABSTRACT vi

TABLE OF CONTENTS ix

LIST OF TABLES xiv

LIST OF FIGURES xv

LIST OF ABBREVIATIONS - Nomenclature List xix

Part I: Background and introduction 1

Chapter 1: Prologue 1

1.1 Background and motivation 1

1.2 Rationale - Aims and objectives 2

1.3 Thesis outline 3

Chapter 2: Literature review 7

2.1 Blood 7

2.2 The constituents of blood 8

2.2.1 Human blood 8

2.2.2 Animal (rodent) blood 10

2.3 Hematology in cardiovascular implantation 12

2.4 Blood rheology 13

2.4.1 Blood viscosity 13

2.4.2 RBC aggregation 15

2.4.3 RBC deformability 16

2.5 Cardiovascular diseases and cardiovascular implants 16

2.5.1 Treatment 17

2.5.2 Coronary stents 18

2.5.3 Bare metal stents 19
2.5.4 Drug eluting stents 20
2.5.5 Stent complications - failure 21
2.5.6 Stent failure - design 21
2.5.7 Stent failure - Type of stents 22
2.6 Clinical and *in vitro* studies 23
Part II: Research design and methodological approach 28
Chapter 3: *In vivo* and *in vitro* approaches 29
3.1 Ethical issues in animal study 30
3.2 Animal study licenses 31
3.3 Animals 31
3.4 Ethics permission and human participants involvement 32
3.4.1 Recruitment of participants 32
3.4.2 Blood collection from human volunteers 33
3.4.3 Testing of human blood samples 33
Chapter 4: Research methods and techniques 35
4.1 Hematology 35
4.2 Hemorheology 37
4.2.1 Viscosity 37
4.2.2 RBC aggregation 38
4.2.3 RBC deformability 39
4.3 Hemodynamics 41
4.3.1 Pressure measurements – Basic theoretical considerations 41
4.3.2 Fluidic system and set-up validation 43
PART III: *In-vivo* approach 47

Chapter 5: *In vivo* investigation on the effects of stent implantation on hematological and hemorheological parameters 47
5.1 Introduction 47
5.2 Methodology 48
5.2.1 Stent design 48
5.2.2 Animals 49
5.2.2.1 Mouse 49
5.2.3 Hematology 51
5.2.4 Hemorheology 51
5.2.5 Statistical analysis 51
5.3 Results 51
5.3.1 Hematological evaluation 51
5.3.2 Hemorheological evaluation 53
5.4 Analysis and discussion 55
Chapter 6: Inflammatory response due to stent implantation - Lymphocyte stiffness 60
6.1 Introduction 60
6.2 AFM- General principles 60
6.3 Methods 64
6.3.1 Lymphocyte isolation and culture 64
6.3.2 Atomic force microscopy (AFM) 65
6.4 Results 66
6.5 Discussion 67
PART IV: *In-vitro* approach 69
Chapter 7: Experimental evaluation of stent configuration and tube geometry on the hematological and hemorheological and hemodynamic profile of blood 69
7.1 Introduction 69

7.2 Methodology 69
7.2.1 Blood sample preparation 69
7.2.2 Stents design and tube stenting configuration 69
7.2.3 Experimental setup and procedure protocol 71
7.2.4 Experimental procedure protocol 71
7.2.5 Hematology 75
7.2.6 Hemodynamics 75
7.2.7 Hemorheology 75
7.2.8 Statistical analysis 76
7.3 Results 77
7.3.1 Hematological evaluation 77
7.3.2 Hemorheological evaluation 79
7.3.3 Hemodynamics 83
7.4 Analysis and discussion 84
7.4.1 Hemorheological parameters 85
7.4.2 Local hemodynamics 87
7.4.3 Relationships and gender differences 88
PAPT V: General Discussion, Synopsis and Conclusions 91
Chapter 8: General Discussion 91
8.1 *In vitro* observations 91
8.2 *In vivo* observations 92
8.3 Study limitations 94
Chapter 9: Conclusions and future work 95
9.1 Concluding summary 95
9.2 Future work 96

BIBLIOGRAPHY 98

APPENDIX 121

Appendix I: *In vivo*- Results 121

Appendix II: *In vivo*: Lymphocytes - Results 123

Appendix III: *In vitro*-Results 124

LIST OF TABLES

Table 4.1: Pressure sensor specifications. 43

Table 4.2: Mean pressure differences. 46

LIST OF FIGURES

Figure 2.1: Blood cells [41]. 9

Figure 2.2: Composition of blood [39]. 10

Figure 2.3: Species differences (human vs. mice): Mice arteries are about 15 times smaller than human arteries, resulting in WSR values approximately 15 times higher in mice than in humans [43]..... 11

Figure 2.4: Viscosity and shear rate of blood using different models: Power law, Casson model and rotating viscometer [49]. 14

Figure 2.5: Red blood cells, Rouleaux formation [52]. 15

Figure 2.6: Coronary stent implantations per million people across countries in 2016. France had the highest rate (4,075 per million) and Egypt had the lowest (1,165 per million). Data: European Society of Cardiology (2023) [60]. 18

Figure 2.7: Stenting procedure [59]. 19

Figure 2.8: A: The stent is mounted on a balloon catheter and guided to the narrowed, diseased section of the coronary artery; B: The balloon is inflated, expanding the stent and opening the constricted artery segment; C: After deflating the balloon and removing it, the stent remains embedded in the artery wall. Drug-eluting stents release medication to lower the risk of restenosis, or re-narrowing of the artery [61]. 20

Figure 2.9: Hematocrit, plasma fibrinogen, plasma and whole blood viscosity after intervention (†$p < 0.05$, ††$p < 0.01$, ∗$p < 0.005$, ∗∗$p < 0.001$, ∗∗∗$p < 0.0001$) [85]. 24

Figure 2.10: Coronary stents decorated by Heparin/NONOate nanoparticles [88]. 26

Figure 4.1: Flowcytometry using a semi-conductor laser [97]. 36

Figure 4.2: The underlying working principle of a flow cytometer [99]. 37

Figure 4.3: Schematic representation of diffuse light scattering used to assess red blood cell (RBC) aggregation parameters, including the aggregation index (AI) and characteristic aggregation time (T1/2). The experimental microchip utilized for RBC aggregation measurements is shown, along with its schematic layout. The kinetics curve of RBC spontaneous aggregation, obtained with the RheoScan AnD-300, illustrates key aggregation parameters: Imax, the forward scattered light intensity at maximum RBC

aggregation; AI, the aggregation index, defined as the ratio of RBCs participating in aggregation during the first 10 seconds of measurement relative to the total number of cells [103,104]. 39

Figure 4.4: Microfluidic chip (right) used for vacuum-driven shearing of a thin layer of RBC suspension under varying pressures, inducing deformation of cells into an ellipsoidal shape [105]. 41

Figure 4.5: Pressure against time for a Newtonian fluid case. 42

Figure 4.6: Microfluidic pressure sensor και flow controller (Elveflow) [108]. 44

Figure 4.7: A diagrammatic representation of the system configuration with a microfluidic pressure sensor (not drawn to scale). 44

Figure 4.8: Collective averaged pressure differences plotted against all flow conditions and for the two flow configurations [109]. 45

Figure 5.1 Representative SEM images of the stent device indicating: (A) The closed-cell design with a diamond-shaped pattern (at x60 mag); Representative surface morphology of (B) the HT and (C) the EP stent (both at x1200 mag). 49

Figure 5.2: Schematic illustration of the experimental design. Overview of the stenting surgical procedure at day 0, the whole blood sampling at day 35 and 70 (5- and 10-weeks post-implantation respectively) and the hematological and hemorheological evaluation 2 hours after blood collection. 50

Figure 5.3: Effect of time-course stenting on hematological parameters. Values are expressed as the mean ± SD and the physiological range is indicated with gray-lined boxes. 53

Figure 5.4: Stent-induced alterations in RBC aggregation and deformability. 54

Figure 5.5: Normalised viscosity η* against shear rate. Control samples in comparison with the stented cases at two different time points. 55

Figure 6.1: Schematic representation of lymphocyte isolation protocol using the RosetteSep™ protocol and the SepMate™ method. 65

Figure 6.2: Lymphocyte elasticity expressed in Young's modulus values (kPa). (A) Control vs stented ApoE and CD1 mice (same day and 24 h after isolation). (B, C) Mid

stage (4W) vs late stage (8W) stented CD1 mice, same and next day measurements, respectively (* indicates $p < 0.05$). 67

Figure 7.1: Stent images in curved geometry. (A) single stented case included a Boston Scientific stent PROMUS Element platinum-chromium (PtCr). (B) Overlapping case using two stents with similar geometry and cell dimensions: a Boston Scientific PROMUS Element stent and an Abbott Xience PRIME cobalt–chromium (CoCr) stent. 70

Figure 7.2: Schematic illustration of the experimental design. Experimental cases include setups for: a) straight non-stented case, b) curved non-stented case, c) single stented straight case, d) single stented curved case, e) overlapped stents in a straight tube, and f) overlapped stents in a curved tube. 72

Figure 7.3: Schematic diagram of the experimental protocol of the low exposure case. 74

Figure 7.4: Effect of stenting on various hematological parameters for the different experimental setups and the different exposure regimes. a) RBC count, b) Hematocrit, d) RBC width distribution, and d) Mean corpuscular volume. Values are expressed as the mean ± SD. The physiological range for each parameter is indicated by the red dashed lines. 78

Figure 7.5: Effect of different exposure conditions (baseline vs high- exposure) in RBC deformability and aggregation. 80

Figure 7.6: Effect of stent and geometry for the high-exposure conditions in RBC deformability (panel a) and aggregation (panel c). The physiological values for each parameter are indicated by the red dashed lines. Panel b: Images of the diffraction pattern resulted from the deformed RBCs at comparable shear stresses (2.89 and 3.11 Pa) for the Control Straight (top image) and the Overlapped Curved (bottom image). In green colour the expected physiological elliptical pattern for the specific stresses. The percent differences from the physiological pattern are given as the difference in the ellipse area for each case. Panel d): AI index for the female population of the study (* for $p<0.05$; two-way ANOVA). 81

Figure 7.7: Viscosity alterations η* in single stented and overlapped cases. 83

Figure 7.8: Mean Pressure ΔP from all volunteers for every stent configuration. (*** for p<0.001; **** for p<0.0001; one-way ANOVA). 84

Figure 7.9: Correlation analysis. (a) Correlation between the stent-induced pressure-drop (ΔP*) and the measured viscosity (η*) of blood samples at a shear rate of 15.82 s^{-1} in the overall population. (b) Correlation between ΔP* and η* in the female group. (c) Correlation between ΔP* and aggregation index (AI) in females and (d) Correlation between ΔP* and AI in males. 89

LIST OF ABBREVIATIONS - Nomenclature List

Abbreviations	
AFM	Atomic Force Microscopy
AI	Aggregation Index
AMP	Amplitude of aggregation
BASO	Basophils
BMS	Bare metal stents
CFD	Computational Fluid Dynamics
CVD	Cardiovascular Disease
D	Diameter
DES	Drug Eluting Stents
DW	Distilled water
EC	Endothelial Cell
EI	Elongation index
EOS	Eosinophils
EP	Electropolished
ESI	Elveflow Software Interface
FSC	Forward Scatter
GL12	Glycerin/water solution (11.89 cP)
GL4	Glycerin/water solution (4 cP)
HCT	Hematocrit
HGB	Hemoglobin
HT	Heat-Treated
IL-6	Interleukin-6
ISR	In-Stent Restenosis
LYMPH	Lymphocytes
MCH	mean cell hemoglobin
MCV	Mean Cell Volume
MONO	Monocytes
MPS3	Microfluidic pressure sensor
NEU	Neutrophils
NO	Nitric Oxide
OB1	Microfluidic controller
P	Pressure
PLT	Platelets

PMTs	Photomultiplier Tubes
Q	Flow rate
r	Radius
RBC	Red Blood Cell
RDW-CV	Red Cell Distribution Width – Coefficient of Variation
RDW-SD	Red Cell Distribution Width – Standard Deviation
Re	Reynolds number
SD	Standard Deviation
SEM	Scanning Electron Microscopy
SS	Shear Stress
SSC	Side Scatter
TEM	Transmission Electron Microscopy
WBC	White blood cell
WSS	Wall shear stress
XG	Xanthan gum/water solution
ΔP	Total average pressure difference
η	Viscosity

Part I: Background and introduction

Chapter 1: Prologue

1.1 Background and motivation

Cardiovascular disease remains one of the most common causes of mortality and morbidity in the world [1–4]. Effects of heart disease usually are poor blood circulation, angina pectoris, lack of oxygen and can also cause myocardial infarction [5]. The cardiovascular stent is the conventional medical device for treating arterial stenosis [6–8]. However, the stenting effectiveness is undermined by complications such as delayed endothelization, early and late thrombosis, and in-stent restenosis (ISR) [9–12].

New generation designs and types of stents have been developed and are available for clinical applications, but the aforementioned complications after implantation are still in many cases a major limitation, influencing the effectiveness of the treatment [6,9,11,13–17]. Many stent types with different mechanical and biochemical characteristics have been developed to modulate the inflammatory reaction, which has been identified as a cause of complications after stent implantation [6]. Vascular and circulating white blood cells also play an important part in post-stenting complications, as they react to the mechanical and biochemical stimuli induced by physicochemical interactions with the stent's surface. Experimental *in vitro* and clinical evidence suggests that changes in the arterial biomechanochemical environment due to stent implantation are the main causes of the initiation of thrombosis and restenosis [18–20]. Therefore, implanted materials, such as stents, must possess specific characteristics that allow them to integrate seamlessly into the target tissue without causing an excessive foreign body reaction [21]. The most commonly used surface treatment method for minimizing post-implantation complications is electropolishing [22–24] however, additional research is necessary to clarify the effectiveness of the particular treatment [23]. In a recent work by Kapnisis et al [25], electropolished and surface-modified devices were evaluated in a mouse stent implantation model. Stent-induced and biocorrosion-related alterations were identified in the nanostructure, cytoskeleton, and mechanical properties of

circulating lymphocytes and it was demonstrated that stent surface wear and metal particle contamination affect the peri-implant inflammatory response. While the latest generation of drug-eluting stents (DES) has drastically reduced the occurrence of early-stage ISR, through inhibition of cell proliferation, extended late-phase in-stent restenosis has been reported [26–28]. Incomplete or delayed stent endothelialisation, caused by drugs like sirolimus and paclitaxel, affects local flow conditions and thereby the RBC profile and blood rheological properties [29,30].

The new generation of stents has decreased the possibility of complications after implantation, but the limited effectiveness of the implant is still present [31,32]. It is well known that hematologic parameters are affected by diseases and play an important role as markers in human and veterinary medicine. Mice models are suitable and are used for human-related research to find solutions to biological questions [33]. Over the years, many research articles have been published using mouse models.

1.2 Rationale - Aims and objectives

The importance of this study lies in the fact that most of the past research is based on simplified theoretical models and computational fluid dynamics analysis, *lacking in vivo* and *vitro* verification. Complications after stent implantation influence basic physiological and pathological parameters, that dominate the non-Newtonian nature of blood, which have not been thoroughly investigated. Therefore, the hypothesis set in this Thesis is that the presence of a stent in the flow of blood may affect various physiological and mechanical properties of the fluid, reflected in haematological, rheological and hemodynamic indices.

The main aim of the project is to investigate changes in hematological hemorheological and hemodynamic parameters as a result of blood flow through stented vessels. The study includes *in vivo* approaches, using animal models and *in vitro* tests in stented polymer tubes using human blood and appropriate stents

In the *in vivo* approach, the study investigates the effects of stenting and the implantation time-course on hematological and hemorheological parameters that could potentially compromise the device's functionality and longevity.

The *in vitro* part of the study builds up and expands on previous knowledge by thoroughly investigating, the stent-induced changes in hematological hemorheological and hemodynamic parameters. The evaluation covered single and overlapping stent cases, to account for common clinical practices, in both straight and curved geometries (reproducing various coronary artery morphologies), under two different biomechanical flow regimes, reflecting a range of physiological flow conditions.

To summarize, the specific objectives of the study were to:

- Conduct a comprehensive literature review on coronary artery disease, cardiovascular implants, and complications following stenting
- Determine the role of blood rheological properties and how they are affected after stenting
- Examine *in vivo* the effects of stenting on hematological and hemorheological parameters at various post-stenting time points and investigate stent-induced alterations in white blood cell mechanical properties.
- Investigate the effect of single stenting and overlapping stenting on rheological and hematological parameters.

1.3 Thesis outline

The study was carried out through a collaboration between the Biorheology Laboratory and the Biomechanics and Living Systems Analysis (BioLISYS) Laboratory in the Department of Mechanical Engineering and Materials Science and Engineering at the Cyprus University of Technology. Innovative methodological approaches were applied throughout the study, including two main experimental parts, the *in vitro* setting to evaluate stent-induced changes in hematological, hemorheological and hemodynamic parameters and the *in vivo* experimental part to

assess the effects of stenting and the implantation time-course on hematological and hemorheological parameters.

The thesis is organised into five Parts including an introductory part (Part I), a second part in which the general methodology is explained (Part II), two following parts (Parts III and IV) elaborating on the different aspects of the study (*in vivo* and *in vitro*) and a general discussion/conclusions part (Part V). Part V also includes a synopsis chapter. In Parts III and IV, additional details of the methodology and literature review are provided at each relevant chapter in order to aid in the description of the work performed.

The Background and Introduction Part I provide a comprehensive overview of the research context, motivation, and objectives. Chapter 1 in Part I introduces the current state of the art in the field, outlining the background and motivation for the study. It emphasizes the significance of the research, states the primary aims, and defines the objectives of the project. This chapter concludes with an outline of the thesis structure. Chapter 2: Sections 2.1-2.4 in Part I, explores the fundamental aspects of blood, beginning with its constituents and their biological functions. The relevance of hematology in the context of cardiovascular implants is discussed, followed by an introduction to blood rheology. Key properties, including blood viscosity, red blood cell (RBC) aggregation, and RBC deformability, are analyzed in detail, highlighting their importance for cardiovascular issues. Section 2.5 examines cardiovascular diseases and their treatment, focusing on the use of coronary stents. The distinctions between bare-metal stents and drug-eluting stents are discussed, along with their respective advantages and challenges. This section also addresses complications such as stent failure and reviews clinical and experimental *in vitro* studies, providing a foundation for the research.

The Methodology Part describes the common experimental methods employed in both Parts III and IV of the study. Section 4.1 details the hematological techniques used to analyze blood components, establishing the framework for subsequent analyses. Section 4.2 focuses on the assessment of hemorheological parameters, including blood viscosity, RBC aggregation and RBC deformability and Section 4.3 presents the pressure system. The methodologies described in these chapters are integral to understanding the study's findings.

The *in vivo* investigation for elucidating the effects of stent implantation forms Part III of the thesis, elaborating on the impact of stent implantation on hematological and hemorheological parameters utilising specific mice models. In this part the objectives of the *in vivo* study are initially introduced, followed by a detailed description of the methodologies employed. Topics include stent, animal models, mouse stenting procedures, blood sampling and preparation, and Chapter 5 in Part III, presents the results obtained from the *in vivo* experiments. Hematological evaluations are reported first, followed by hemorheological findings, including viscosity, RBC aggregation, and RBC deformability. Section 5.4 provides a critical analysis of the results, discussing their implications for cardiovascular implant performance and their potential relevance for clinical applications. Results from this Part of the PhD programme have been published in Clinical Hemorheology and Microcirculation [34]:

Kokkinidou, D., *Kaliviotis, E., Shammas, C., Anayiotos, A., & Kapnisis, K. (2024). An in vivo investigation on the effects of stent implantation on hematological and hemorheological parameters. Clinical Hemorheology and Microcirculation, 87(1), 39–53. doi: 10.3233/CH-231921. PMID: 38143339.*

Chapter 6 elaborates on the investigation of stent presence on Lymphocyte stiffness. Results from this Part of the PhD program have been published in ACS Biomaterials Science & Engineering [25]:

Kapnisis, K., Stylianou, A., ***Kokkinidou, D.****, Martin, A., Wang, D., Anderson, P. G., Prokopi, M., Papastefanou, C., Brott, B. C., Lemons, J. E., & Anayiotos, A. (2023). Multilevel assessment of stent-induced inflammation in the adjacent vascular tissue. ACS Biomaterials Science & Engineering, 9(8), 4747-4760. https://doi.org/10.1021/acsbiomaterials.3c00540.*

The *in vitro* evaluation of the effect of stent configuration forms Part IV of the thesis, exploring the influence of stent design features, such as curvature and overlapping, on hematological and hemorheological profiles. Chapter 7 in Part IV, commences with the rationale for this experimental approach, and describes the methodologies employed, including blood sample preparation, stent design, tube stenting configurations, and the experimental procedure. Section 7.3 presents the results of this experimental study, focusing on hematological, hemorheological and

hemomodynamic evaluations under different stent configurations. Section 7.4 discusses the findings in the context of stent design optimization and their implications for hemorheological properties and blood flow. Results from this Part of the PhD program have been published in the Journal of Cardiovascular Engineering and Technology [35]:

***Kokkinidou D**., Kapnisis K., M. Chrysostomou, Shammas C., Anayiotos A, Kaliviotis E. (2025). In vitro evaluation of the effect of stenting on hematological, hemorheological and hemodynamic parameters, in various stent configurations and flow conditions. Journal of Cardiovascular Engineering and Technology, DOI: 10.1007/s13239-025-00791-0.*

A general discussion of the results of the study is provided in Part V of the thesis. In this part, the findings from Parts III and IV are synthesized and an overall discussion is provided in Chapter 8. The Thesis closes with Chapter 9: which provides a comprehensive summary of the study's conclusions and future work.

Chapter 2: Literature review

2.1 Blood

The average adult human possesses over 5-6 liters of blood. Blood is a specialized and vital fluid in the human body that contains different cells, proteins and sugars [36]. Each of the elements plays a unique role in maintaining overall health and homeostasis. Beyond its complex composition, blood performs a wide array of essential functions critical to life.

It acts as a transport system, delivering oxygen and vital nutrients to the lungs and tissues while removing waste products for filtration and excretion through the kidneys and liver. Blood also plays a pivotal role in defence, carrying immune cells and antibodies to combat infections. Additionally, it aids in wound repair through clot formation, preventing excessive blood loss. Blood's role extends to temperature regulation, ensuring the body maintains an optimal internal environment.

The circulatory or cardiovascular system is a complex system of distribution of nutrients, gases, electrolytes, removal of waste products of metabolism and other substances. The system consists of the heart, the blood, the blood vessels and the lymphatic system. The main blood vessels include arteries, arterioles, capillaries, veins, and venules, transporting blood throughout the body. Blood vessels form a network that allows blood to flow from the heart to all living cells and back to the heart [37]. Another essential part of the circulatory system is the lymphatic system, which drains a fluid known as lymph and includes lymph vessels, lymph nodes and lymph glands. The cardiovascular system circulates blood throughout the body, with the ability to adjust the speed and volume of blood flow in response to various stimuli. Regulation of the cardiovascular system is influenced by a wide range of factors, including changes in blood volume, hormones, electrolytes, osmolarity, medications, adrenal gland activity, and kidney function, among others [38].

Arteries transport oxygen-rich blood to organs under high pressure. With elastic tissue to expand and contract, arteries maintain steady flow despite the pulsatile heartbeats. Arteries, branch into muscular arteries, like the brachial and femoral, and then into smaller arterioles. Arterioles, mainly smooth muscle, regulate blood flow based on the body's needs and control vascular resistance [39].

Capillaries, the thinnest vessels, allow nutrient and waste exchange via diffusion. Venules collect blood from capillaries, facilitating additional exchange before transferring it to veins. Veins, with thin, low-pressure walls, hold most of the body's blood and contain one-way valves to ensure blood returns to the heart. Muscle contractions and breathing help veins move blood from the lower extremities [39].

2.2 The constituents of blood

2.2.1 Human blood

Blood is composed of plasma, white blood cells (WBCs), platelets, and red blood cells (RBCs). Plasma makes up about 55% of the blood and contains water along with essential proteins, sugars, and fats. The remaining 45% consists of cellular components, including red blood cells (RBCs), which carry oxygen, and WBCs and platelets, which are involved in immune defence and blood clotting, respectively. All blood cells originate from stem cells in the bone marrow and mature into RBCs, WBCs, or platelets. RBCs are shaped like "biconcave disks," with a disc diameter of approximately 6.2-8 μm and a 2 μm thickness at the edges [40]. There are approximately 5 billion RBCs per millilitre of blood, so the total RBCs' surface area in a normal human adult is approximately 3000 m^2. The cytoplasm contains large amounts of hemoglobin (Hb), an iron-containing protein that efficiently binds oxygen. This high concentration of Hb enhances the oxygen transport capacity of blood, as a result, the oxygen-carrying capacity of whole blood is approximately 65 times more effective than that of plasma alone (~ 21 ml O2 per 100 ml blood versus 0.3 ml O2 per 100 ml plasma, at 1 atmosphere) [40]. The volume fraction of RBCs is important to the rheological and physiological characteristics of blood that a specific term, known as the hematocrit (Hct) defined by $\mathrm{HCT} = \frac{\text{Volume of RBCs}}{\text{Total blood volume}}$. WBCs are further categorised into lymphocytes, monocytes, and granulocytes, the latter of which include neutrophils, eosinophils, and basophils. Together, these components enable blood to transport nutrients, remove waste, fight infections, and prevent blood loss [36]. Figure 2.1 illustrates the various cell types contained in the

whole blood, while Figure 2.2 presents a detailed breakdown of the components within human blood.

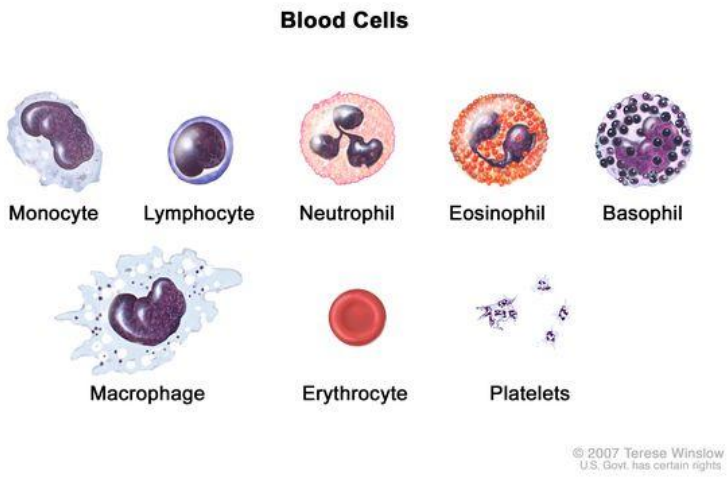

Figure 2.1: Blood cells [41].

Morphological abnormalities of erythrocytes can arise from either the production of defective erythrocytes in the bone marrow or pathological conditions affecting the erythrocytes within the circulation. Macrocytes typically indicate abnormal erythropoiesis, characterized by a reduced number of cell divisions during the maturation of erythroid precursors [42].

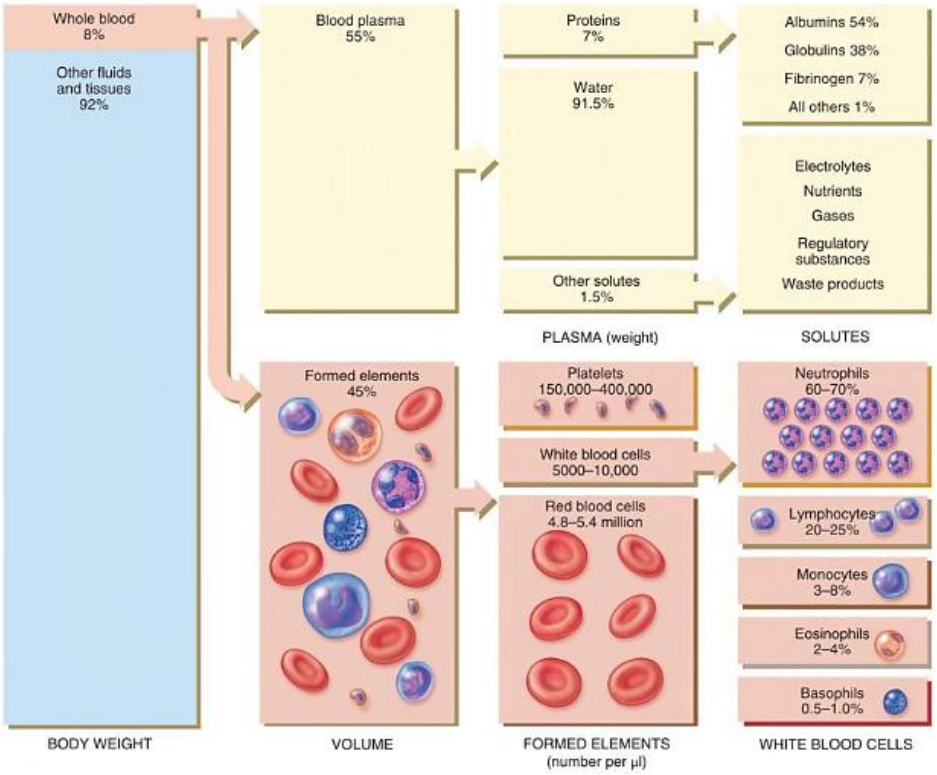

Figure 2.2: Composition of blood [39].

2.2.2 Animal (rodent) blood

The cardiovascular systems of rodents and humans share many similarities but also notable differences. Murine RBCs are spherical, anucleate, biconcave discs with central pallor, measuring approximately 4 to 7 µm in diameter. Total RBC counts in mice range between 7800 and 10,600 per microliter, with hematocrit (HCT) levels in healthy controls spanning 35% to 52%, which generally corresponds to three times the hemoglobin (HGB) concentration. Mice have relatively small RBCs compared to most mammals, with a mean cell volume (MCV) of 45 to 55 fL. Additionally, mouse RBCs have a shorter half-life of 38 to 52 days, contrasting with the longer RBC lifespans observed in humans and other species. White blood cell (WBC) counts in mice typically range from 2000 to 10,000 per microliter, and their blood composition is distinctively rich in lymphocytes, making up 75-90% of the total WBC count. Neutrophils constitute only 10-25% of murine WBCs, a stark contrast to human blood, where neutrophils dominate, comprising 60-70% of the total WBCs, with lymphocytes accounting for 20-25%. Human WBCs are generally 10 to 15 µm in

diameter, with scant blue cytoplasm, smooth chromatin, and a centrally placed, round, or slightly indented nucleus, as shown in Figure 2.3.

Carotid arteries are prone to atherosclerosis in humans, often leading to atherothrombotic complications or acute thrombosis following carotid stenting, which can result in strokes. Unlike humans, mice do not naturally develop atherosclerosis. The carotid artery is a primary site for mouse thrombosis research due to its size and accessibility. Human carotid artery wall shear rates (WSRs) range from 260–500 s^{-1} (diameters 4.3–8.2 mm), with slightly lower values in females, while murine WSRs range from 350–3500 s^{-1} (diameters 300–500 µm), averaging 1850 s^{-1} [43].

Coronary arteries, critical in myocardial infarction, are challenging to study in mice due to imaging difficulties. However, the left anterior descending (LAD) artery ligation is a commonly used ischemia-reperfusion model. Human coronary WSRs range from 100–600 s^{-1} depending on health and vessel diameter (2.6–5.0 mm). In mice, LAD flow rates of 0.5 mL/min in 230 µm vessels produce WSRs of 6700 s^{-1}, with similar values reported for smaller coronary arteries [43].

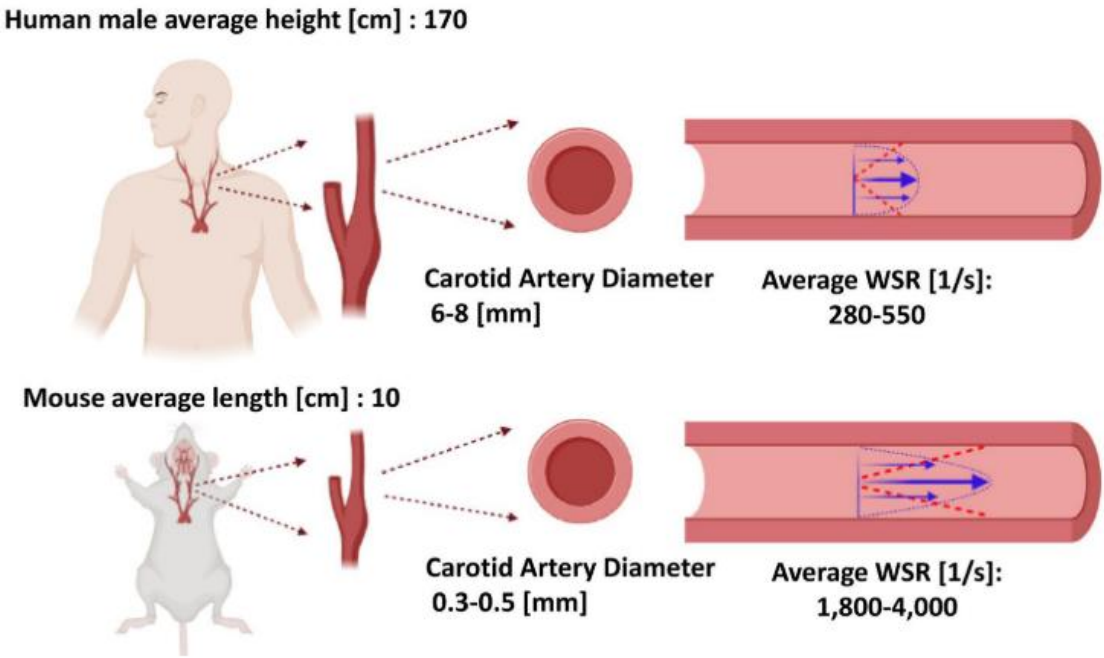

Figure 2.3: Species differences (human vs. mice): Mice arteries are about 15 times smaller than human arteries, resulting in WSR values approximately 15 times higher in mice than in humans [43].

2.3 Hematology in cardiovascular implantation

Hematological parameters are fundamental tools in the field of hematology, providing critical insights into the physiological and pathological status of the blood and its components. These markers are increasingly recognized for their relevance in cardiovascular diseases (CVDs) and the outcomes of stenting procedures. Key parameters include red blood cell (RBC) count, mean corpuscular volume (MCV), red cell distribution width (RDW), and white blood cell (WBC) count, among others. RBC indices, such as MCV, RDW and hemoglobin concentration are essential for diagnosing and classifying anemias, as they reflect the size, volume, and variability of red blood cells. These indices have also been linked to adverse cardiovascular outcomes. Similarly, WBC parameters are critical for evaluating immune function and detecting inflammatory or infectious processes. Collectively, these hematological markers serve as indispensable tools for diagnosing a wide range of hematological and systemic disorders, guiding treatment decisions, and monitoring disease progression or therapeutic responses.

Among these, RDW a measure of anisocytosis (variability in red blood cell size) is traditionally used to monitor anemia but has gained attention for its association with human pathology and cardiovascular diseases. Recent studies have demonstrated that RDW is closely correlated with inflammation and cardiovascular risks, including in-stent restenosis. Geng et al. (2019) found that elevated RDW-CV values are linked to increased inflammation and a higher risk of restenosis following stent implantation [26].

Inflammation is a critical factor in the development and progression of atherosclerosis, contributing to every stage, from lesion initiation to plaque progression and destabilization [44]. This has spurred research into various inflammatory markers to better predict cardiovascular risk. Among these, WBC count and its subtypes, such as neutrophils and lymphocytes, play a significant role in reflecting systemic inflammation, a key driver of atherosclerosis and plaque instability. The neutrophil-to-lymphocyte ratio (NLR), which combines two independent markers of inflammation, is recognized as a simple yet effective indicator of inflammatory activity [44]. Notably, lymphocytes are central to

modulating the inflammatory response, and lymphopenia has been associated with progressive atherosclerosis in both clinical and experimental studies.

In summary, hematological parameters, particularly RBC, WBC count and MCV not only provide diagnostic and prognostic insights into hematological disorders but also offer valuable information about cardiovascular health and the risk of complications following stent implantation. These parameters continue to be explored as accessible and cost-effective tools for improving the diagnosis, monitoring, and management of cardiovascular diseases.

2.4 Blood rheology

2.4.1 Blood viscosity

Blood viscosity is a critical hemodynamic parameter that plays a key role in determining the flow dynamics of whole blood within blood vessels. Blood viscosity is influenced by hematocrit, plasma viscosity and the ability of RBCs to deform and disaggregate under certain hemodynamic conditions. Viscosity is the internal friction arising from intermolecular forces within a flowing liquid. Blood has been recognized as a non-Newtonian fluid, showing shear-thinning behavior and has viscoelastic properties. Due to the shear-thinning behavior of whole blood, which is influenced by the RBCs' rheological properties, its viscosity varies according to the hemodynamic conditions, namely the shear rates [45].

Blood viscosity fluctuates in response to pulse wave velocity during cardiac systole and diastole. Viscosity increases when the shear rate is low, as a result of cardiac diastole. Conversely, viscosity decreases when the shear rate is high [46]. The power law model, Casson model and Carreau-Yasuda model (Figure 2.4) are commonly used non-Newtonian models for modelling blood viscosity, which exhibits shear thinning behavior [46]. A comprehensive review of blood viscosity models has been provided by Beris et al 2021 in [47] including the Stephanou and Georgiou 2018 model [48].

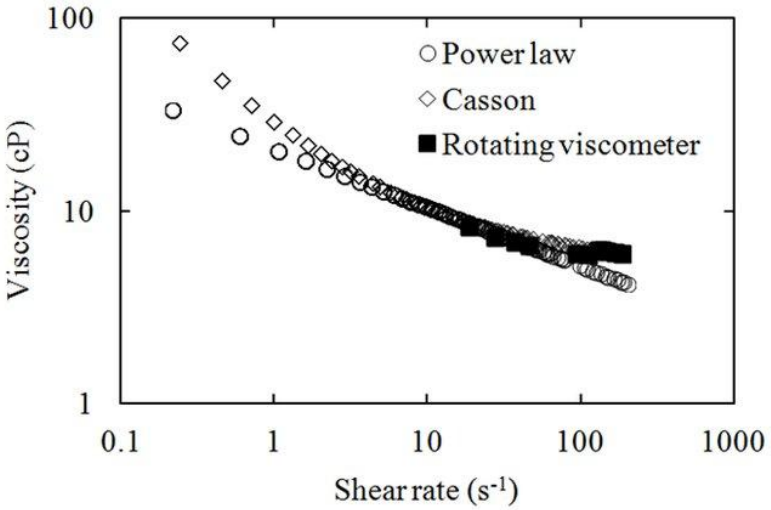

Figure 2.4: Viscosity and shear rate of blood using different models: Power law, Casson model and rotating viscometer [49].

Blood viscosity varies significantly across species, including differences between humans and mice [43]. However, at arterial shear rates, blood can be approximated as a Newtonian fluid with a constant viscosity of 0.03 to 0.04 poise, which is similar to murine blood viscosity under these conditions [50].

Whole blood viscosity is influenced by the number and volume of RBCs present in the blood and is therefore linearly associated with hematocrit [44]. The effect of hematocrit on blood viscosity is significantly greater at low shear rates, such as those found in veins, compared to high shear rates, as seen in arteries [51]. At high shear rates, an increase of one unit in hematocrit is estimated to raise blood viscosity by 4%, assuming no change in the rheological properties of red blood cells.

2.4.2 RBC aggregation

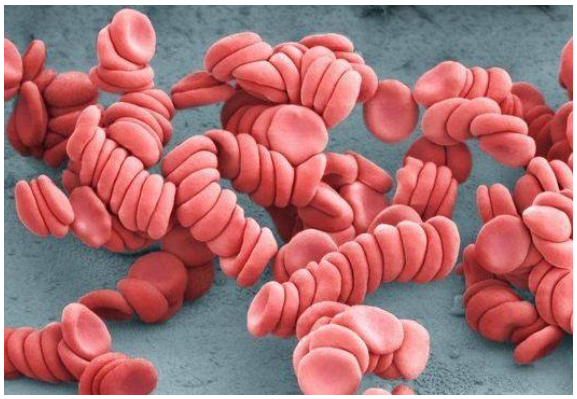

Figure 2.5: Red blood cells, Rouleaux formation [52].

Red blood cells (RBCs) can aggregate into two- or three-dimensional structures in aqueous solutions containing large plasma proteins (like fibrinogen) or polymers (e.g., 70 kDa dextran). These structures form when fluid shear forces are low and disperse when shear forces increase, making the process reversible. In two-dimensional structures, cells align face-to-face, forming stacks known as rouleaux (Figure 2.5). While these form between glass slides, larger 3D structures can develop under different conditions. RBC aggregation occurs quickly, within seconds, and may happen in areas with low shear in the body. This phenomenon, known since the 18th century, was detailed by Fahraeus, who linked it to blood stability and erythrocyte sedimentation rate, a common inflammation marker [53].

RBC aggregation significantly influences blood flow, tissue perfusion, and vascular resistance, with its effects depending on the vascular regions where aggregates form. RBC aggregation typically occurs in low shear rate areas, such as veins or bifurcations, leading to a marked increase in blood viscosity in these zones. Conversely, high shear rate areas, such as arteries and arterioles, promote the disaggregation of RBC aggregates. However, persistent aggregates have been observed in large arteries, where they can alter flow dynamics. These aggregates promote RBC axial migration, widening the cell-free layer. This process has three key consequences: (i) reduced apparent blood viscosity and flow resistance, (ii) decreased wall shear stress, which lowers endothelial nitric oxide (NO) production and vasodilation, and (iii) enhanced plasma skimming at bifurcations, decreasing

microcirculatory hematocrit and viscosity (Fahraeus and Fahraeus–Lindqvist effects) [54].

2.4.3 RBC deformability

RBCs have a unique biconcave disk shape and behave as elastic bodies; cells respond to applied pressure, such as reduced diameter, by extensive changes in their shape followed by a reversal when the deforming force is removed [55].

RBC deformability is influenced by several factors, including internal (cytosolic) viscosity, primarily determined by mean cell hemoglobin (MCH) concentration, membrane viscoelasticity, which depends on cytoskeleton proteins and lipid bilayer properties, and the surface-area-to-volume ratio, also known as cell sphericity [51]. At low shear rates, rigid RBCs are less prone to aggregation compared to deformable ones. Consequently, reduced RBC deformability at very low shear rates leads to a decrease in blood viscosity. Conversely, at shear rates exceeding 1 s–1, reduced RBC deformability results in an increase in blood viscosity [56]. Erythrocyte deformability is a key hemorheological factor in maintaining adequate blood flow and tissue perfusion. In pathological conditions, such as sickle cell disease, reduced erythrocyte deformability leads to sequestration at capillary entrances, increasing resistance to microvascular blood flow [55].

2.5 Cardiovascular diseases and cardiovascular implants

Cardiovascular diseases (CVDs) are the leading cause of death worldwide, responsible for approximately 17.9 million deaths in 2019, which accounted for 32% of all global fatalities based on WHO [57]. Coronary artery disease is a common heart condition characterized by the formation of atherosclerotic plaque within the blood vessels, which impairs blood flow and reduces oxygen delivery to the heart. Early diagnosis and treatment are crucial to prevent the severe medical implications associated with coronary artery disease. This activity outlines the evaluation, diagnosis, and management of the condition, emphasizing the importance of the healthcare team's role in assessing and treating patients [58].

2.5.1 Treatment

Despite the significant advances that have been progressed in the diagnosis and treatment of atherosclerosis and its pathological mechanism of action, many aspects and subsequent complications remain unclear. The pathogenesis of atherosclerosis is complex and multifactorial, involving interactions between the cellular structure of the arterial intima, lipid metabolism and inflammatory processes.

Despite the introduction of stent technology over balloon angioplasty, restenosis remains a significant limitation, with a prevalence of 20-30%. Since excessive smooth muscle cell proliferation is the primary cause of restenosis, new technologies were developed to target specific cellular mechanisms aimed at preventing neointimal hyperplasia. Figure 2.6 illustrates the number of coronary stent implantations per million people across various countries in 2016, highlighting substantial regional differences. France, with 4,075 implantations per million, leads in stent use, while Egypt has the lowest rate at 1,165 per million. This variation underscores disparities in access to cardiovascular interventions and points to the need for an improved understanding of both availability and usage factors in stent-based treatments. Although early oral pharmacologic therapies showed promise in animal models of in-stent restenosis, clinical trials in the early 1990s yielded largely disappointing results. Clinical case success was achieved with the advent of localized therapy, using stents as drug delivery platforms. This approach utilized polymers to attach and control the release of drugs from the stent, allowing for sustained drug delivery. A series of successful preclinical studies paved the way for stent-based local drug delivery in humans [59].

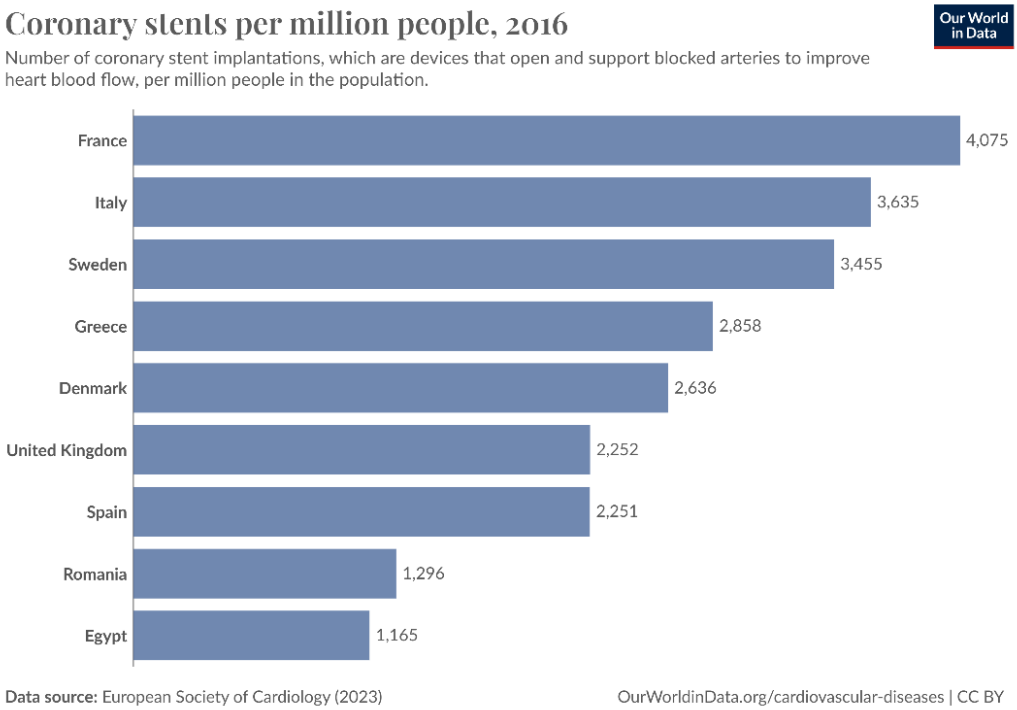

Figure 2.6: Coronary stent implantations per million people across countries in 2016. France had the highest rate (4,075 per million) and Egypt had the lowest (1,165 per million). Data: European Society of Cardiology (2023) [60].

2.5.2 Coronary stents

Coronary stents are expandable metallic tubular devices deployed within coronary arteries that have become obstructed as a result of atherosclerotic disease. Stents are very small metal tubes that are inserted via a balloon catheter into the narrowed segment of the artery (Figure 2.7). Upon balloon inflation, the stent expands and is embedded into the artery vessel wall, which effectively opens the previously narrowed artery segment. The balloon is then deflated and removed along with the catheter, and the stent remains in place, acting as a metal framework to maintain arterial support [61]. This revascularization technique is known as percutaneous coronary intervention (PCI), or coronary angioplasty with stent placement. The use of coronary stents has mitigated the risks of coronary dissection and vascular recoil, as the expandable metallic mesh of the stent provides structural support and prevents adverse vascular remodelling.

The development of coronary stents, first introduced in the 1980s, has significantly advanced coronary revascularization by improving upon earlier balloon angioplasty techniques. In the absence of stents, balloon angioplasty refers to a technique that uses an inflated balloon catheter within coronary arteries to compress the atherosclerotic plaque and restore blood flow. However, this procedure had several limitations, such as arterial recoil, coronary dissection, thrombosis, and restenosis. The introduction of coronary stents, with their expandable metallic mesh structure, eliminated issues like vessel recoil and dissection, providing more durable vascular support. Coronary stents have since evolved into several types, including bare metal stents (BMS), drug-eluting stents (DES), bioresorbable scaffold systems (BRS), and drug-eluting balloons (DEB) [62].

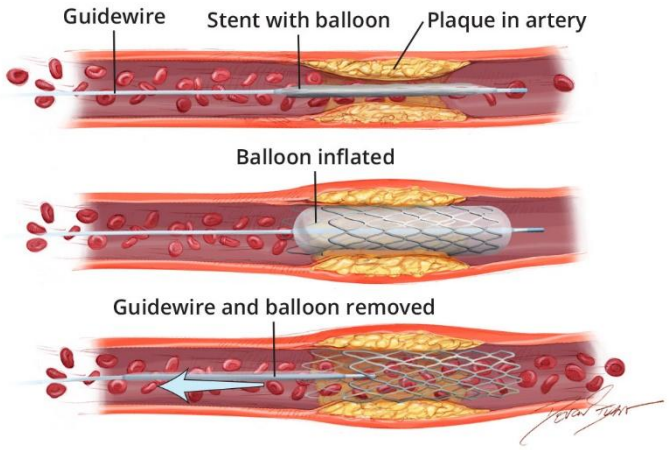

Figure 2.7: Stenting procedure [59].

2.5.3 Bare metal stents

Bare metal stents (BMS) are widely used and typically made from stainless steel or nitinol, a nickel-titanium alloy that self-expands when exposed to heat after implantation. These small mesh tubes generally vary in length from 8 to 38 mm and in diameter from 2.5 to 5.0 mm. Stents are categorized based on their configuration, either slotted or coiled. In slotted stents, the struts are primarily aligned along the longitudinal axis, providing rigidity in that direction. In contrast, coiled stents have struts oriented predominantly perpendicular to the longitudinal axis, allowing for greater flexibility [63]. A functional stent unit consists of struts connected to form

rings. When the balloon's radial force expands the rings, plastic deformation of the struts occurs [64].

2.5.4 Drug eluting stents

Drug-eluting stents (DES) have been designed to reduce the risk of in-stent restenosis and improve the long-term efficacy of PCI. DESs are composed of three key components: a metallic stent platform, a drug, and a carrier vehicle. The metal, often stainless steel or cobalt-chromium, provides long-term mechanical support to prevent vascular recoil. The drugs used in DES inhibit smooth muscle cell proliferation and intimal hyperplasia, reducing the risk of restenosis. Rapamycin-based drugs block cell cycle progression by inhibiting the mTOR pathway, while taxanes interfere with cell division by targeting microtubule function. A polymer coating is used to hold and slowly release the drug over time, and it biodegrades into water and carbon dioxide.

First-generation DESs typically used sirolimus or paclitaxel on stainless steel, while second-generation DESs employ zotarolimus or everolimus on a cobalt-chromium or platinum-chromium base. Specialized stents, such as bifurcation or covered stents, are used for specific conditions like lesions at artery branches or vessel perforations.

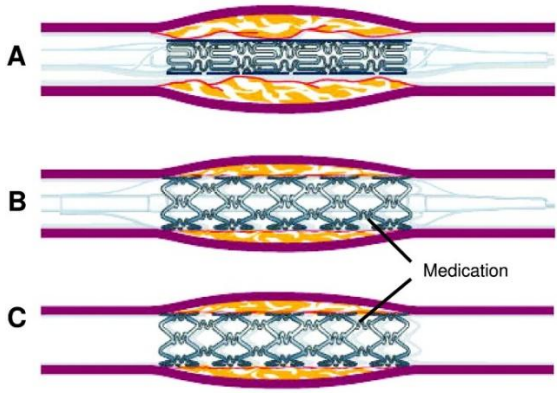

Figure 2.8: A: The stent is mounted on a balloon catheter and guided to the narrowed, diseased section of the coronary artery; B: The balloon is inflated, expanding the stent and opening the constricted artery segment; C: After deflating the balloon and removing it, the stent remains embedded in the artery wall. Drug-eluting stents release medication to lower the risk of restenosis, or re-narrowing of the artery [61].

2.5.5 Stent complications - failure

New-generation drug-eluting stents with thinner struts and more biocompatible polymers have shown improved outcomes at 1 year. However, stent-related adverse events still occur at a rate of 2–3% annually beyond the first year, persisting for up to at least 5 years of follow-up, which is comparable to contemporary bare-metal stents [65–67]. Additionally, long-term follow-up data have raised concerns about the high failure rates of the latest stent technology iteration, bioresorbable scaffolds, although these failures are attributed to various factors [46].

In-stent restenosis (ISR) remains a significant concern, as it is a prevalent but not fully understood cause of stent failure in the drug-eluting stent era, with a wide range of clinical presentations. Similarly, while a combination of patient, lesion, and procedural factors is known to trigger stent thrombosis, its underlying biology remains poorly understood. Importantly, coronary stenting is designed to mechanically relieve artery blockages by restoring blood flow, but it does not address the complex underlying atherosclerotic disease. This limitation has a significant impact on stents, as ISR and stent thrombosis rates are considerably higher in patients with complex lesions, including those associated with acute coronary syndromes, bifurcations, chronic total occlusions, or longer lesions. The risk is also elevated in individuals with conditions that accelerate atherosclerosis, such as diabetes or renal failure. This indicates that the progression of atherosclerosis and its complications may be a key factor in stent failure [66].

2.5.6 Stent failure - design

Regarding the influence of the stent design, it is already established that specific characteristics, namely mesh design, strut density and strut thickness, etc. play a significant role in the vascular response, restenosis, and other effects [68,69]. Studies with animal models signified that these characteristics, affect the experimental vascular injury and neointimal proliferation [70].

In alignment with clinical findings, computational fluid dynamics (CFD) studies demonstrated that elevated stent strut density and increased strut thickness increase local blood flow disturbances, thereby promoting thrombogenicity [71],[72]. In an

ex vivo model, thick struts measuring 162 μm resulted in a 1.5-fold increase in thrombogenicity compared to thin struts of 81 μm [72]. In addition, a preclinical study demonstrated that after three days of implantation in porcine coronary arteries, thick-strut stents exhibited a 1.6-fold higher thrombus coverage compared to thin struts [72]. Stent underexpansion and malapposition of stent struts have also been linked to a high risk of in-stent restenosis (ISR) and stent thrombosis [73,74]. Moreover, research indicates an elevated ISR and target lesion revascularization risk in cases where a stent gap exists, defined as incomplete coverage of a coronary lesion between two stents [73,74], most predominant when treating bifurcation lesions [29,75].

Although newer-generation bioresorbable stents (BRS) have reduced strut thickness (<120 μm), the impact on scaffold thrombogenicity remains uncertain. A recent study by Lu et al. (2018) investigated three types of DES and scaffolds, XIENCE (81 μm), Absorb BVS (157 μm), and ArterioSorb BRS (95 μm) in a 3-mm silicone coronary model perfused with porcine blood. Immunofluorescence and OCT were used to assess platelet adherence and thrombus formation, while CFD analyzed flow patterns. Thin-strut BRS showed significantly lower thrombus formation compared to thick-strut BVS (0.005 mm^2/mm vs. 0.046 mm^2/mm; $p < 0.0001$) and similar results to metallic DES. These findings suggest that thinner BRS struts reduce flow disturbance and thrombogenicity, indicating potential advantages in subacute thrombus reduction [76].

2.5.7 Stent failure - Type of stents

While the latest generation of drug-eluting stents (DES) has drastically reduced the occurrence of early-stage ISR, through inhibition of cell proliferation, extended late-phase in-stent restenosis has also been reported [26–28]. Incomplete or delayed stent endothelialization, caused by drugs like sirolimus and paclitaxel, affects local flow conditions and thereby the RBC profile and blood rheological properties [29,77]. A recent study by Palmerini et. al [78], utilized also an *in vitro* stent perfusion system to assess the thrombogenic properties of various bare metal stents (BMS) and drug-eluting stents (DES). The results revealed that DES exhibited the lowest rates of thrombus formation, significantly differing from the other stent types [78].

Previously, Koppara et al. (2015) observed that the drug-eluting stent type (Xience stents) demonstrated a significantly reduced adhesion of inflammatory cells to the strut surface [79].

2.6 Clinical and *in vitro* studies

In vivo studies for stents, and how they affect hematological index are available in the literature however, the correlation with the hemorheological factors presents a gap with the topic still being unexplored.

Zhang et. al 2015 examined the platelet counts of patients six months after stent implantation. It was observed that platelet counts significantly fell in more than 70% of patients and only 23.1% of patients showed an increase compared to the period before stent implantation. The changes in platelet counts were correlated with different factors, namely positively correlated with white blood cells (WBCs) and fibrinogen values and negatively correlated with the number of stents [80]. Qian et al., 2018 examined 261 patients with coronary artery disease implanted with drug-eluting stents and the result showed higher hematological parameters (WBCs, RDW, etc.) and no differences in red blood cell count [81].

Red blood cell distribution (RDW) is a hematological parameter, which applies as the measurement for anisocytosis diagnosis and is mainly used for anemia disease. Recent studies, in the last decade, have related RDW with human pathology and cardiovascular disease. Geng et. Al. examined the role of the hematological index of red blood cell distribution (RDW-CV) and how it is correlated with in-stent restenosis. The clinical study showed that RDW is closely correlated with restenosis and the elevated RDW shows high inflammation [82].

Kassain et.al. studied patients with acute myocardial infarction and selected only the extreme cases of patients with very long lesions (≥ 25 mm). Two different overlapping stent cases were examined; the first case was only DES compared with a combination of DES and bare metal stents. Overlapping stents are common, especially the utilization of a combination of DES was preferred in clinical cases with longer lesions. In addition, most patients with left anterior descending artery lesions

were treated with the same combination. A small group of patients was treated with the DES-BMS group, overlapping stents for the coverage of dissections. It was concluded that overlapping with bare metal stents in the proximal part of a long DES compared to the deployment of two or more overlapped DES is the most appropriate and safe treatment in these clinical cases [83].

Erythrocyte aggregation is primarily thought to result from elevated levels of adhesive plasma proteins, with fibrinogen playing a central role [84]. In line with this, the aim of the following study by Szapary et al., 2009 was to understand the alterations in hemorheological parameters and platelet aggregation after carotid implantation. In this group, 18 patients with high-grade carotid stenosis who underwent carotid stent implantation were examined. Haematocrit, plasma fibrinogen, plasma, and whole blood viscosity were measured directly before and after the surgical intervention, followed by the 1st, 2nd, 5th, and 30th days' measurements after it. It was observed that hemorheological variables decreased after implantation [85]. Figure 2.9 depicts the outcomes of all the measurements of the parameters and it can be observed that all of them fell instantly after the procedure and raised by the fifth day of implantation in comparison with baseline. Stent occlusion and restenosis can be caused by changing the rheological parameters and platelet activation [86].

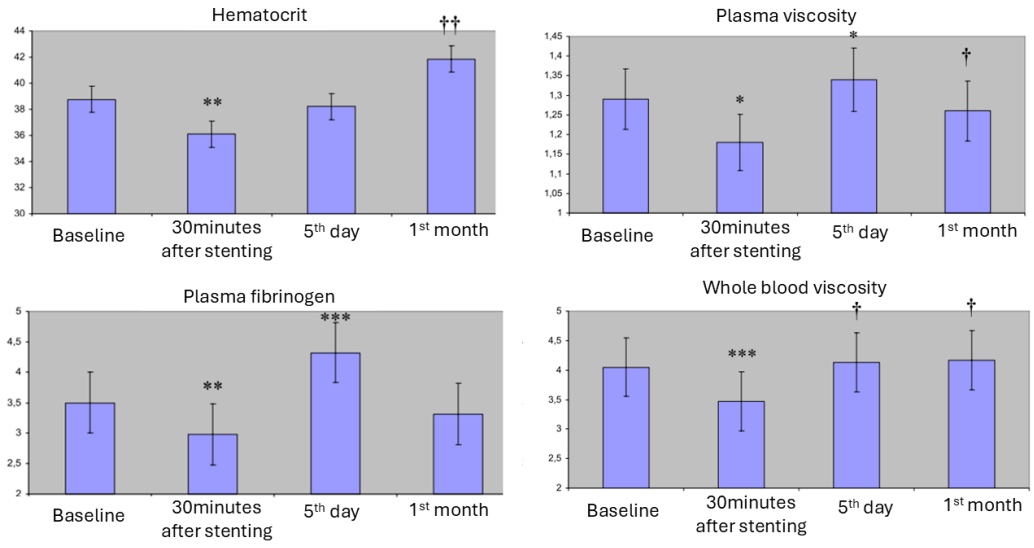

Figure 2.9: Hematocrit, plasma fibrinogen, plasma and whole blood viscosity after intervention (†p< 0.05, ††p< 0.01, ∗p< 0.005, ∗∗p< 0.001, ∗∗∗p< 0.0001) [85].

Palmerini et al., 2020 investigated an *in vitro* system of stent perfusion and the thrombogenicity of different DES and BMS. The experimental system was tested by deploying different stents with dimensions of 3 mm x 18 mm and four parallel silicone tubes with an internal diameter of 3 mm connected to a peristaltic pump. Each circuit was closed using a silicone connector and the perfusion lasted 2 hrs. The chosen flow rate was 10 mL/min, and a constant pressure was examined for 20 s. Blood was selected from healthy volunteers and incubated with fibrinogen. I-fibrinogen was used to determine the surface thrombus deposition [78].

Two sets of experiments occurred. In the first phase, the thrombogenicity of 4 currently available stents was compared. In the second phase, the thromboresistant and the absorption of albumin were investigated. The findings showed that the lowest rates of thrombus formation were observed in the case of DES and mentioned a significant difference with the other types of stents.

Another experimental study by Benard, et.al. 2003 investigated an *in vitro* model of intravascular prosthesis to study blood flow in a stented area. Specifically, the experimental artery included a transparent rectangular channel, and five different constant flow rates using a programmable pump (6.8, 10, 11.6, 12.3, 17.3 l/ml) were tested. As fluid was used a 50.6% by volume water glycerine mixture solution with a 6.9 cP viscosity and a density of 1.02 g/ cm^2. To summarize, the velocity field measurements in complex geometrical patterns and limited areas were obtained using the particle image velocimetry method (PIV). PIV was applied to measure the flow between and over the stent. Consequently, the WSS was quantified by using the aforementioned method. Several prosthesis designs were studied.

These specific geometries and areas are ideal for restenosis. The WSS was altered due to the interaction between the stent wire and blood flow. It was concluded that zones with EC proliferation are localized at the sites of low WSS, as strong shear leads to cell migration. Furthermore, it was demonstrated that the highest values of SS are localized close to the stent struts. As the endothelial proliferation was greatly influenced by the SS, knowing that these alterations were caused due to SS after stenting could be significant for the future improvement of the stent design, followed by the reduction of the phenomenon of restenosis [87].

Zhu et al., 2020 developed a new coated coronary stent decorated with heparin/NONOate nanoparticles Figure 2.10. They studied the release behaviors of heparin and nitric oxide (NO). Bioactive molecule NO affects the physiological functions in the body, such as preventing thrombosis, smooth vascular muscle cell proliferation, and promoting endothelial cell growth. The compatibility and cytotoxicity of the stent were evaluated through different tests, whole blood and adhesion tests, colorimetric assays (hemolysis assay test, MTT assay), and through using an experimental *in vivo* rabbit model of atherosclerosis. Two groups of stents were implanted in the rabbits, namely the bare SS stents and SS-PGMA-Hep/ NONOates stents. The stents were evaluated using SEM and vascular pathological analysis. The results showed that the usage of the specific combination of coating has a rapid anticoagulant effect and provides the regeneration of endothelial cells [88].

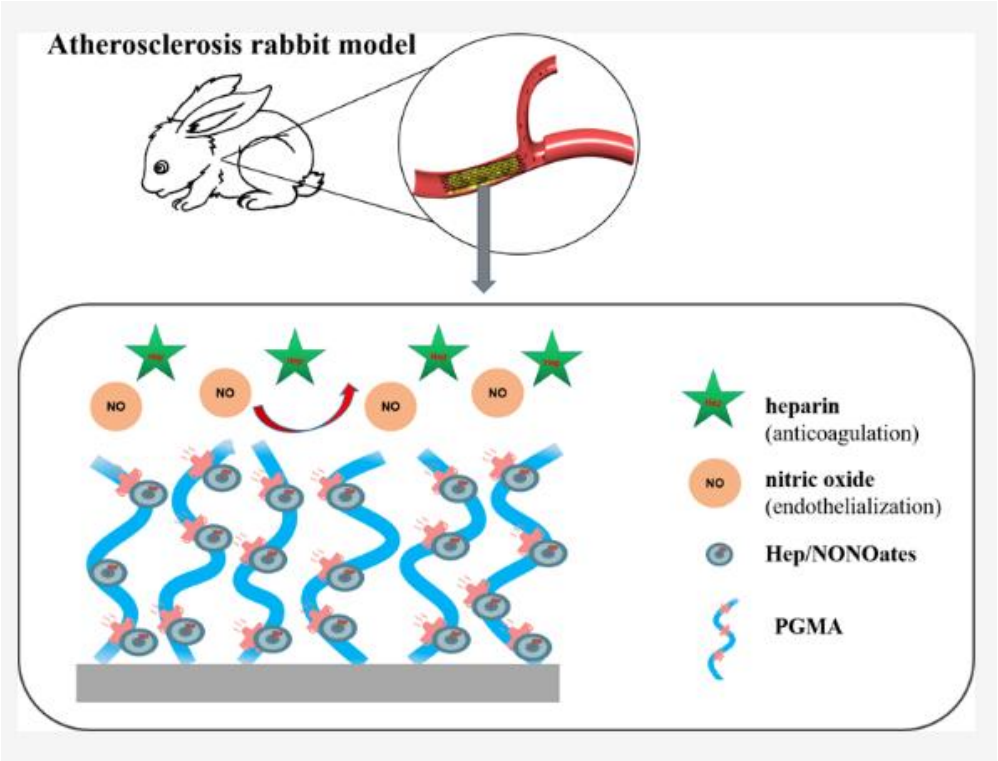

Figure 2.10: Coronary stents decorated by Heparin/NONOate nanoparticles [88].

Kapnisis et.al. investigated the changes in RBC properties due to the presence of stents. Blood was collected from a healthy population into vacuum tubes containing EDTA. After the collection, one portion of the blood donation from each participant

was kept as the normally aggregating blood sample and another portion of the blood donation was changed/ altered in order to produce non-aggregating blood samples. Hemorheology tests were performed immediately after collection and treatment within 4 hours. In the experiments were used self-expanding nitinol stents. RBC aggregation, RBC deformability, viscosity, and RBC membrane integrity were examined. The outcomes indicate that the presence of a stent in a vessel has an influence on the hemorheological characteristics of blood. A remarkable observation is that the reduction in RBC aggregation is apparent in the stented case, due to the changes in the mechanical and biochemical membrane properties [68].

Toth C. et.al investigated the early postoperative complications of vascular graft implantation using a canine model. It was used two groups, the control group, and the grafted group. The tested group included a 3mm PTFE graft that was the replacement of a 3.5 cm segment removed unilaterally from the femoral artery. Controlled parameters, i.e. skin temperature of both hind limbs, and blood collection for hematological, hemostaseological and hemorheological tests were examined at five time points (1st-3rd-5th-7th and 14th postoperative days). The outcomes of this study showed that significant change occurred in several hemostaseological and hemorheological parameters due to the presence of graft [89].

Part II: Research design and methodological approach

The work in this PhD program was designed in a structured approach, beginning with *in vivo* experiments that incorporated lymphocyte isolation and atomic force microscopy (AFM), followed by in vitro studies. This sequence was chosen to capture both the complex physiological responses to stenting and the implantation time-course on hematological and hemorheological parameters that could potentially compromise the device's functionality and longevity. The *in vivo* phase was designed to evaluate real-time biological and systemic responses to stenting, including inflammation, blood rheology, and vascular changes, which are difficult to fully replicate in controlled laboratory conditions. By examining the physiological reactions in a living system, the study aimed to provide crucial insights into how stents interact with host tissues and blood over time.

Following the animal studies, the *in vitro* experiments were conducted to isolate and analyze the mechanical and hemorheological changes induced by stents in a controlled *in vitro* environment. This approach enabled the precise assessment of stent-related alterations in blood flow, viscosity, RBC deformability, and aggregation, eliminating systemic variables present in *in vivo* conditions. The inclusion of a pressure drop measurement across the stented area provided further insights into hemodynamic changes, a crucial factor for clinical evaluation and stent optimization. By integrating both methodologies, the research bridged gaps between theoretical models, computational simulations, and experimental validation, ensuring a comprehensive understanding of stent-induced effects on blood and vascular tissues.

Chapter 3: *In vivo* and *in vitro* approaches

The *in vivo* experiments were designed to investigate the biological and physiological impact of stent implantation in a dynamic and natural environment. Cardiovascular stenting is widely used for treating coronary artery disease, yet information regarding its influence on hematological and hemorheological profiles remains scarce. Most previous studies rely on computational models, lacking experimental verification. To address this limitation, custom-made self-expanding nitinol stents were implanted in the common carotid artery of male CD1 mice to assess implantation time-course effects on blood parameters, hematological and hemorheological.

The changes were likely linked to peri-implant inflammatory responses, highlighting the importance of stent design characteristics such as mesh structure, strut density, and thickness in vascular response and neointimal proliferation. The *in vivo* study was essential for evaluating the systemic effects of stenting, capturing the biomechanical and biochemical alterations that computational models alone cannot fully explain.

Cellular biomechanics: AFM and Lymphocyte Analysis following the *in vivo* study, lymphocyte isolation and AFM analysis were conducted to investigate the inflammatory response to stenting and elevated metal particle contamination in peri-implant tissue. Leukocyte biomechanics were examined to detect changes in cellular properties such as stiffness, which serve as early biomarkers of peri-implant inflammation. These properties are of high importance, as alterations in cell mechanics are associated with various pathological conditions and foreign-body reactions. Circulating lymphocytes were isolated and analyzed using AFM, a powerful tool that provides high-resolution, real-time insights into dynamic cellular processes. This phase of the study was crucial in bridging the gap between the biological response and biomechanical analysis, offering a deeper understanding of stent-induced inflammation at the cellular level.

With the systemic and cellular responses characterized, in vitro studies were conducted to isolate specific mechanical effects of stents on blood properties in a controlled setting. This study built upon and expanded previous knowledge by thoroughly investigating stent-induced changes in hematological, hemodynamic and

hemorheological parameters in an ex vivo environment. The evaluation covered single and overlapping stent cases, reflecting common clinical practices, in both straight and curved geometries to simulate different coronary artery morphologies during the cardiac cycle. Two distinct biomechanical flow regimes were utilized to account for a range of physiological and more intense flow conditions, providing a comprehensive assessment of stent-induced effects. To conduct the in vitro experiments, commercially available stents were deployed in clear perfluoroalkoxy alkane (PFA) tubing, which was connected to a syringe pump and pressure sensors to replicate physiological flow conditions. Blood samples from healthy donors were analyzed to assess RBC integrity, deformability, aggregation tendencies, and whole-blood viscosity under varying biomechanical flow conditions. The presence of the stent significantly altered blood viscosity and aggregation, particularly in high-flow cases, while the pressure drop across the stented region varied depending on stent configuration and arterial geometry. An additional investigation in this study involved the measurement of pressure drop across the stented area via an in-line pressure sensing setup, an important yet complex parameter for clinical evaluation. Understanding these hemodynamic alterations is crucial for improving stent design and optimizing patient outcomes.

3.1 Ethical issues in animal study

The proposed study complied with National Legislation and EC Regulations regarding relevant issues, which include, amongst others: State aid; Protection of the environment; Equal opportunities for men and women; Protection of personal data; Non-discrimination, and Information and disclosure. The BioLISYS animal facility is a closed ecosystem with no harm to the environment and fully complies with local legislation regarding the disposal of biological waste, and the use of controlled substances. Therefore, the proposed study complied with the «Do No Significant Harm» principle as per Article 17 of Regulation (EU) No 2020/852 on the establishment of a framework to facilitate sustainable investment (EU Taxonomy Regulation) and with the European acquis and the national environmental legislation as it will not include any of the related activities.

3.2 Animal study licenses

All animal-related research work adhered to the standard and extensively tested procedures that were subjected to the inspection and approval of the Cyprus Veterinary Services, Animal Health and Welfare Division. All animal experiments were performed at the facilities of the BioLISYS lab which is fully licensed as a small animal housing facility for rodents (license no. CY.EXP.108). Approval for all procedures involving animals was granted by the Cyprus Veterinary Services (project license no. CY/EXP/PR. L7/2018).

3.3 Animals

All the procedures involving animals and their care was conducted in conformity with national and European laws and policies (DIRECTIVE 2010/63/EU of the European Parliament and the Council on the protection of animals used for scientific purposes; European Commission Recommendation 2007/526/EC on guidelines for the accommodation and care of animals used for experimental and other scientific purposes; Cyprus Regulations of 2013 for the Welfare and Protection of Animals used for scientific purposes). All animal procedures were designed in compliance with the Prepare and Arrive guidelines and with full consideration of the 3Rs. Replacement: Specific pathogen-free male CD1 mice, weighing 40±5 g (16–20 weeks old), specifically bred only for research purposes, were used for this study. The use of animal models is required for model parameterization and cross-species extrapolation that will allow for model validation with coherent clinical data. Refinement: All experimental animals were specifically bred for research and handled according to documented procedures. The animals were housed in a controlled environment with a constant temperature (22±1°C), relative humidity (60±10%), and a 12-hour light-dark cycle. Veterinary staff monitored their health regularly and cage cleaning was performed daily to maintain health and safety standards. The most refined anesthesia/analgesia protocols (both injectable and inhalable) were used to minimize discomfort and pain during procedures. Reduction: To reduce the use of animals to a minimum, experiments have been carefully planned (considering the information that should and/or can be extracted by using fewer

animals), and procedures were performed by well-trained personnel. Statistical analysis was considered in designing the experiments to ensure that the number of animals being used is not greater than those required.

3.4 Ethics permission and human participants involvement

Experiments with human participants are vital in the present study because they focus and capture important parameters of the complex, interplay of human anatomy, physiology, blood rheology and flow behavior that animal studies illustrate. Differences in geometry, cell properties and blood composition mean that results from animals often don't scale directly to clinical decisions for people. The variability due to sex in the rheological and other properties of blood flow through stent are captured in the present work. While animal research remains invaluable for invasive measurements and mechanistic insight, in vitro experimentation with human samples provides a certain degree of validity and direct clinical relevance needed to translate the results into better diagnosis, rehabilitation, and prospective outcomes.

The research protocol of this study was approved and granted permission by the Cyprus National Bioethics Committee (ref: EEBK/E/2016/18). Blood samples (30 ml) were obtained from a healthy population (8 volunteers, equal number of male and female; aged 20–50 years). All participants were appropriately informed and signed an informed consent form prior to the donation.

3.4.1 Recruitment of participants

Participants were recruited by Cyprus University of Technology staff and students, mainly for the following reasons: the large number of staff and students and the reasonable variation in age range and gender. Potential participants were given an information sheet, describing the aim of the study and other details of the participation in the project. The time allowed for reading the given information sheet 24 hours, according to the approved protocol.

Evidence suggests that factors affecting blood viscosity in healthy humans remain relatively unchanged within adulthood. It was expected to have approximately 10 participants in total in the study. This number has been shown to provide sufficiently

meaningful, though exploratory, data. The sample size is consistent with the samples used in previous research (e.g. Ostenberg et al 1997 [90] and Reihart et al 2016 [91] had 8 participants) [92]. The selection criteria were: (a) no health problem (b) over 18 years of age (c) no taking drugs.

Participants could withdraw from the study at any point, and this was clearly stated in the Participant Information Sheet. For any complaints or issues arising from their participation in the study the participants could communicate them to the Principal Investigator, Dr. E. Kaliviotis (directions were provided in the Information Sheet).

Participants will be asked to give their written consent prior to testing. A copy of the information sheet and consent form will be given to the participant. All records were kept secured in a lockable cabinet and only the researchers had access to this information. Samples were given codes for proceeding with tests and the analysis of the results.

3.4.2 Blood collection from human volunteers

Each participant would have to donate 30ml of blood (after a 12 hour overnight fast). Blood samples were collected into EDTA anticoagulant tubes. Blood samples were collected in the Bioanalysis hematology laboratory of Dr. Shammas, at Spyrou Kiprianou 23C, Limassol, or at the Biorheology laboratory in the premises of the Cyprus University of Technology (Stoa Laniti, Archiepiskopou Kiprianou, Limassol) by qualified researchers, including the author of this thesis. The Biorheology laboratory complies with the regulations for Containment Level 2, according to the Ministry of Labor (Τμήμα Επιθεώρησης Εργασίας, Κ.Π.Δ. 144/2001). The overall time for the completion of the above procedure, was between 30-45 minutes. Blood samples were immediately tested after collection, or they were stored in a lockable fridge at 4 degrees Celsius for up to 48 hours.

3.4.3 Testing of human blood samples

Testing of the samples took place within four hours of collection according to the standards set by the International Committee for Standardisation in Haematology and the International Society for Hemorheology and Microcirculation [93,94]. For samples that may be stored at 4 degrees Celsius and needed to be tested, an

appropriate time was allowed outside the fridge, before imposing the desired temperature. Upon completion of testing the remaining blood samples were disposed of according to the guidelines of the Human Tissue Authority code of Practice and the European standards

Chapter 4: Research methods and techniques

In this Chapter, the main methodological tools utilized throughout the study will be described. Details of the methodology related to the different research parts (*in vivo – in vitro* approaches) will be additionally given in the related Parts III and IV of the Thesis.

4.1 Hematology

Hematological measurements were performed using a Sysmex XT-2000i analyzer (Sysmex, Landskrona, Sweden), within 4 hours after blood collection. The following hematological indicators were determined in all blood samples: white blood cell (WBC) and red blood cell (RBC) counts, hematocrit (HCT), mean corpuscular volume (MCV), and red blood cell distribution width-coefficient of variation (RDW-CV).

The Sysmex XT-2000i is a hematology analyzer that employs a combination of impedance technology, hydrodynamic focusing, fluorescence flow cytometry, and photometric analysis to perform comprehensive blood cell analysis [95].

Flow cytometers use lasers as excitation sources to generate both scattered and fluorescent light signals, which are detected by photodiodes or photomultiplier tubes (PMTs) [96]. These signals are converted into electronic signals, analyzed by a computer, and stored in standardized data files. Each particle is assessed for light scatter in two directions: Forward Scatter (FSC) indicates relative cell size, and Side Scatter (SSC) provides information on internal complexity and granularity. Fluorescence measurements further enhance cell characterization.

The optical system consists of excitation optics (lasers) and collection optics (PMTs and photodiodes), which capture and direct signals via dichroic and bandpass filters to detect specific fluorochromes. The forward scatter versus side scatter (FSC vs. SSC) plot aids in the broad identification of cell populations in peripheral blood. Cells with smaller size, such as lymphocytes, exhibit lower FSC, while larger granulocytes display higher FSC. Similarly, cells with agranular cytoplasm (e.g., lymphocytes) have low SSC, whereas granulocytes (e.g., neutrophils, eosinophils,

basophils) exhibit high SSC due to their granular nature. Monocytes have intermediate FSC and SSC characteristics [96].

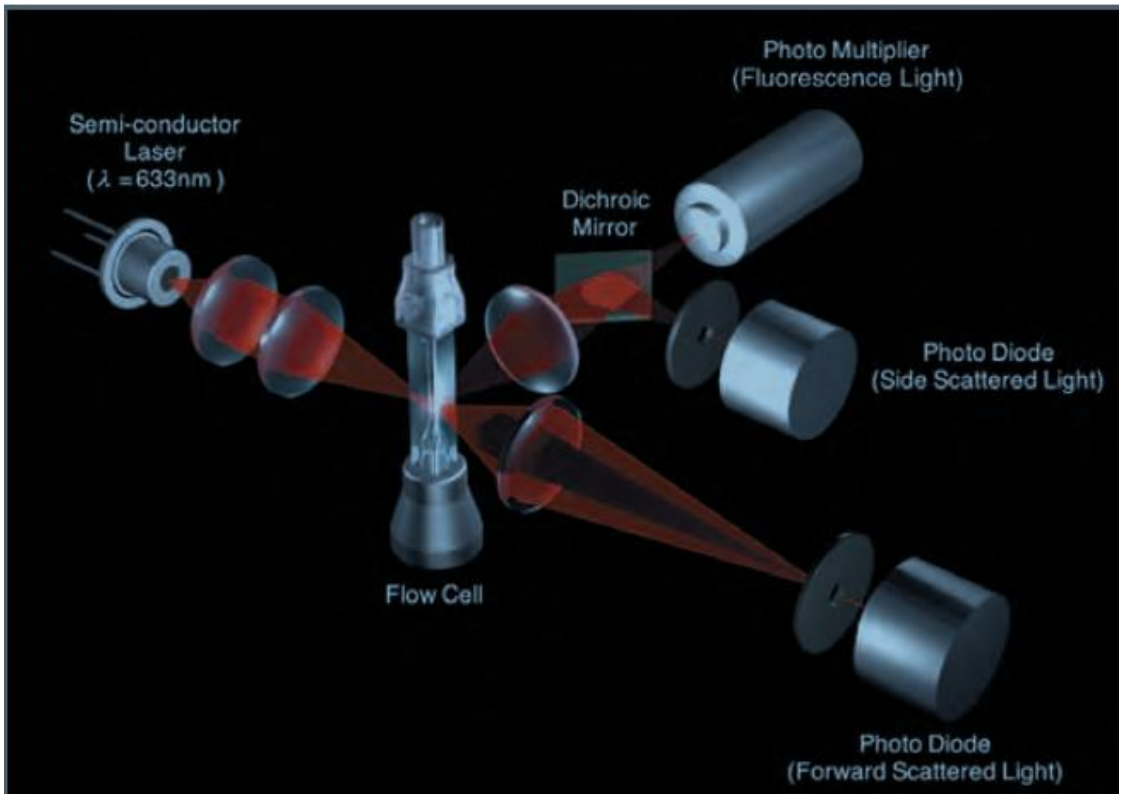

Figure 4.1: Flowcytometry using a semi-conductor laser [97].

The Sysmex XT-2000i utilizes the electric resistance detecting method, also known as impedance technology, combined with hydrodynamic focusing to measure red blood cells (RBC), platelets (PLT), mean platelet volume (MPV), mean red cell volume (MCV), and hematocrit (HCT) [95]. Hydrodynamic focusing ensures that cells pass through the center of the sensing aperture, improving measurement accuracy to detect the changes in the electric current flowing through the aperture [96,97]. MCV is obtained as an average of all RBC size measurements collected, whereas HCT is determined as the sum of all RBC size measurements, expressed in proportion to the total sample volume. Red cell indices such as mean cell hemoglobin (MCH), and red cell distribution width (RDW) are calculated. RDW is reported as both standard deviation from the mean red cell size (RDW-SD) and coefficient of variation (RDW-CV). Flow cytometry is a technique that enables rapid, multi-parametric analysis of individual cells in suspension. The Sysmex XT-2000i employs a 633 nm semiconductor laser for flow cytometry analysis of WBCs. The system

measures fluorescence and side scatter (SSC) to determine cellular properties. SSC provides information on internal complexity, including size, shape, and granularity of the nucleus and cytoplasmic granules [98]. Neutrophils (NEUT), lymphocytes (LYMPH), monocytes (MONO), and eosinophils (EOS) are identified using a combination of fluorescence and scatter measurements, while basophils (BASO) are characterized separately based on cell size and SSC properties [95].

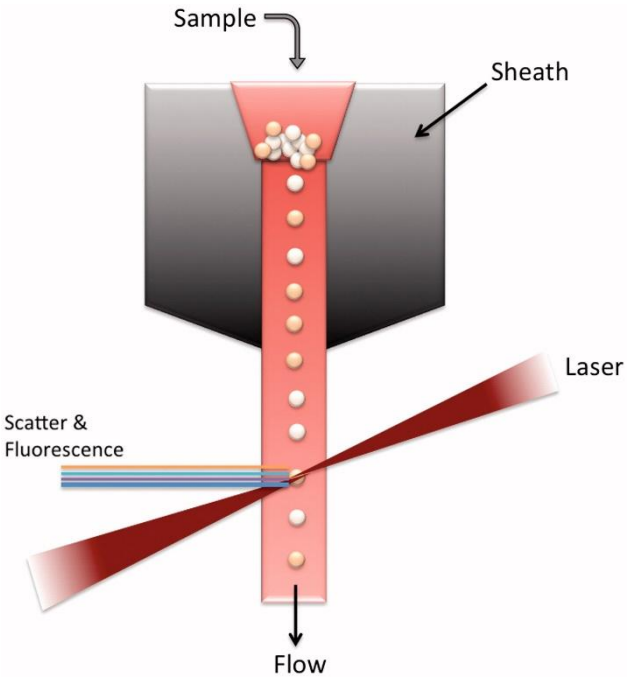

Figure 4.2: The underlying working principle of a flow cytometer [99].

4.2 Hemorheology

Blood viscosity, RBC aggregation, and RBC deformability were estimated using standard techniques at room temperature (25±0.5 °C). Below the techniques are described in detail.

4.2.1 Viscosity

Viscosity measurements were evaluated through the Brookfield DV2T instrument (AMETEK GB LTD T/A Brookfield, Stadium Way Harlow, Essex) using a cone-plate geometry [100]. Samples were applied to the viscometer plate using a

micropipette (0.6 mL volume), and measurements were initiated approximately 30 seconds after sample loading. The viscosity was assessed by gradually decreasing the shear rates from high values of approximately 10^2 s^{-1} (to ensure RBC aggregate dispersion) to lower shear rates around 10 s^{-1}, with a 30-second measurement duration at each shear rate. All blood measurements were performed using the same predefined shear rates between 251.2 and 0.975 –1 (from higher to lower shear rates). No pre-shearing was performed between shear rate points. The maximum shear stress at the highest shear rate was approximately 2 Pa for 30 seconds, significantly lower than the stress/duration threshold that could cause membrane damage and hemolysis [101]. All experiments were carried out at room temperature (25 ± 0.5°C).

4.2.2 RBC aggregation

Red blood cell (RBC) aggregation was evaluated using the Rheoscan A200 instrument (Rheomeditech, Seoul, Korea), a laser-photodiode-based system designed for the quantitative assessment of RBC aggregation kinetics. The aggregation index and amplitude (AI, AMP) was utilized as key parameters to quantify the RBC aggregation, determined by analyzing the reduction in back-scattered light as RBCs aggregate [102].

The RheoScan-A system comprises a disposable microchip featuring a disc-shaped test chamber, a laser-photodiode detection system and a magnetic stirring mechanism. The microchip, constructed from transparent plastic, is equipped with sample inlet ports and air exit channels to facilitate proper filling (Figure 4.3 right). The test chamber has a diameter of 4 mm and a height of 0.3 mm, requiring a minimal sample volume of 8 µL. A laser beam and detector are positioned perpendicularly to the chamber, ensuring precise optical measurement of aggregation dynamics.

An 8 µL volume of whole blood was injected into the chamber using a pipette through an inlet. During the measurement, the aggregation kinetics were recorded, which represent the time-dependent changes in the intensity of forward-scattered laser light from the blood sample. Initially, the stirring bar rotated at high speed, dispersing all RBC aggregates within the chamber, resulting in minimal forward-scattered light. At t = 0, the bar rotation was stopped, initiating spontaneous aggregation. This led to the formation of larger and more numerous aggregates within the blood sample, causing

an increase in forward-scattered light intensity. After 120 seconds, the intensity reached its maximum value, indicating that most RBCs in the chamber had aggregated. The aggregation parameters were subsequently extracted from the aggregation kinetics curve using specialized computer software [103].

All measurements were performed at room temperature (25 ± 0.5°C). The aggregation index (AI) was defined as the ratio between the area under the light intensity-time curve and the sum of the areas above and below the curve within the first 10 seconds [102]. Another interesting parameter is the Amplitude (AMP), which refers to the total change in reflected light intensity over the 120-second period.

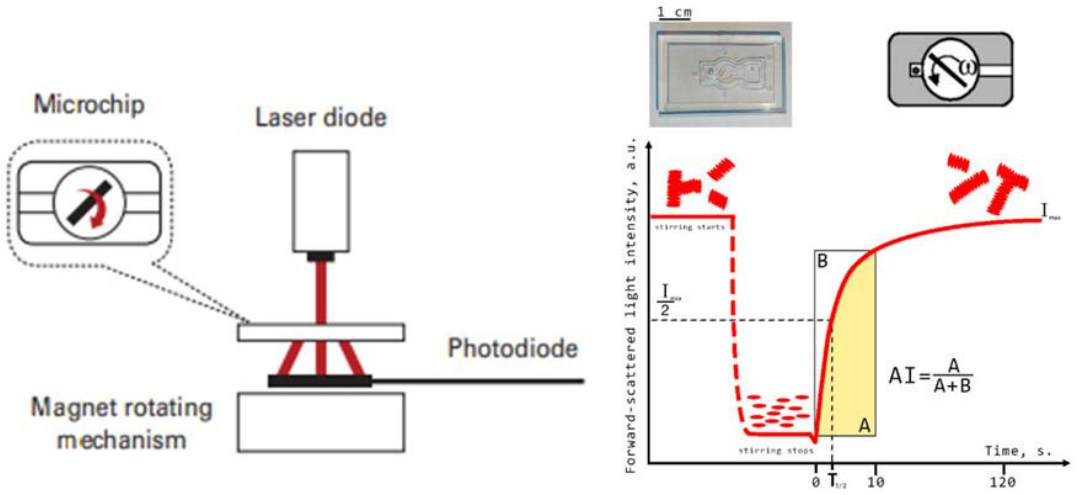

Figure 4.3: Schematic representation of diffuse light scattering used to assess red blood cell (RBC) aggregation parameters, including the aggregation index (AI) and characteristic aggregation time (T1/2). The experimental microchip utilized for RBC aggregation measurements is shown, along with its schematic layout. The kinetics curve of RBC spontaneous aggregation, obtained with the RheoScan AnD-300, illustrates key aggregation parameters: Imax, the forward scattered light intensity at maximum RBC aggregation; AI, the aggregation index, defined as the ratio of RBCs participating in aggregation during the first 10 seconds of measurement relative to the total number of cells [103,104].

4.2.3 RBC deformability

The RheoScan-D300 (Rheomeditech, Seoul, Korea) is a microfluidic-based ektacytometer that utilizes laser diffractometry in combination with microfluidic rheometry to quantitatively assess red blood cell (RBC) deformability. The device operates using a disposable microfluidic chip, through which a low RBC-to-medium

volume is perfused under vacuum-driven shear stress. As RBCs traverse the microchannel, they experience deformation into an ellipsoidal shape, proportional to the applied shear force.

RBC deformability measurements were performed using the RheoScan-D300. The instrument is based on a diffraction technique combined with microfluidic rheometry, utilizing a disposable microfluidic chip. A minimal RBC-to-medium volume is perfused through the microfluidic chip (Figure 4.4, right), at a varying pressure (vacuum-driven shearing of a thin layer of RBC suspension), causing the cells to deform in an ellipsoidal shape (Figure 4.4). The elongation index (EI) of the cells is calculated and evaluated based on the obtained diffraction patterns over a range of shear stresses [105].

A laser beam is directed through the sheared RBC suspension and the scattered light produces a diffraction pattern that reflects the average morphology of a large population of RBCs. The deformation of the RBCs is quantified by calculating the elongation index (EI), which is derived from the diffraction pattern and examined over a range of shear stresses. The EI is defined as: $EI = \frac{L-W}{L+W}$, where L and W are the long and short axes of the elliptical diffraction pattern, respectively. The EI-Shear Stress relationship provides critical insights into the mechanical properties of RBC membranes and their ability to deform under physiological and pathological conditions [105].

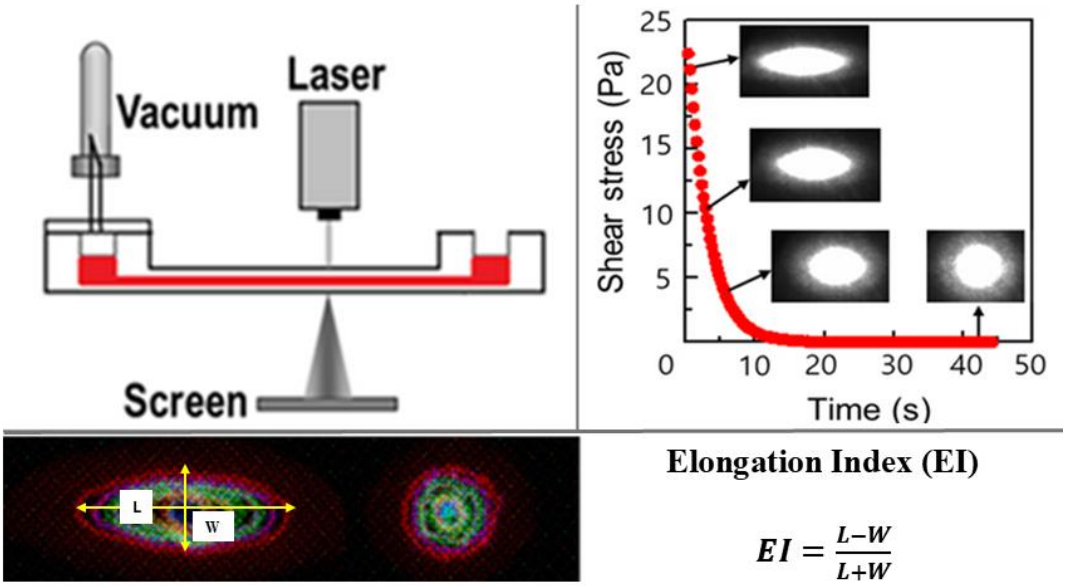

Figure 4.4: Microfluidic chip (right) used for vacuum-driven shearing of a thin layer of RBC suspension under varying pressures, inducing deformation of cells into an ellipsoidal shape [105].

4.3 Hemodynamics

4.3.1 Pressure measurements – Basic theoretical considerations

For the simple flow in the rigid circular tube and accepting that blood behaving like a Newtonian fluid due to high shear rates, the flow is assumed incompressible, laminar leading to the Hagen–Poiseuille relation with a parabolic velocity profile. The centerline speed is twice the mean velocity value, and the wall shear rate is the derivative of velocity profile at the walls [106]. Wall shear stress (WSS) is then estimated by multiplying the WSR by the blood viscosity (μ) [107]. The pressure gradient is directly proportional to the viscosity (μ) and flow rate (Q), and inversely proportional to the 4th power of the radius (r) of the tube:

$$\Delta P = \frac{8\mu LQ}{\pi r^4}$$

Entrance-length development from a uniform inlet profile to fully developed Poiseuille flow is governed by the Reynolds number (Re = ρUD/μ):

$$Le \approx 0.05 Re\, D$$

The tube/stent configuration (i.e. the position of the stent in the tube) was designed in order to avoid any entrance effects (details of the geometry are given in Part IV).

In the present work the flow in the stented tube was imposed by abruptly applying specific flow rates (please see Part IV for more details in methodology). Therefore, the pressure in the tube is expected to develop with the developing velocity profile in the tube, and therefore with the frictional forces at the walls of the tube. Figure 4.5 below shows a representative diagram of the pressure developing throughout the duration of the imposed flow.

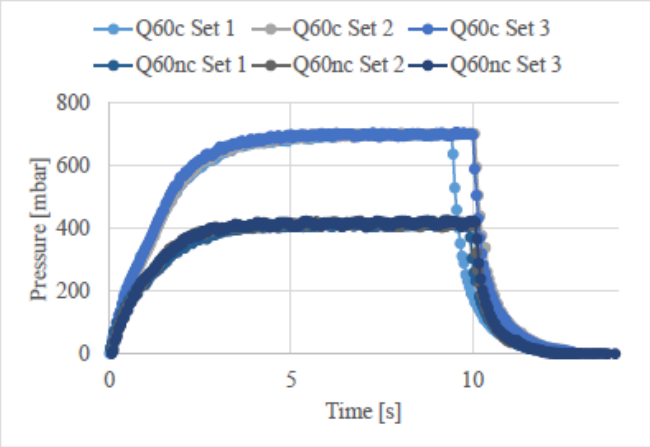

Figure 4.5: Pressure against time for a Newtonian fluid case.

For the purposes of the present work however only the maximum pressure detected (at the peak of the pressure curve) was considered for the analysis of the hemodynamics. That is the pressure values recorded at the completion of each flow cycle. Pressure drop values were averaged and the mean value out of 2 cycles was used in the analysis of the results.

Energy losses due to the stent presence in the tube are expected, and they could be captured by the pressure drop–flow rate relationship. Other losses are due to the curvature of the tube configuration, which with the stent introduce additional viscous losses and perhaps local secondary flows, and recirculation zones in the region of the stent. The aforementioned losses, however, were not possible to be quantified experimentally, as it required localized pressure sensing at the microscale level, that was not feasible in the present study.

Shear-thinning effects of blood in the pressure results are expected to be minimised, as mentioned, due to the high shear rates generated in the tube by the relatively elevated flow rates utilised. However, RBC migration could occur driving the formation of a near-wall, RBC-depleted cell-free layer, and altering the local hematocrit concentration in the tube. This may result in a Fåhræus effect (apparent hematocrit falling as tube diameter decreases). Consequently, pressure–flow relations may deviate from the linear Poiseuille law, depend on the local hematocrit, and complex fluid dynamics near the stent region, which could not be captured in the present study.

4.3.2 Fluidic system and set-up validation

The OB1 MK3+ (Elveflow, Paris, France) used in the study is a microfluidic flow controller that enables independent pressure control for up to four channels, with a range from -900 mbar to 8 bar. It supports a wide range of advanced microfluidic applications and allows direct connection of pressure and flow sensors. Elveflow's microfluidic pressure sensor of the controller functions as a gauge sensor measuring pressure relative to atmospheric pressure [108]. The MPS 3 microfluidic sensor was selected for this study. Sensors were plugged inline into the fluidic setup and paired with the pressure control system to monitor and collect the desired parameter data (see Figure 4.6). The pressure sensor specifications are presented in Table 1 and an Image of the sensor and controller is provided in Figure 4.5 and Figure 4.6.

Table 4.1: Pressure sensor specifications.

Microfluidic pressure sensor MPS 3	
Sensor range	2 bar
Pressure range	-15 to 30 psi
Maximum overpressure	60 psi
Pressure accuracy liquids	Up to ± 0.2% max range
Operating temperature	- 40 °C to +85 °C
Repeatability & hysteresis %span	± 0.2
Specified temperature range	0 °C to +50 °C

Figure 4.6: Microfluidic pressure sensor και flow controller (Elveflow) [108].

An initial validation of the pressure system was performed using different fluids including distilled water (DW), xanthan gum solution (XG), glycerin solutions (GL), and finally a preliminary test with blood. All samples were tested at a range of flow rates (20, 40, and 60 ml/min) in two conditions, a constricted (e.g. DWc) and non-constricted (e.g. DWnc) tubing. For the constricted case a tube element of dimensions inner diameter 0.83mm, outer diameter 1.2mm, length 6 mm was placed in the tube at a length of 6mm to represent the stenting geometries. The maximum pressure was measured for three repetitions of the imposed flow rates, and the mean value was calculated.

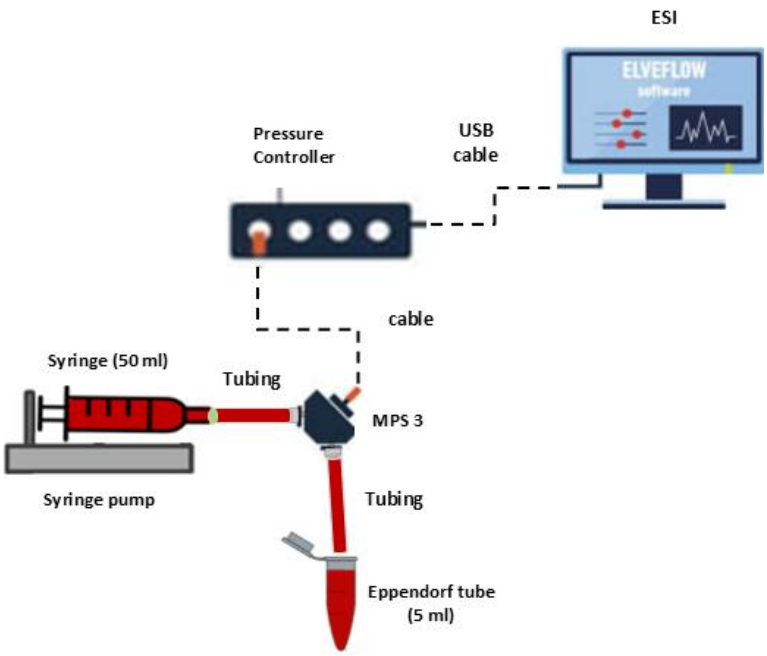

Figure 4.7: A diagrammatic representation of the system configuration with a microfluidic pressure sensor (not drawn to scale).

Figure 4.8 summarized the validation pressure results from the four different fluids (distilled water, glycerin, xanthan gum and blood) in both conditions (constricted vs non-constricted). Figure 4.8 illustrates that the linear relationship between pressure and flow rate is retained for the Newtonian cases for the whole range. Importantly for the non-Newtonian fluids (xanthan gum and blood) the linearity and slope of the curves is similar to those of the Newtonian fluids for the range 40 to 60 ml/min. This implies that the non-Newtonian effects are suppressed due to the high flow rate as mentioned earlier.

The presence of constriction is seen to affect the pressure in all different fluid cases, and the pressure drop of glycerin with high viscosity and blood have a tendency to rise between constricted and non-constricted cases more than the other cases.

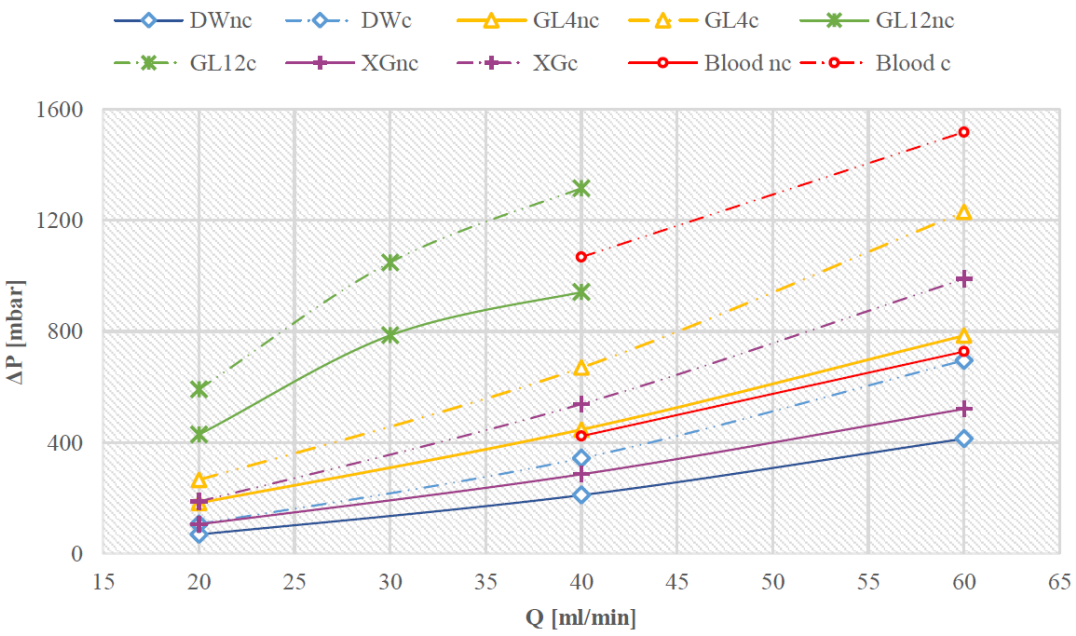

Figure 4.8: Collective averaged pressure differences plotted against all flow conditions and for the two flow configurations [109].

Table 4.2: Mean pressure differences.

	Mean pressure differences				
Flow rate	**DW**	**GL4**	**GL12**	**XG**	**Blood**
Q20	52.3	42.8	38.1	70.4	-
Q30		-	33.4	-	-
Q40	63.3	49.0	39.6	89.3	152.2
Q60	68.2	56.0	-	91.3	108.6

The data in the Table 4.2 show that introducing a constriction systematically elevates the mean pressure for all fluids and flow rates, with the magnitude of this increase depending on both viscosity and rheological behavior. Newtonian fluids (DW, GL4, GL12) exhibit moderate pressure rises as flow rate increases, and the more viscous glycerol solutions consistently reach higher mean pressure differences than distilled water at the same flow conditions, in line with the Hagen–Poiseuille relation for viscous flow in tubes.

Non-Newtonian samples display the strongest sensitivity to constriction: XG already presents the highest mean pressure difference at Q20, while blood exhibits the largest pressure increases at higher flow rates (Q40 and Q60), exceeding all other fluids in the table. These results indicate that both increased flow rate and constricted geometry amplify pressure demands, with non-Newtonian and higher-viscosity fluids showing disproportionately large pressure elevations compared with Newtonian, lower-viscosity solutions.

The validation studies have confirmed that the system can capture the expected behavior of the pressure/flow rate relationship for conditions where the flow is dominated by the Newtonian nature of the fluids.

PART III: *In-vivo* approach

This part elaborates in the *in vivo* approach of the study. It includes two chapters: Chapter 5 investigates the effects of stent implantation on hematological and hemorheological parameters, while Chapter 6 examines the inflammatory response due to stent implantation with a particular focus on lymphocyte stiffness. Within the chapters additional and more detailed information regarding literature review and methodology is provided.

Chapter 5: *In vivo* investigation on the effects of stent implantation on hematological and hemorheological parameters

5.1 Introduction

This chapter of the PhD work investigates, in an *in vivo* approach, the effects of stenting and the implantation time-course on hematological and hemorheological parameters that could potentially compromise the device's functionality and longevity. *In vivo* studies for assessing the effect of stenting on hematological indices are available in the literature (see for example studies [110] and [111]), however, the correlation with the hemorheological factors is a relatively unexplored topic. The most important hemorheological factors include red blood cell (RBC) aggregation and deformability, as they influence the non-Newtonian nature of blood. The RBCs' ability to deform and change their shape allows effective circulation and oxygen delivery in the circulatory system; decreased deformability leads to a fall in tissue oxygenation [112]. Moreover, RBC aggregation is directly correlated with hemostasis and affects the leukocytes, platelets, and their interaction with endothelium [113], [53]. Deformability and aggregation are often interdependent and aggregation alterations are often associated with cell shape changes. Szapary et al., 2009 investigated the changes in the hemorheological characteristics (red blood cell aggregation) and platelet aggregation of patients with carotid stenosis following endovascular treatment. The study showed that in the first days after the intervention, a pathological change in hemorheological parameters (plasma viscosity, hematocrit, and plasma fibrinogen concentration) is present, however, after a month the parameters returned to normal levels [114].

Regarding the influence of the stent design, it is already established that specific characteristics, namely mesh design, strut density and strut thickness, etc. play a significant role in the vascular response, restenosis, and other effects [100],[69]. Studies with animal models signified that these characteristics affect the experimental vascular injury and neointimal proliferation [70].

Presently, most of the work on this issue is based on simplified theoretical models and computational fluid dynamics analysis on local hemodynamics [115], lacking *in vitro* and *in vivo* experimental verification with blood samples. Studies suggest that red blood cells undergo mechanical and biochemical changes during blood passage through medical devices [115–117]. It is of great importance, therefore, to evaluate the effects of the stent presence on the hematological and hemorheological profile of the host. This part of the study aimed to evaluate in an *in vivo* setting, the effects of stenting and the implantation time-course on hematological and hemorheological parameters that could potentially compromise the device's functionality and longevity.

5.2 Methodology

5.2.1 Stent design

Custom-made self-expanding nitinol stents (Admedes GmbH, Pforzheim, Germany), 0.7 x 3.3 mm in dimension, with a closed-cell design and a diamond-shaped pattern, were used (please see the study by Kapnisis et al [68] for more details). Stent samples were mechanically polished to remove the heat-affected zones from laser cutting before undergoing further surface processing. Two groups, differing in material surface condition and processing steps, were prepared: heat-treated (HT) and electropolished (EP), with a resulting strut thickness in the range of 20-40 μm, as shown in Figure 5.1.

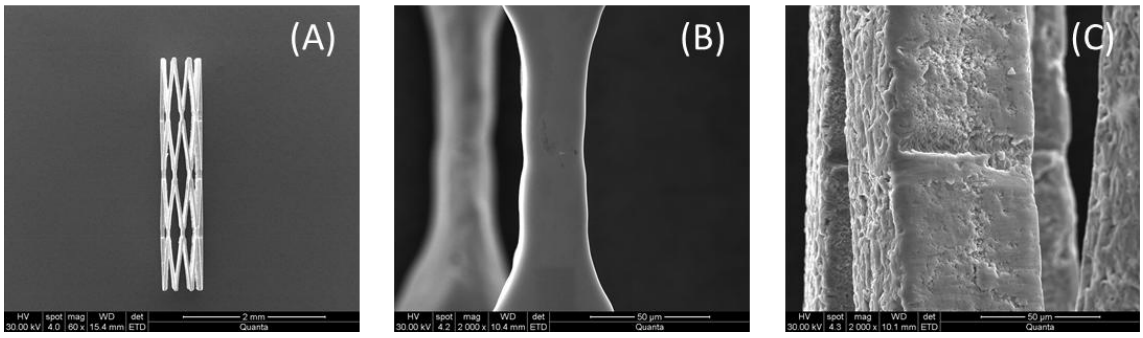

Figure 5.1 Representative SEM images of the stent device indicating: (A) The closed-cell design with a diamond-shaped pattern (at x60 mag); Representative surface morphology of (B) the HT and (C) the EP stent (both at x1200 mag).

5.2.2 Animals

Information regarding animal studies has been provided in Section 3. Animal experiments were carried out with approval from the Cyprus Veterinary Services (license CY/EXP/PR.L09/2019) and complied with relevant national and European regulations on the care and use of animals for scientific purposes. The study used pathogen-free male CD1 mice (16–20 weeks old, 40 ± 5 g) bred specifically for research. The animals were housed under controlled conditions, including regulated temperature (22 ± 1°C), humidity (60 ± 10%), and a 12-hour light/dark cycle.

5.2.2.1 Mouse stenting procedure

Operative procedures were performed following the experimental protocol first reported by Simsekyilmaz et al. [118] and modified accordingly by Kapnisis et al. [25] which describes a rapid and accessible procedure of stent implantation in mouse carotid artery. Animals were pre-treated for 48 h with aspirin (75 mg in 250 mL drinking water), which was discontinued 48 h postoperatively. General anesthesia was induced by intraperitoneal injection of 100 mg/kg b.w. ketamine and 10 mg/kg b.w. xylazine. A small median incision was performed at the ventral neck area and the left common carotid artery was exposed. Following arteriotomy on the external carotid artery, a polymeric guiding catheter containing the stent was introduced, and after reaching the desired position in the common carotid artery, the tube was pulled back over a guidewire to allow the shape-memory expansion of the stent. After stent deployment, the wound was closed and the animals were allowed to recover. Two

testing groups (HT and EP stented) and one control group (healthy, non-stented) were prepared for subsequent evaluation, as per the experimental plan illustrated in Figure 5.2.

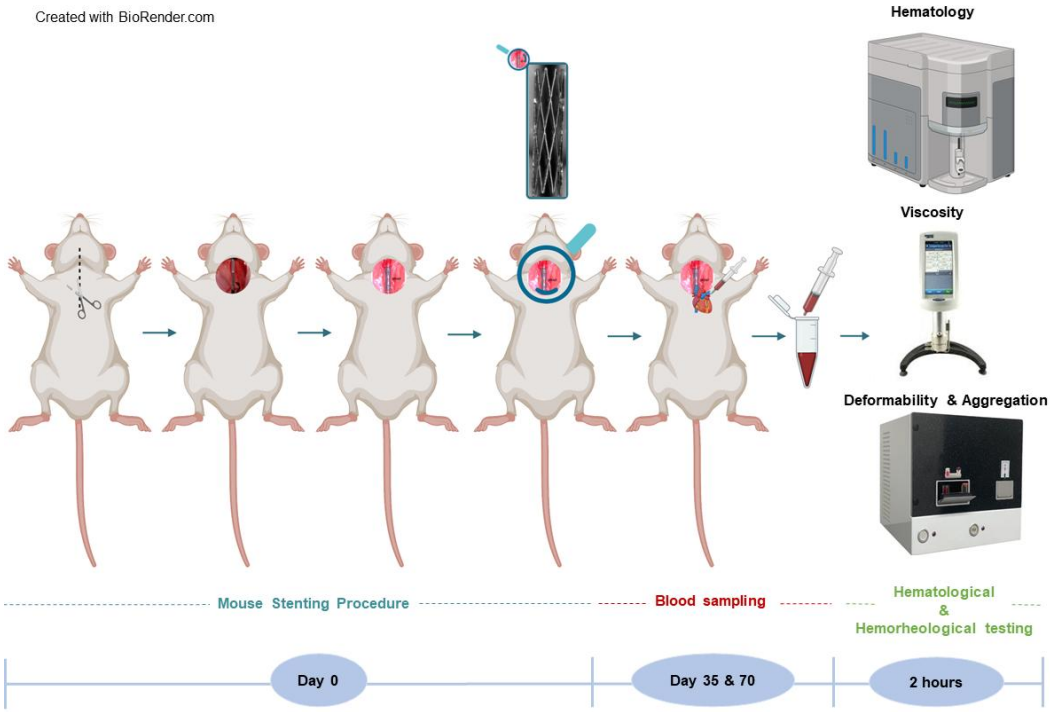

Figure 5.2: Schematic illustration of the experimental design. Overview of the stenting surgical procedure at day 0, the whole blood sampling at day 35 and 70 (5- and 10-weeks post-implantation respectively) and the hematological and hemorheological evaluation 2 hours after blood collection.

5.2.2.2 Blood sampling and preparation

Whole blood (0.5 - 1.0 ml per animal) was withdrawn from control (healthy, non-stented; n=7) animals before implantation (t=0) and from stented animals at 5- and 10-weeks post-implantation (n=3 per time point). Blood collection was performed by direct cardiac puncture under anesthesia, using citrate-dextrose solution (Sigma-Aldrich, MI, USA) prefilled syringes at a ratio of citrate-to-blood of 1:9. Following blood aspiration, the needle was removed to avoid cell shearing and the fluid was gently introduced into a 1.5 ml Eppendorf tube, with the tip of the syringe in contact with the tube wall to minimize drop splashing. The tube was inverted several times by hand to ensure adequate blood mixing with the anticoagulant.

5.2.3 Hematology

The hematological analysis conducted in this section utilized the same methodology detailed in the previous chapter 4, section 4.1. All blood samples were analyzed within 4 hours of collection using the Sysmex XT-2000i hematology analyzer (Sysmex, Landskrona, Sweden. Parameters assessed included white blood cell (WBC) and red blood cell (RBC) counts, hematocrit (HCT), mean corpuscular volume (MCV), and red blood cell distribution width-coefficient of variation (RDW-CV).

5.2.4 Hemorheology

The experimental methodologies applied in this section are identical to those described in detail in the Section 4.2, specifically in the context of hemorheological assessments. These include the evaluation of blood viscosity using the Brookfield DV2T viscometer with cone-plate geometry under controlled shear rates, red blood cell (RBC) aggregation analysis via the Rheoscan A200 system based on laser-photodiode detection, and RBC deformability measurements using the microfluidic-based RheoScan-D300 ektacytometer. All procedures were conducted at room temperature (25 ± 0.5°C), using consistent sample preparation protocols and standardized measurement conditions as previously outlined.

5.2.5 Statistical analysis

The differences between the five groups of samples examined in the study were compared with a one-way ANOVA test. All measurements were reported as mean± standard deviation (SD) and considered significant when $p < 0.05$.

5.3 Results

5.3.1 Hematological evaluation

Due to inconsistent changes among the two groups, differing in surface treatment (HT vs. EP), all the results were analyzed collectively at each time point. However,

to account for the potential influence of surface modification on hematological and hemorheological parameters, a separate analysis was performed based on stent surface treatment. These results are provided in detail in Appendix I: *In vivo*- Results. The overall effect of stenting on the various hematological indices is depicted in Figure 5.3, along with the physiological range for each parameter, indicated with gray-lined boxes. Variations in the hematological indices when blood is collected at different sampling sites were previously reported [70], and data suggest that blood cell counts and other indices are found significantly lower in heart blood compared to eye and tail vein blood. Therefore, the tendency of some indices (RBC, WBC counts, and HCT) to reside at the lower end of the physiological range could be explained in this manner. Even though no statistically significant differences were observed between the tested samples ($p>0.05$), in some cases notable trends were apparent due to the stenting time course. Our data demonstrated an increase in RBC counts and slightly elevated HCT at 10 weeks post-stent implantation, and increased RDW-CV, contrary to a slight reduction in MCV. These findings could also account for the higher RDW-CV, denoted at the same time point. In addition, WBC counts were used for assessing the inflammatory status [119] of healthy (control) and stented CD1 mice. The analysis revealed a rising trend over time, with HT-stented mice denoting notably higher WBC counts than EP (data not shown), suggesting a gradually increasing implant-included inflammatory response.

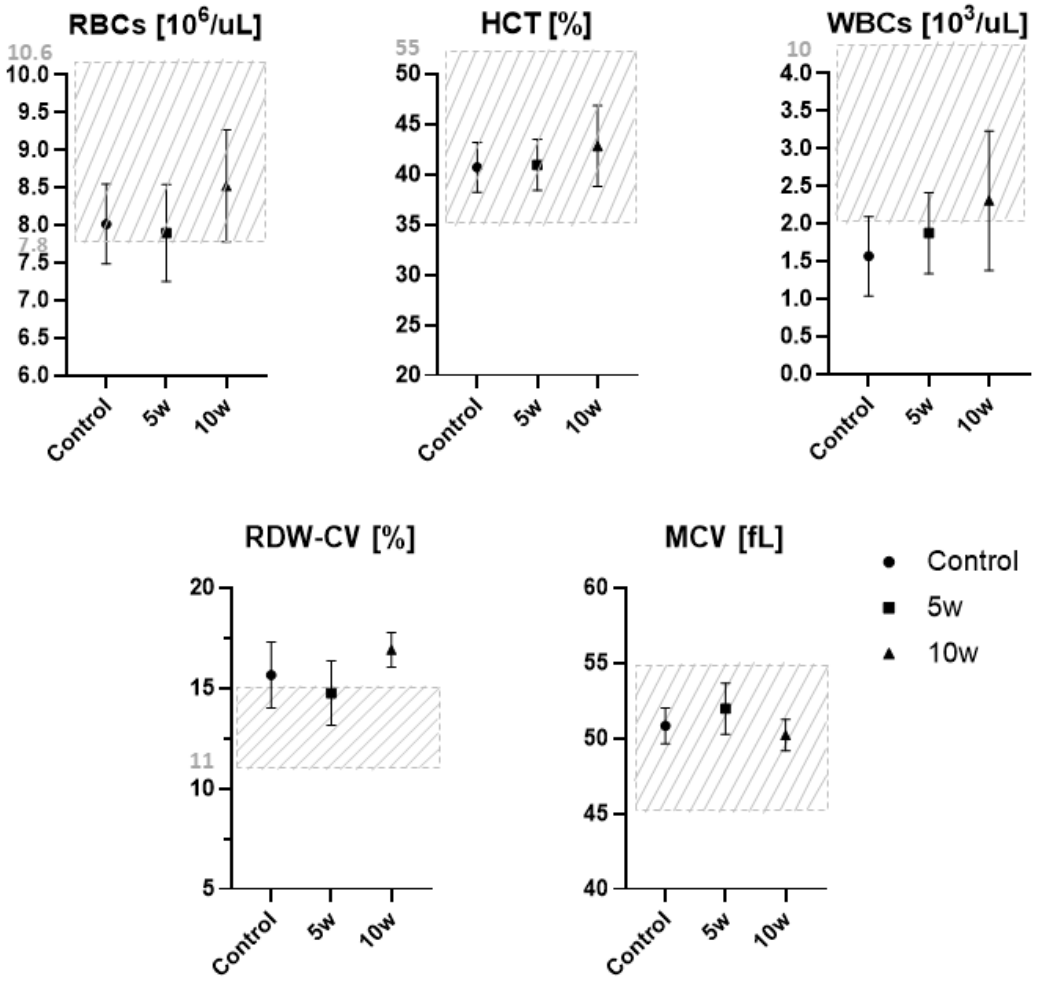

Figure 5.3: Effect of time-course stenting on hematological parameters. Values are expressed as the mean ± SD and the physiological range is indicated with gray-lined boxes.

5.3.2 Hemorheological evaluation

5.3.2.1 Viscosity, RBC aggregation, RBC deformability

Stent-induced alterations in RBC aggregation and deformability are expressed by the indices AMP and EI_{max} respectively and are presented in Figure 5.4. Although not statistically significant, a marked decrease in the AMP index is observed at 10 weeks, compared to the control and 5-week cases (jointly evaluating HT and EP stented cases). RBCs showed a subtle increase, followed by an analogous decrease in deformability over the 10-week implantation period, compared to the control case. This fluctuating trend could be due to biological, but also mechanical factors such as the shear stress and the period of exposure to stress, which play a role in the RBC

membrane properties and deformability [120–122]. It is noteworthy that the decreased RBC deformability noted at 10 weeks also corresponds well with the distinct increase in RDW-CV shown in Figure 5.3.

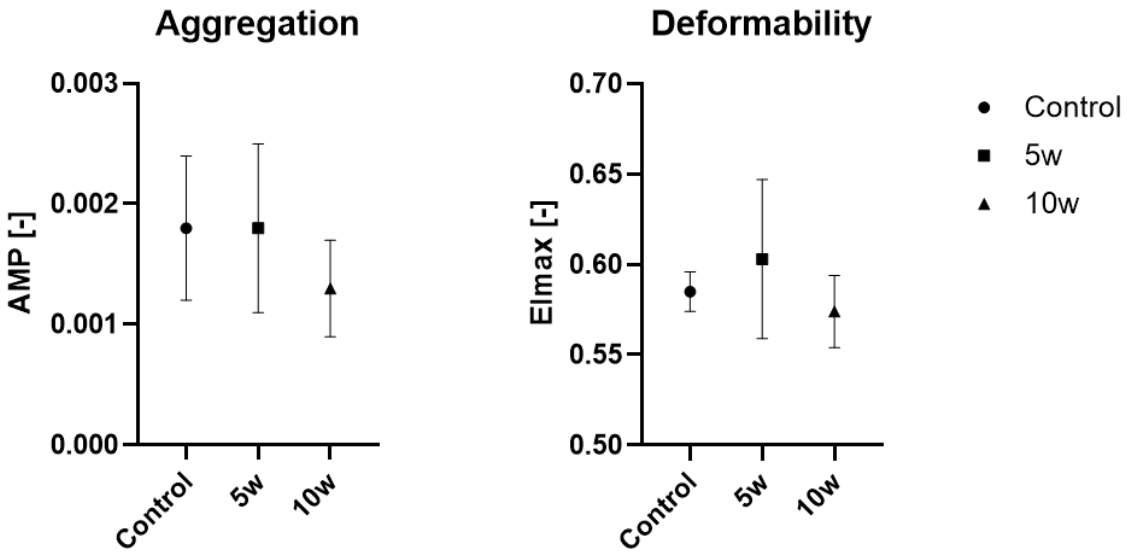

Figure 5.4: Stent-induced alterations in RBC aggregation and deformability.

The viscosity data in Figure 5.5 are presented as normalized (η^*) with the high-shear viscosity (η_∞) values ($\eta^* = \frac{\eta}{\eta_\infty}$), for a shear rate range of 0.975 to 252.2 s-1. Therefore, η* is effectively a non-dimensional index of the non-Newtonian nature of the fluid. Figure 5.5 demonstrates the shear thinning and non-Newtonian nature of blood, which is in general agreement with the literature [53]. When assessing the η* differences between the control samples and the longest implantation case (Week 10), in view of the hematology data shown in Figure 5.3 and Figure 5.4, the following observations can be made: the viscosity of blood is negatively affected by increased hematocrit, and impaired RBC deformability, although RBC aggregation shows a decrease at Week 10. It should be noted, however, that the RBC aggregation appears generally very low in mice and other rodents, and this is the case in the present work (very low AMP values for all samples). Nevertheless, the RDW-CV index demonstrates an improvement at Week 5, suggesting enhanced blood fluidity (lower viscosity) in contrast to the cases with elevated RDW-CV levels in Week 10, which show slightly higher viscosity at the lower shear rates. The increased RDW-CV has

also been linked [123] with increased interaction between blood cells and the vascular wall.

When comparing the differences in η* between the control and the stented cases collectively (at both weeks 5 and 10), notable differences appear below approximately 7 s-1: the η* difference is increasing with the decreasing shear rate, indicating an enhanced non-Newtonian behavior for blood for the stented cases. No statistical significance is observed for the η* differences between control and stented cases. Above approximately 30 s^{-1}, η* is almost identical for all control and stented cases.

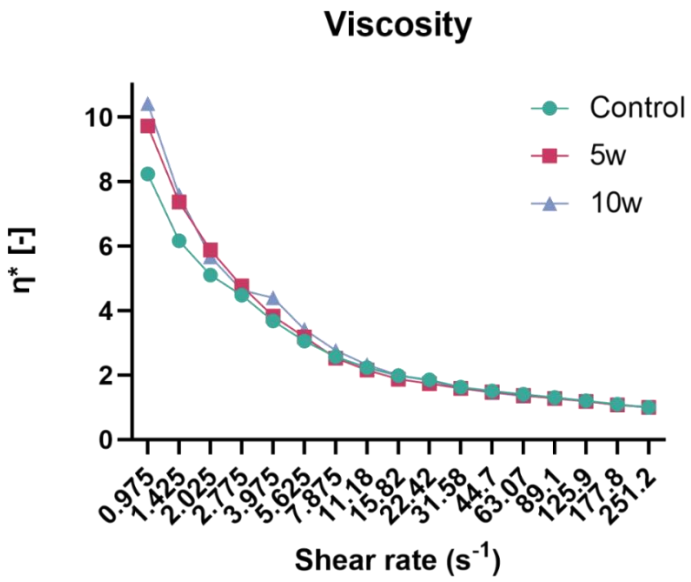

Figure 5.5: Normalised viscosity η* against shear rate. Control samples in comparison with the stented cases at two different time points.

5.4 Analysis and discussion

The present part of the study showed that various hematological factors and rheological properties of blood in mice may be associated with device implantation, and in some cases, with the time course of stenting. To avoid any non-stent-related effects associated with the implantation procedure, such as endothelial layer damage caused during catheter guidance, it was decided to investigate for mid (5 weeks) to

late stages (10 weeks) of stent-related hemorheological complications, thus allowing adequate recovery time for operated animals.

Even though the cardiovascular stent is used for restoring blood flow, it locally acts as a suppressive factor, inducing hypoxic conditions for the arterial layers around the stent [124]. In the present results, the observed increasing trend in RBC count can be explained by hypoxia, which leads to the rise of erythropoietin. Bone marrow produces mature RBCs, which are stimulated by erythropoietin, leading to an increase in hematocrit also [10]. Hypoxia condition can be also related to the decreased elongation index in the 10-week stented case [125]. Also, the wound healing after the stent implantation itself might influence blood cells. In particular, stent placement induces vascular damage and disrupts local blood flow, resulting in endothelial dysfunction. This dysfunction initiates the activation of inflammatory cells, enhances thrombogenicity, and decreases the presence of β-lipoprotein, leading to its accumulation within the neointima. The apoptosis of macrophages and smooth muscle cells plays a role in the development of a necrotic core and calcification. Furthermore, less mature endothelial cells with increased permeability promote the migration of monocytes [126,127].

The mouse RBC has a half-life of 38 to 52 days, which is shorter than that in humans and other veterinary species. Due to shorter RBC half-lives in mice, processes affecting red cell mass and volume have more rapid effects in mice than in other species [11]. A decreased RBC count after 5 weeks of implantation could occur due to secondary conditions like immune-mediated hemolysis and inflammatory disease [128].

Regarding the WBC presence (WBC count), shown in Figure 5.3 to lie outside the physiological range for the control and 5-week cases, it is important to note that the total number of white blood cells per unit volume is significantly lower in the heart blood compared to eye and tail vein withdrawal [129]. In general, differences are reported in all cell types and indices, including RBCs, platelets, and hematocrit, which are found significantly higher in the tail compared to heart blood [129].

The increased number of WBCs in the implanted cases indicates that inflammation is present. The WBCs participate in the inflammatory processes and are used as a nonspecific marker of inflammation [130,131]. Moreover, oxidative stress is

apparent in the stented group, which injures erythrocytes and reduces erythrocyte survival, thereby leading to RDW elevation [132,133]. Moreover, WBCs are important producers of inflammatory cytokines, and it has been thought that increased cytokines may inhibit the maturation of erythrocytes in the bone marrow and may cause increased RDW values in cardiovascular diseases [134,135]. Furthermore, the oxidative stress, inflammation, and activation of the neurohormonal system may be the possible mechanism that disturbs the RBCs membrane leading to increased RDW [136]. All of these causes may contribute to stent thrombosis and restenosis [137,138].

The hemorheological results observed in Figure 5.4 are in general agreement with the literature. The decreased deformability (EI_{max}), seen between the 5- and 10-week cases, is followed by a decrease in the RBC aggregation. Reasons for the disproportional effect of decreased RBC deformability on aggregation may include RBC membrane/cytoskeleton dissociation, which has been suggested to affect the correlation between the two RBC properties [136].

This slight decreasing trend of RBC deformability in the 10-week sample group can be due to mechanical fatigue and biological factors. In terms of mechanical fatigue, it is known that the shear stress and period of exposure to stress play a role in the RBC membrane properties and deformability [129]. It has been shown for example, that stresses of approximately 30 Pa can have a statistically significant effect on RBC deformability for a period of exposure of approximately 30 seconds and that an exposure of 4 seconds to approximately 64 Pa, can result in a significant change in RBC membrane stiffness [139]. It is noteworthy that the decreased RBC deformability corresponds well with the distinct increase in RDW-CV observed in the case of 10 weeks samples Figure 5.3. Indeed, studies suggest that mechanical stresses could influence the RDW more than the MCV of the RBCs; the study of Cahalan et al. [140] showed that the recirculation of RBCs and the exposure to mechanical forces can influence their membrane integrity and volume through a dehydration mechanism. Altered RBC stiffness occurs in many numerous pathologies [134], and in general, could lead to decreasing tissue perfusion and oxygenation and thereby further contribute to the impaired pathophysiology [137]. Further, normal senescent RBCs which have stiffer membranes, show difficulty

moving through the arterial passage and are eventually filtered out by macrophage phagocytosis [141]. Similar negative effects in blood circulation are expected due to the alterations in RBC aggregation. Baskurt 2008 has illustrated that vascular resistance is affected (although non-monotonically) by the increase of RBC aggregation and the decrease in RBC deformability [142].

Szapary et al. also observed elevated RBC aggregation in cases of human carotid stenting after implantation, compared to the baseline cases [85]. In the aforementioned study, RBC aggregation is influenced at the early stages after stent implantation, however, in the present case, the aggregation index and decreases in the 10th week. The degree of RBC aggregation is anticipated to be influenced by the affected deformability of RBCs, as a decrease in RBC deformability can lead to a decrease in RBC aggregation, as in the case of 10-week stenting [25,137].

The main determinants of blood viscosity are hematocrit, plasma viscosity, RBC aggregation, and deformability [134,143]. The concentration of WBCs contributes to a much lesser extent to the viscosity of blood. Ohta et al., 2005 observed that stent placement induces changes in the dynamic viscosity of blood [144]. This finding is in line with the results shown in Figure 5.5 where an increasing trend in η^* is observed below 7.875 s^{-1}. The outcomes in this study are generally consistent with the existing hemorheology knowledge, indicating that a decrease in RBC deformability (at 10 weeks), in conjunction with increasing RBC count and hematocrit and increasing WBC count and RDW-CV, leads to an increase in the non-Newtonian extent of blood viscosity [145]. However, RBC aggregation is observed to decrease between weeks 5 and 10, which might be the result of decreased deformability, although generally, all cases show very low aggregation tendencies (AMP between 1 to 2x10-3 units). Blood viscosity alterations are also expected to influence blood circulation; however, animal studies show different effects when considering different organs. For example, blood flow in the brain spleen, and intestine of the dog has been found to decrease when increasing blood viscosity, whereas liver blood flow in the same animal was found to increase [146].

Another noteworthy observation in Figure 5.3 is the decreased MCV from Week 5 to Week 10. One important implication of decreased MCV is the possibility of adverse

effects in the stent area; Tscharre et al. showed that lower MCV in stented patients increases the risk of restenosis [147].

The results of the present study provide useful information however caution is needed when relating them to the human population. In terms of human circulatory physiology, during the left ventricular systole, the contraction of myocardial fibers creates a distinctive characteristic in the coronary blood flow, where the flow is also impeded [148]. The coronary arteries are the first branches of the aorta, divided into smaller arteries and arterioles, forming a comprehensive system that serves specific functions [148]. In a human adult heart, the resting left coronary blood flow typically ranges from approximately 0.5 to 1.0 mL/min/g. In contrast, the average blood flow in the right ventricle is considerably lower, typically ranging from approximately 0.3 to 0.6 mL/min/g [149]. The healthy carotid artery in the human system has a diameter range of 6 mm – 8 mm, compared to the mouse which spans from 0.3 to 0.5 mm [43]. The large and accessible carotid artery serves as a prominent vessel in mice, making it an excellent model for investigating disturbed blood flow profiles and induced arterial thrombosis in response to various stimuli in research studies. The average flow rates in mouse carotid arteries typically range from 0.24 to 0.7 mL/min [150] while in a human carotid artery, the blood flow is 7.2 mL/s [151] and the average wall shear rate ranges between 280-500 s^{-1} [152]. Numerous studies have examined the WSR value in the carotid arteries of mice resulting in a range between 1300 and 4000 s^{-1}, indicating an inverse relationship between animal size and wall shear stress on account of small vessel diameter [43,153]. As a general principle, mice exhibit a size that is approximately 15 times smaller than that of humans, with their arterial dimensions following a proportional reduction as well [43].

Based on the above, the RBC flow/stress exposure in the stented region is most probably much higher in mice compared to humans. Therefore, impaired cell deformability and the observed phenomena are intensified in the mouse model and are less likely to affect the hemorheological profile in a human stented carotid artery. That being said, the *in vivo* setting studied in the present study could resemble the clinical conditions developed in the cortical branches of the anterior cerebral artery, which have a sub-millimeter diameter, and thus further investigation is warranted on this aspect.

Chapter 6: Inflammatory response due to stent implantation - Lymphocyte stiffness

6.1 Introduction

In this part of the work, a multilevel approach was employed to investigate the inflammatory response associated with implant-induced processes using a mouse stent implantation model. The study focused on key biological parameters, including leukocyte biomechanics, to gain insights into the progressive nature of inflammation in peri-implant vascular tissue. Given that alterations in cell biophysical properties such as morphology, nanostructure and stiffness are closely linked to pathological conditions and foreign-body reactions, their assessment is crucial in understanding the impact of stent implantation on vascular health. To achieve this, Atomic Force Microscopy (AFM) was employed to characterize the mechanical properties of lymphocytes. AFM, a powerful tool for real-time cellular analysis, lymphocyte isolation and culture methods were optimized to ensure precise biomechanical characterization.

6.2 AFM- General principles

AFM is a widely used scanning probe microscopy technique capable of obtaining both topographical imaging at single or sub-nanometer resolution and various mechanical properties such as elasticity and viscosity. The fundamental working principle of AFM is based on the interaction between the AFM cantilever probe and the sample surface, where the probe approaches, interacts, and retracts from the sample to measure forces and generate high-resolution images. Despite the diversity of AFM methods and configurations, the core components of most AFM systems remain similar, comprising a cantilever with a sharp probe, an optical detection system utilizing a laser and photodetector, piezoelectric actuators for precise movement control, and a feedback control system to optimize tip-sample interactions [154].

The AFM cantilever plays a critical role in determining the imaging resolution and mechanical measurements. Typically made from silicon nitride or silicon, cantilevers come in various shapes, sizes, and stiffness levels, affecting their response to different sample types. For biological specimens, softer cantilevers with spring constants below 1 N/m are commonly used to minimize interaction forces and prevent damage to delicate samples. The cantilever tip varies in geometry, with pyramidal, conical and spherical shapes. While sharp pyramidal and conical tips provide high-resolution imaging, spherical tips are often employed for mechanical property measurements due to their well-defined contact area, which simplifies force modeling using standard contact mechanics equations.

The interaction between the cantilever and sample surface results in deflections of the cantilever, which are detected using an optical lever system. A laser beam is reflected off the back of the cantilever onto a four-quadrant photodetector, enabling precise measurement of the cantilever's deflection. By calibrating the cantilever's spring constant, these deflection measurements can be converted into force values, allowing for the extraction of mechanical properties such as Young's modulus and adhesion forces.

To achieve high-resolution imaging and force measurements, AFM systems employ piezoelectric actuators that control the movement of the cantilever in the x, y and z axes with nanometer precision. These piezoelectric elements utilize their intrinsic material properties to enable highly accurate positional adjustments. Many AFM systems incorporate a tube-shaped piezo scanner that simultaneously controls motion in all three dimensions; however, to minimize cross-talk and artifacts, some systems use independent piezo actuators for lateral and vertical movement. The x-y piezo actuators raster scan the sample, with the fast scan direction following a triangular motion while the slow scan direction incrementally shifts the probe. The z-axis piezo actuator is responsible for maintaining a controlled approach and retraction of the cantilever, ensuring accurate force measurements and minimizing tip-induced damage.

A crucial aspect of AFM operation is the implementation of a feedback loop to maintain stable imaging conditions and obtain reliable mechanical data. In contact mode, the deflection of the cantilever is continuously monitored and compared to a

predefined setpoint to regulate tip-sample interaction forces. In dynamic modes such as tapping mode, the amplitude or phase of the oscillating cantilever is monitored, and deviations from the setpoint are corrected through proportional and integral gain controllers. Proper tuning of these feedback parameters is essential for achieving clean, high-quality imaging and maintaining stable scanning performance, particularly at high speeds.

AFM is widely used in biological research due to its ability to probe the mechanical properties of living tissues in physiologically relevant conditions. Unlike traditional imaging techniques such as SEM and transmission electron microscopy (TEM), which require complex sample preparation, AFM can be performed in liquid environments without damaging or altering the sample. This makes it particularly valuable for studying soft biological materials such as cells, tissues, and biofilms [155].

Two commonly employed AFM imaging modes are contact mode and tapping mode. In contact mode, the probe maintains continuous contact with the sample surface, recording deflections as it scans [156]. However, this mode exerts significant lateral forces, which can damage soft biological samples. Tapping mode was developed to mitigate this issue by oscillating the cantilever near its resonance frequency, allowing the tip to intermittently contact the surface. This reduces lateral forces and minimizes sample deformation while preserving high-resolution imaging capabilities. Mechanical properties can be obtained by analyzing force-distance curves, which describe the cantilever deflection as it indents and retracts from the sample. These curves can be further processed to determine material stiffness, adhesion, and viscoelastic properties.

Advanced AFM methods, such as multi-frequency tapping mode and quantitative force-volume mapping, have been developed to improve the accuracy and speed of mechanical characterization. Multi-frequency AFM leverages higher harmonic oscillations of the cantilever to extract additional mechanical information beyond basic phase imaging. By analyzing multiple oscillation frequencies, researchers can differentiate between various mechanical properties such as adhesion, stiffness, and viscosity. Force-volume mapping, on the other hand, automates force curve acquisition across a defined grid, enabling spatially resolved mechanical property

mapping. To enhance resolution and acquisition speed, techniques such as Peak Force Tapping (PFT) have been introduced, which regulate tip-sample interactions through direct force control, allowing for rapid and high-resolution mechanical mapping.

AFM-based mechanical measurements rely on contact mechanics models to interpret force-distance data. The Hertz model is the most commonly used approach for extracting elastic properties, assuming that the sample behaves as a homogeneous, isotropic, and linearly elastic half-space. Although biological materials often deviate from these assumptions, modified Hertzian models, such as those developed by Sneddon for conical indenters, can provide reasonable approximations under specific conditions. More advanced models, including the Derjaguin-Muller-Toporov (DMT) and Johnson-Kendall-Roberts (JKR) theories, account for adhesive interactions, making them more suitable for studying soft biological tissues.

While AFM-based elasticity measurements have provided valuable insights into cellular mechanics, biological tissues exhibit complex viscoelastic behavior that cannot be fully captured by traditional elastic models. Living tissues display time-dependent mechanical responses due to their hierarchical structure and active remodeling processes. AFM-based microrheology techniques have been developed to assess viscoelastic properties by analyzing force relaxation and creep responses over multiple timescales. Some studies have applied poroelasticity theory to describe the fluid-driven force relaxation observed in cells, while others have suggested that nonlinear viscoelastic models may be necessary to accurately capture the mechanical behavior of biological tissues. However, implementing nonlinear viscoelastic models remains challenging due to their analytical complexity and the limited capabilities of commercial AFM systems. As a result, ongoing research aims to refine AFM-based mechanical characterization methods by integrating more advanced theoretical frameworks and improving data acquisition techniques.

In summary, AFM is a powerful tool for probing the mechanical properties of biological materials with nanometer resolution. By leveraging precise force measurements and advanced imaging techniques, AFM provides unique insights into the mechanobiology of cells and tissues. Continued advancements in AFM methodologies and theoretical models will further enhance their capability to study

complex biological systems, ultimately contributing to a deeper understanding of cellular mechanics and disease progression.

6.3 Methods

6.3.1 Lymphocyte isolation and culture

The lymphocyte isolation procedure followed in this study is a combination of the RosetteSep™ protocol [157] and the SepMate™ method [158].

Blood samples were collected and processed using the RosetteSep™ protocol for cell enrichment. To each milliliter of blood, 50 µL of RosetteSep™ Cocktail was added, followed by gentle mixing through pipetting. The sample was then incubated at room temperature (RT) for 10 minutes. After incubation, the sample was diluted with an equal volume of the recommended medium (e.g., 1 mL blood was diluted with 1 mL of the medium), ensuring gentle mixing to maintain cell integrity.

A density gradient medium was added to a SepMate™ tube to a final volume of 4.5 mL of density gradient medium. The diluted sample was carefully layered onto the tube containing the density gradient medium by pipetting along the tube wall while maintaining the tube upright to prevent the mixing of the layers. The sample was centrifuged at 1200 × g for 10 minutes with the brake on. Following centrifugation, the enriched cells at the interface were carefully collected.

The supernatant was transferred to a new standard tube, and the enriched cells were subjected to two wash steps. For the first wash, the cell suspension was topped up with the recommended medium and centrifuged at 300 × g for 10 minutes with the brake set to low (acceleration 5, brake 5). The supernatant was discarded and the process was repeated for a second wash under the same conditions. If necessary, additional wash steps were performed.

Mononuclear cells (MNCs) were isolated from whole blood using the SepMate procedure, and highly purified CD4+ T lymphocyte subsets were enriched via the RosetteSep protocol (Stemcell Technologies, Vancouver, BC, Canada), as shown in (Figure 6.1). Isolated lymphocytes (see Figure 6.1, bottom right) were cultured in 300 µL of RPMI1640 medium supplemented with penicillin 100 IU/ml, streptomycin

100 mg/mL, L-glutamine, and 10% newborn calf serum at 37 °C in a humidified atmosphere of 5% CO2. The cells were cultured either on 35 Petri dishes or glass coverslips, both coated for 5 min with poly-L-lysine hydrobromide (Sigma-Aldrich, MI, USA).

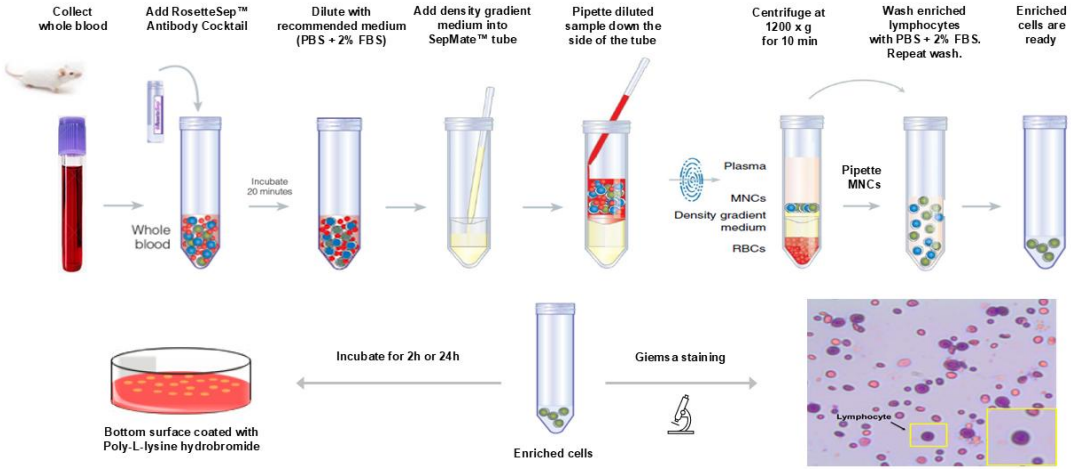

Figure 6.1: Schematic representation of lymphocyte isolation protocol using the RosetteSep™ protocol and the SepMate™ method.

6.3.2 Atomic force microscopy (AFM)

Atomic force microscopy was performed to probe the mechanical properties of live cells using a PicoPlus AFM system (Molecular Imaging-Agilent, USA) and V-shaped soft silicon nitride probes (MLCT-Bio, probe C, Bruker, USA). Isolated lymphocytes were incubated for 2 h (same day group) and 24 h (next day group) on poly-L-lysine hydrobromide coated dishes, to allow the cells to sit and adhere on the surface before AFM analysis (Figure 6.1). The reason for the two separate time points was to account for any changes in cell morphology during incubation. Petri dishes (35 mm) with the cultured cells were directly mounded on AFM sample plates. In an area of 1 × 1 μm near the center of the cells, 8 × 8 points of force curves were collected and analyzed by the freeware software AtomicJ (Jagiellonian University & AGH University of Science and Technology, Kraków, Poland) to calculate the sample's Young's modulus using the Hertz model (for cells a 0.5 Poisson ratio was used). All mechanical property measurements were recorded with a set point of 1 nN normal force. For the mechanical characterization, at least 30 live cells per condition from 3 independent experiments were studied, while attention was paid to always

performing the measurements in less than 40 min per experiment. Imaging fixed cells (20 min with 4% PFA) was performed in tapping mode with silicon probes (ACT probes, Applied Nanostructures, CA, USA). The AFM image processing was performed by using the PicoView software (Agilent, USA) and the freeware scanning probe microscopy software WSxM (Version 5.0 Develop 8, Madrid, Spain).

6.4 Results

AFM indentation was performed to probe the nanomechanical properties of circulating lymphocytes isolated from control and stented Apoe and CD1 mice. AFM measurements highlighted that lymphocytes from stented mice were stiffer as they exhibit higher Young's modulus values (Figure 6.2A). This statistically significant pattern was notable in cells that were studied either 2 h (same day) or 24 h (next day) after isolation, indicating a persistent effect regardless of any changes in cell morphology during incubation. These differences were also apparent in lymphocytes isolated from both mouse strains, with the atherosclerotic ApoE exhibiting Young's modulus values higher than those of the healthy CD1 mice. Most importantly, the comparative analysis between control and 4-week (4w) and 8-week (8w) stented CD1 mice denoted that stent implantation time affect remarkably the resulting lymphocyte stiffness (see Figure 6.2 B, C). The evaluation revealed a statistically significant higher Young's modulus value in 8w stented compared to control, which in both cases (same day and next day) increased over the 8-week implantation period (see Figure 6.2 B, C). Same-day measurements present, in general, higher Young's modulus values compared to the next-day indentations. Even so, the well-defined decrease in cell elasticity along the test cases, demonstrated after the 24 h incubation period, indicates an enduring effect. However, to account for the potential influence of surface modification on lymphocyte stiffness, a separate analysis was performed based on the stent surface treatment. The detailed results are provided in Appendix II: *In vivo*: Lymphocytes - Results. All things considered, it was shown that cellular remodelling and relevant alterations in cells' morphology, observed in the previous sections, significantly modify the cell's mechanical properties.

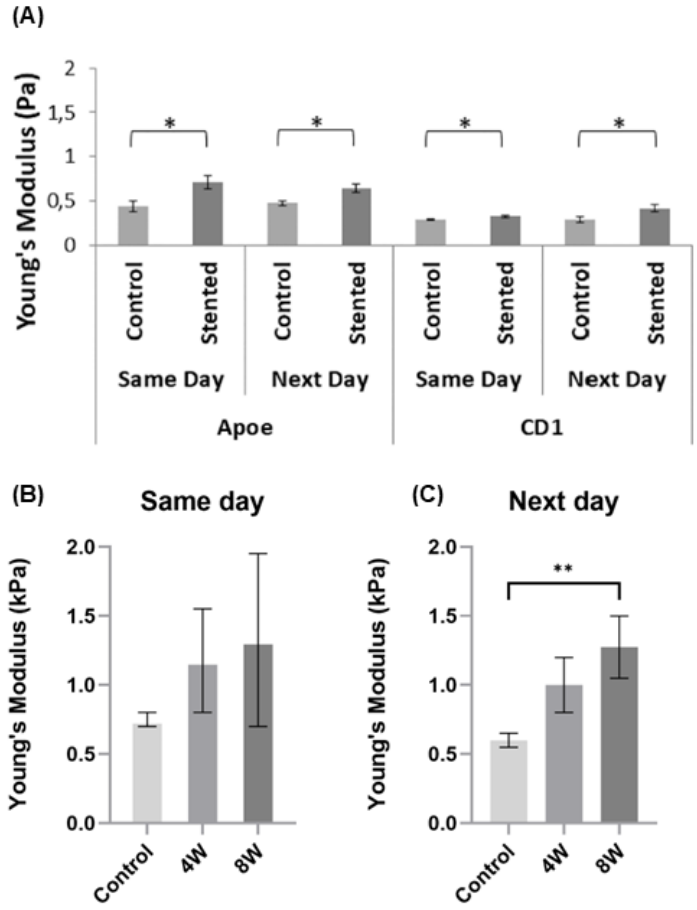

Figure 6.2: Lymphocyte elasticity expressed in Young's modulus values (kPa). (A) Control vs stented ApoE and CD1 mice (same day and 24 h after isolation). (B, C) Mid stage (4W) vs late stage (8W) stented CD1 mice, same and next day measurements, respectively (* indicates $p < 0.05$).

6.5 Discussion

AFM measurements revealed that lymphocytes from stented mice exhibit a higher Young's modulus value compared with control (sham-stented) cases. This statistically significant trend was observed across two distinct mice strains, the atherosclerotic ApoE−/− (for which changes due to lymphocyte activation are more profound) and the multipurpose CD1 strain. Notably, these differences were detected in lymphocytes analyzed both 2 hours (same day) and 24 hours (next day) after isolation. The presence of these changes in both strains suggests that they result from the implant induced effect rather than chronic inflammation associated with

atherosclerosis. The analysis also revealed a significantly higher Young's modulus value in 8W compared to control group. These results highlight that indeed the cellular remodelling that we observed through alterations in cells' morphology was accompanied by modifications in cellular nanomechanical properties.

PART IV: *In-vitro* approach

Chapter 7: Experimental evaluation of stent configuration and tube geometry on the hematological and hemorheological and hemodynamic profile of blood

7.1 Introduction

The current part evaluated in an *in-vitro* setting the possible stent-induced changes in hematological, hemorheological and hemodynamic parameters. The evaluation covered single and overlapping stent cases, in both straight and curved tube geometries, to reproduce various stented coronary artery morphologies during the cardiac cycle. Two different biomechanical flow regimes were utilized to reflect a range of physiological and more intense flow conditions.

7.2 Methodology

7.2.1 Blood sample preparation

The study protocol was approved and granted by the Cyprus National Bioethics Committee (ref: EEBK/E/2016/18). Blood samples (30 ml) were obtained from a healthy population (8 volunteers, equal number of male and female; aged 20–50 years) using a 21G needle and collected into 9 ml vacuum tubes (BD) containing 1.8 mg/ml EDTA. All tubes were then placed in a blood mixer device for 2-3 minutes, to ensure proper mixing with the anticoagulant. All blood samples were transferred in a 50 ml syringe and oxygenated by rolling carefully for approximately 1/2 minute, before extracting the air from the syringe. Testing was performed immediately after blood withdrawal.

7.2.2 Stents design and tube stenting configuration

Commercially available stents were inserted in clear perfluoroalkoxy alkane (PFA) tubing of internal diameter 2.5 mm in single and overlapping (~30%) configurations. The single stented case included a Boston Scientific stent (PROMUS Element

platinum-chromium (PtCr)) with dimensions 3 x 8 mm (nominal diameter x length) and a strut thickness of 98 μm (including the 5 μm polymer coating). For the overlapping case, two stents of similar geometry and dimensional characteristic cells were used: a Boston Scientific PROMUS Element stent (3.5 x 32 mm - strut thickness 98 μm) and an Abbott Xience PRIME cobalt-chromium (CoCr) stent (2.75 x 28 mm - strut thickness of 97 μm, including the 5 μm polymer coating).

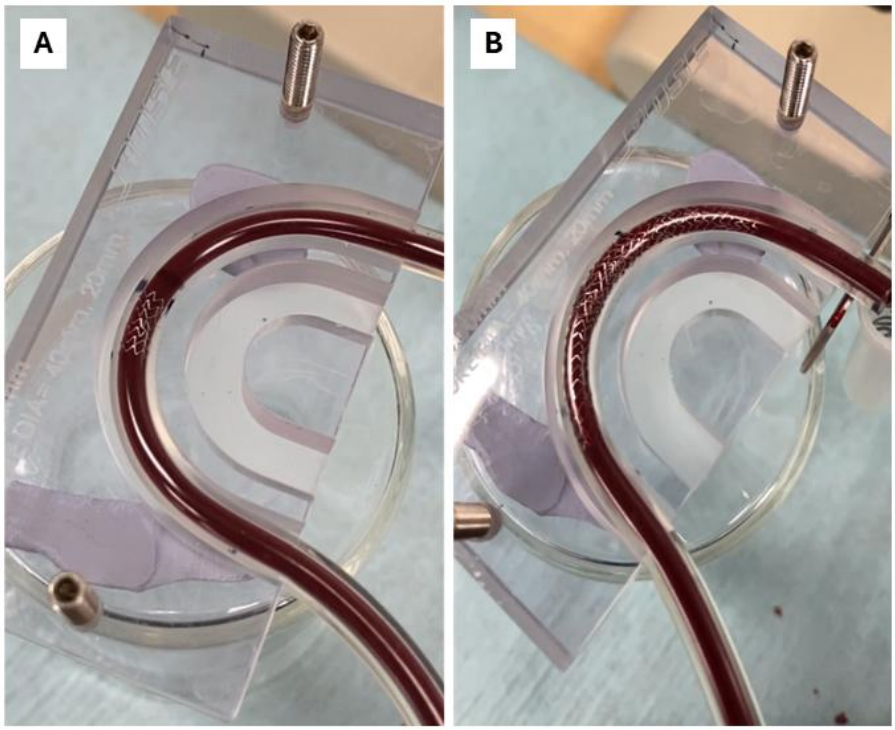

Figure 7.1: Stent images in curved geometry. (A) single stented case included a Boston Scientific stent PROMUS Element platinum-chromium (PtCr). (B) Overlapping case using two stents with similar geometry and cell dimensions: a Boston Scientific PROMUS Element stent and an Abbott Xience PRIME cobalt–chromium (CoCr) stent.

7.2.3 Experimental setup and procedure protocol

The experimental setup is shown in Figure 7.2 and Figure 7.3. As shown in the figures the 50 ml syringe, containing the blood sample, was placed on a syringe pump (KDS 200) and was linked to a pressure sensor through an empty 2.5 mm diameter PFA tubing of 6.5 mm length to ensure fully developed flow at the sensor entrance. The test tube containing the stent samples was linked to the other end of the pressure sensor, and the perfused blood samples flowed and were collected within a 2 ml Eppendorf tube (see Figure 7.2). The test tube had a length of 13.2 mm with the stent placed in the middle. The end of the tubing was in contact with the Eppendorf tube wall for smooth droplet sliding to avoid splashing.

Stents were inflated at a predetermined balloon pressure (10-12 atm as per the manufacturer's guidelines) to achieve optimal expansion with a stent-to-tube-size ratio of ~1.1. Stent apposition and stability were assessed under a stereomicroscope, and confirmed, by subjecting the stented tube to a very high flow rate (50% higher than the maximum flow rate applied during testing). Identical but empty tube setups were employed as the control cases. All three configurations (control, single, and overlapped stented) were tested in two geometries, straight and curved (radius of curvature = 20 mm). These configurations were chosen to replicate coronary artery morphologies observed in the cardiac circulatory system. The radius of curvature was chosen based on the work of Wei et al [159], and Forouzandeh et al., [160] which investigated different curvatures (radiuses of 64 mm, 40mm, and 16 mm) to represent a range of physiologically relevant arterial geometries. These values were derived from existing computational and experimental studies, ensuring that the modelled geometries encompass a broad spectrum of realistic coronary artery curvatures.

7.2.4 Experimental procedure protocol

The experimental setup, illustrating the six different cases, is shown in Figure 1. The 50 ml syringe, containing the blood sample, was placed on a syringe pump (KDS 200) and was linked in-line to a pressure sensor through an empty 2.5 mm diameter PFA tubing of 6.5 cm length. A second (test) tube, containing the stent samples, was linked to the other end of the pressure sensor, and the perfused blood specimens were collected within a 2 ml Eppendorf tube (see Figure 7.2). The end of the tubing was

in contact with the Eppendorf tube wall for smooth sliding flow to avoid splashing. The test tube had a length of 13.2 cm with the stent(s) placed in the middle. To ensure a fully developed flow in the region of the pressure sensor and stent, the entrance length (L) was calculated based on the relationship between the length-to-diameter ratio L/d and the Reynolds number (Re): L/d= 0.06*Re.

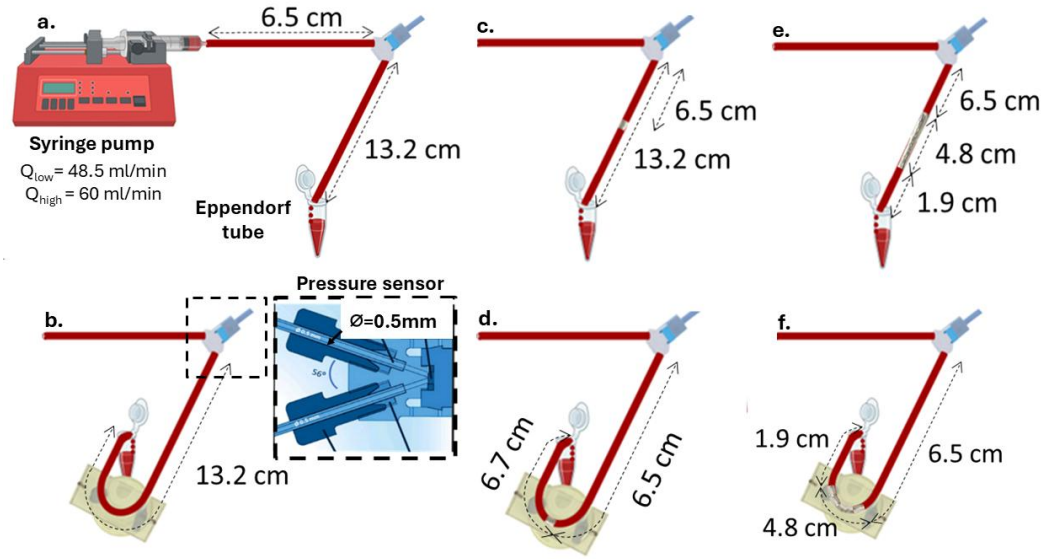

Figure 7.2: Schematic illustration of the experimental design. Experimental cases include setups for: a) straight non-stented case, b) curved non-stented case, c) single stented straight case, d) single stented curved case, e) overlapped stents in a straight tube, and f) overlapped stents in a curved tube.

The Reynolds number was estimated using the high shear viscosity of blood at 5 mPas. The lengths of both the tubes used were several times larger than the entrance lengths. The pressure monitoring setup consisted of an Elveflow OB1 MK3 pressure controller (Elveflow, Paris, France) connected with the Elvesys inline microfluidic pressure sensor (MPS3, -1 to +1 bar range, Elveflow, Paris, France). The pressure sensor was calibrated before each test to ensure accurate pressure readings, and data were continuously recorded with a 10 Hz acquisition rate for the duration of the flow.

Two different flow regimes were adopted to reflect a range of physiological flow conditions (systolic/diastolic peak and mean flow values) of the left anterior descending coronary artery [161]. The first was a baseline, low-exposure regime, where blood samples were exposed to a single passage through the stented tube, with

a flow rate of 48.5 ml/min. Figure 7.2 illustrates the experimental procedure for all geometries and stent configurations. In the low-flow rate and single-pass mode, the blood-air interface was at the exit of the tube (see Figure 7.2). The perfusion of the fluid by the syringe was set to drive 2 ml of blood in the Eppendorf tubes for collection. Representative pressure/time data can be seen in Figure Appendix III. 5.

In a second regime, higher stress and longer time exposure conditions were set, utilizing a quadruplicate blood passage (back-and-forth flow through the stented tube) with a flow rate of 60 ml/min. In this mode the starting position of the blood-air interface was placed at the end of the PFA tubes, and the first action was the infusion of blood until the pressure sensor exit. The total traveling distance in the stented tube was 13.2 cm for each infusion (pull) and perfusion (push) modes. After infusion, the first perfusion was followed, and another infusion-perfusion cycle was performed. The final stage was the collection of approximately 2 ml amount of sample in the Eppendorf tubes. The quadruple passage was then repeated. Representative pressure/time data for the quadruple mode can be seen in Figure Appendix III. 6. In both cases (single and quadruple), the sequence of blood flow experiments adhered to the following order: 1) flow in the straight, non-stented tube (control straight), 2) flow in the curved non-stented tube (control curved), 3) flow within the single stented tube (straight and curved tube) and 4) flow within the overlapped stents (straight and curved tube). After each test, the stented tube was thoroughly cleaned by infusing/withdrawing distilled water multiple (x6) times, followed by high-flow air infusion for 30 secs in order to fully dry the tube and stent. Stents were inspected again visually for cleanness and integrity before undertaking the next experiment. Additionally, during each setup change, the 50 ml syringe along with the linked tubing was carefully removed and subjected to a rolling motion to prevent red blood cell (RBC) sedimentation.

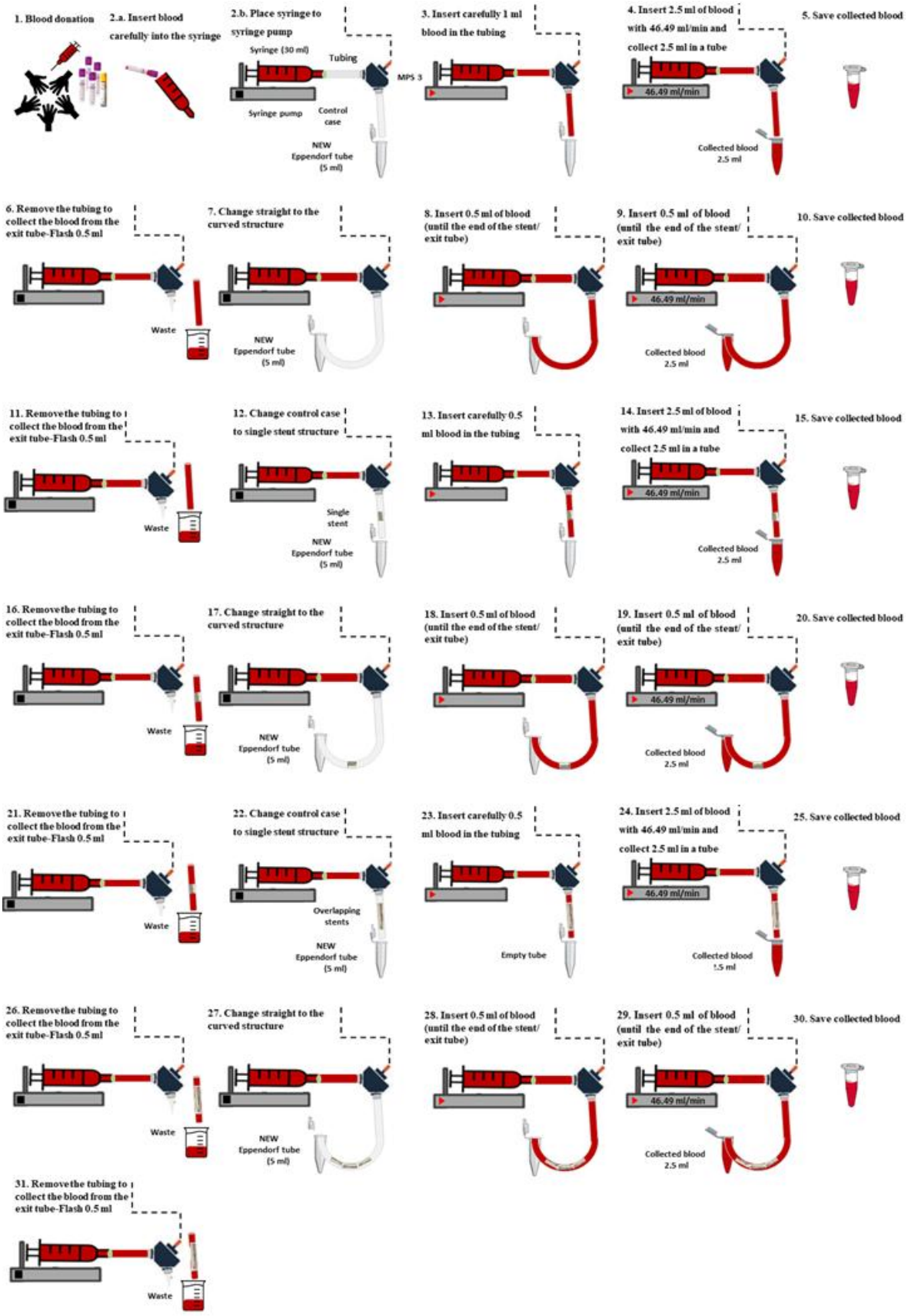

Figure 7.3: Schematic diagram of the experimental protocol of the low exposure case.

7.2.5 Hematology

Hematological testing was completed within a 3-hour timespan, in a qualified Hematology Laboratory. The Sysmex XT-2000i analyzer (Sysmex, Landskrona, Sweden) was utilized for hematological measurements which in all blood samples included white blood cell (WBC) and red blood cell (RBC) counts, hematocrit (HCT), mean corpuscular volume (MCV), and red blood cell distribution width-coefficient of variation (RDW-CV). The analytical techniques and operational principles of the Sysmex XT-2000 are comprehensively described in Section 4.1.

7.2.6 Hemodynamics

The pressure drop between the sensor and the open end of the test tubes (atmospheric conditions) was continuously recorded with a 10Hz acquisition rate for the duration of the flow. The pressure monitoring setup consisted of an Elveflow OB1 MK3 pressure controller (Elveflow, Paris, France) connected with the Elvesys inline microfluidic pressure sensor (MPS3, -1 to +1 bar range, Elveflow, Paris, France). The pressure drop results are expressed as the mean of the maximum pressure values of the two repetitions ($\overline{\Delta P}$) in the perfusing mode (pushing part in the case of the reciprocating flows) and for all volunteers ($\overline{\overline{\Delta P}}$ with n=7).

7.2.7 Hemorheology

Hemorheological evaluation commenced immediately after flow testing. The hemorheological analyses included blood viscosity, red blood cell aggregation, and deformability. All the hemorheological parameters were assessed using standard equipment and methodologies at a controlled room temperature (25±0.5 °C). The viscosity of each sample was measured using the cone-plate Brookfield DV2TLV instrument (AMETEK GB LTD T/A Brookfield, Stadium Way Harlow, Essex). All blood measurements were conducted at the same predetermined shear rates, ranging from 251.2 to 0.98 s^{-1} (from higher to lower shear rates to ensure initial dispersion of aggregates). Viscosity data were included in the analysis for transducer torque values greater than 5% of the total torque range. Normalized viscosity was calculated as $\eta^* = \frac{\eta_i}{\eta_c}$, where c represents the control configuration blood viscosity and

i represents the viscosity measured for the blood samples flowed in the different stented tube configurations. Further, the viscosity data were normalized with their high shear rate values (at 251.2 s^{-1}) for each case, in order to focus the analysis on the non-Newtonian viscosity behavior, which is affected by both RBC aggregation and deformability.

The Rheoscan A200 instrument (Rheomeditech, Seoul, Korea) was employed to assess the red blood cell aggregation of the various samples. The aggregation index (AI was utilized as a metric to evaluate the overall extent of RBC aggregation. AI is defined as the ratio of the areas above and below a time-dependent curve (a laser backscattering signal), produced by the application of a laser source on a microchip containing the blood sample [162]. Another useful aggregation index used to verify the resulting AI behavior is the aggregation half-time $T_{1/2}$ index, which indicates the time to reach half of the aggregation potential. RBC deformability measurements were determined using the Rheoscan D300 (Rheomeditech, Seoul, Korea). The instrument employs a laser diffraction technique applied on a disposable microfluidic chip [163]. In this setup, blood is perfused through the microfluidic chip at varying pressures, inducing ellipsoidal deformation of the cells. The cells' elongation index (EI) is defined from the major (A) and minor (B) lengths of the ellipsoidal axes of the deformed RBC as (A-B)/(A+B). EI is then calculated across various shear stresses (SS) ranging between 0 and 20 Pa. The maximum EI (EI_{max}) was selected as the representative deformability parameter to facilitate comparison between samples.

7.2.8 **Statistical analysis**

A two-way ANOVA test was employed to compare the hematological and hemorheological variations among the six groups of samples for each condition (normal / higher exposure) and for each stent geometry/configuration investigated in the study. In contrast, one-way ANOVA was used for pressure drop comparisons with one independent variable. The Kolmogorov-Smirnov test was employed for the normality check. All measurements were presented as mean ± standard deviation (SD), and the level of significance was initially considered at α=0.05. Moreover, the level of significance was re-evaluated according to the particular characteristics of the study, namely the relatively small sample power, to avoid missing meaningful

relationships. According to recent work by Gómez-de-Mariscal [164], the p-value, which is a size-dependent parameter, can be reset to cover issues arising when the n value is small. For the present work with n=8, the tolerance for Type I errors was increased to 10% following Bonferroni's post hoc test, and $p<0.1$ was utilized to indicate potential statistically significant information.

7.3 Results

7.3.1 Hematological evaluation

Figure 7.4 presents the hematological indices for the blood samples tested in the different stenting cases and different flow conditions. The results are presented as mean values from all tests performed (n=8) with their standard deviations placed as error bars. Along with the results, the physiological range for each parameter is indicated with the red dashed lines. Although no statistically significant differences were detected between the twelve tested conditions ($p>0.1$), some noticeable tendencies are present, which could be attributed to tube stenting and the geometric configurations used. These include the hematological changes between the baseline (low-exposure regime) and the high-exposure conditions. More specifically, an increase in RBC count and hematocrit (HCT) levels is observed (Figure 7.4a and Figure 7.4b), accompanied by a concurrent decrease in the mean corpuscular volume (MCV, in panel 2d) at high-exposure conditions compared to the baseline). These findings could also account for the higher RDW-CV (Figure 7.4c) in each case, which is found elevated in the high-exposure regime.

In general, the differences between the two exposure regimes seem to be systematic for all utilized setups, except for the control-curved configuration. Another observation made from Figure 7.4, is that the SD in RDW-CV reaches the physiological range, while those of the MCV extend below the physiological range.

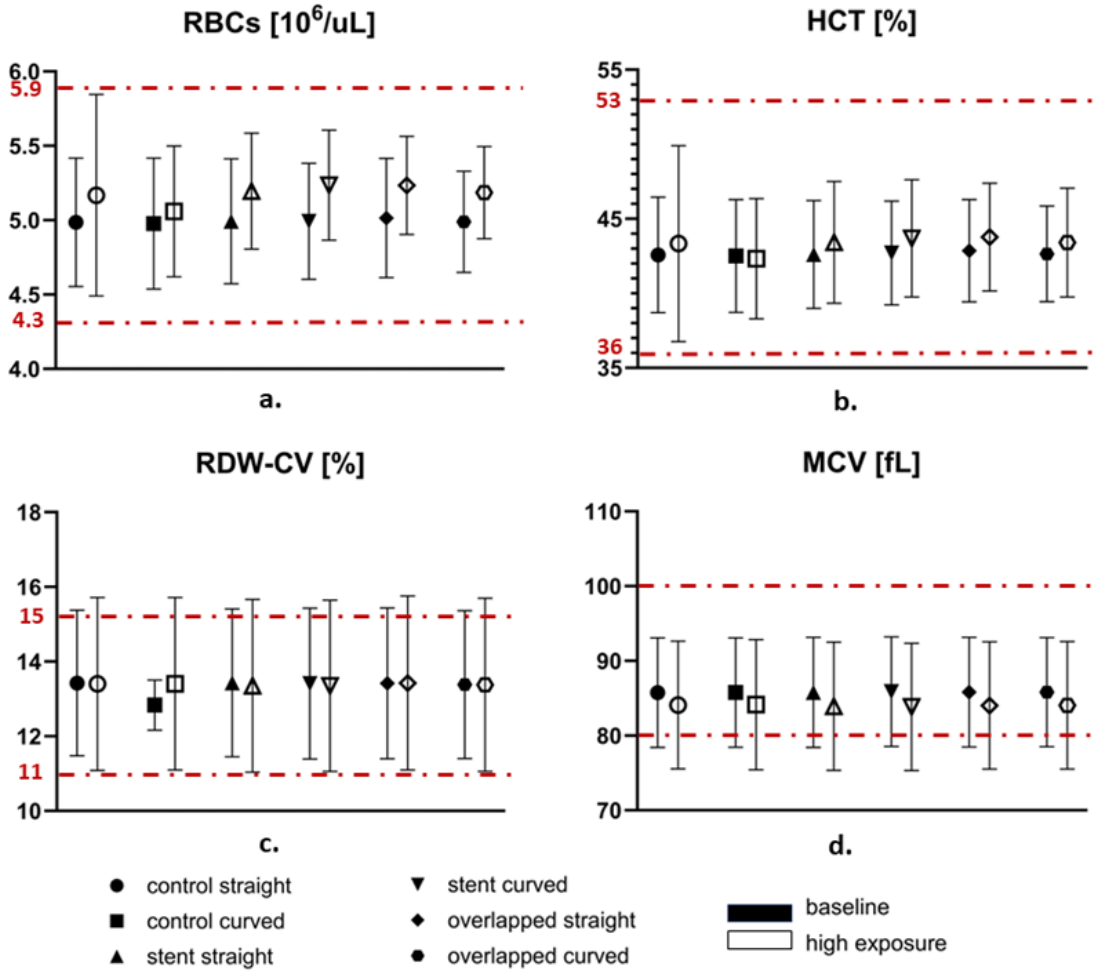

Figure 7.4: Effect of stenting on various hematological parameters for the different experimental setups and the different exposure regimes. a) RBC count, b) Hematocrit, d) RBC width distribution, and d) Mean corpuscular volume. Values are expressed as the mean ± SD. The physiological range for each parameter is indicated by the red dashed lines.

Considering the high-exposure data, it appears that there is an increasing tendency (although not significant) in the RBC count, between the control (curved) and the stented cases. In the absence of physiology factors, this increase in the RBC count could only be attributed to known flow parameters, such as alteration of the hematocrit profile in the tube, resulting in a higher concentration of cells in the bulk [165]. A supplementary gender-specific analysis was conducted and the results are presented in Appendix III.

7.3.2 Hemorheological evaluation

The hemorheological parameters RBC deformability and aggregation are expressed by the indices EI_{max} and AI respectively and are presented in Figure 7.5. The figure compares the results from the low-exposure tests (baseline tests at the lower flow rate, and lower time exposure) with those from the higher flow and time exposure in the reciprocating mode. Figure 7.5 shows a slightly higher-than-normal deformability for all samples and test modes, as normal values of EI_{max} are found in the vicinity of 0.5. This increase can be attributed to factors such as tourniquet application [166] for blood collection, as it has been found that this approach can result in approximately 8% higher than the control values measured in samples obtained without a tourniquet use [166].

Furthermore, Figure 7.5 illustrates that EI_{max} is increased in the high-exposure cases compared to the low-exposure baseline regime, for all experimental configurations. The same increasing tendency was observed in the AI. This could be explained by the elevated flow and stress conditions and time exposure that cells experience in the particular flow mode. More specifically, the increased flow rate utilized in the high-exposure regime seems to result in increased deformability and aggregation. Regarding the latter observation, it is known from the literature that the time duration the RBCs are exposed to stresses has a non-monotonic effect on the elastic properties of the cells [139]. Thus, according to shear stress and time exposure, the deformability of the RBCs can be affected positively or negatively, and the effect can be either permanent or temporary. Another study has shown that the kinetics of RBC aggregation are increased for cells with increased deformability [167], suggesting a similar effect in the present study.

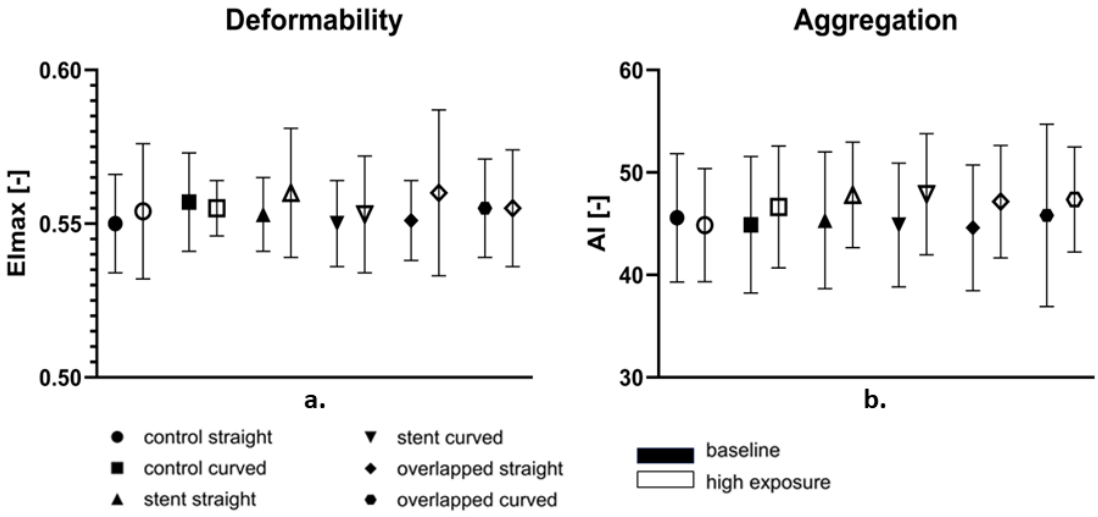

Figure 7.5: Effect of different exposure conditions (baseline vs high- exposure) in RBC deformability and aggregation.

The small alteration in RBC deformability and aggregation between the test configurations of the high-exposure condition are illustrated more clearly in Figure 7.6. A slight decrease in the deformability index is observed in Figure 7.6a between the cases of single stent from straight to curved geometries. Similarly for the cases of overlapped stents, from straight to curved geometries Figure 7.6a These small differences, however, do not show any statistical significance.

Images of the deformed pattern of RBCs, as extracted from the Rheoscan-D300 instrument, for two comparable shear stresses (2.89 and 3.11 Pa) and two configurations (control straight and overlapped curved) are shown in Figure 7.6b. In green colour are the expected physiological elliptical patterns for the specific stresses. The percent difference from the physiological pattern is also given as the difference in the ellipse area for each case.

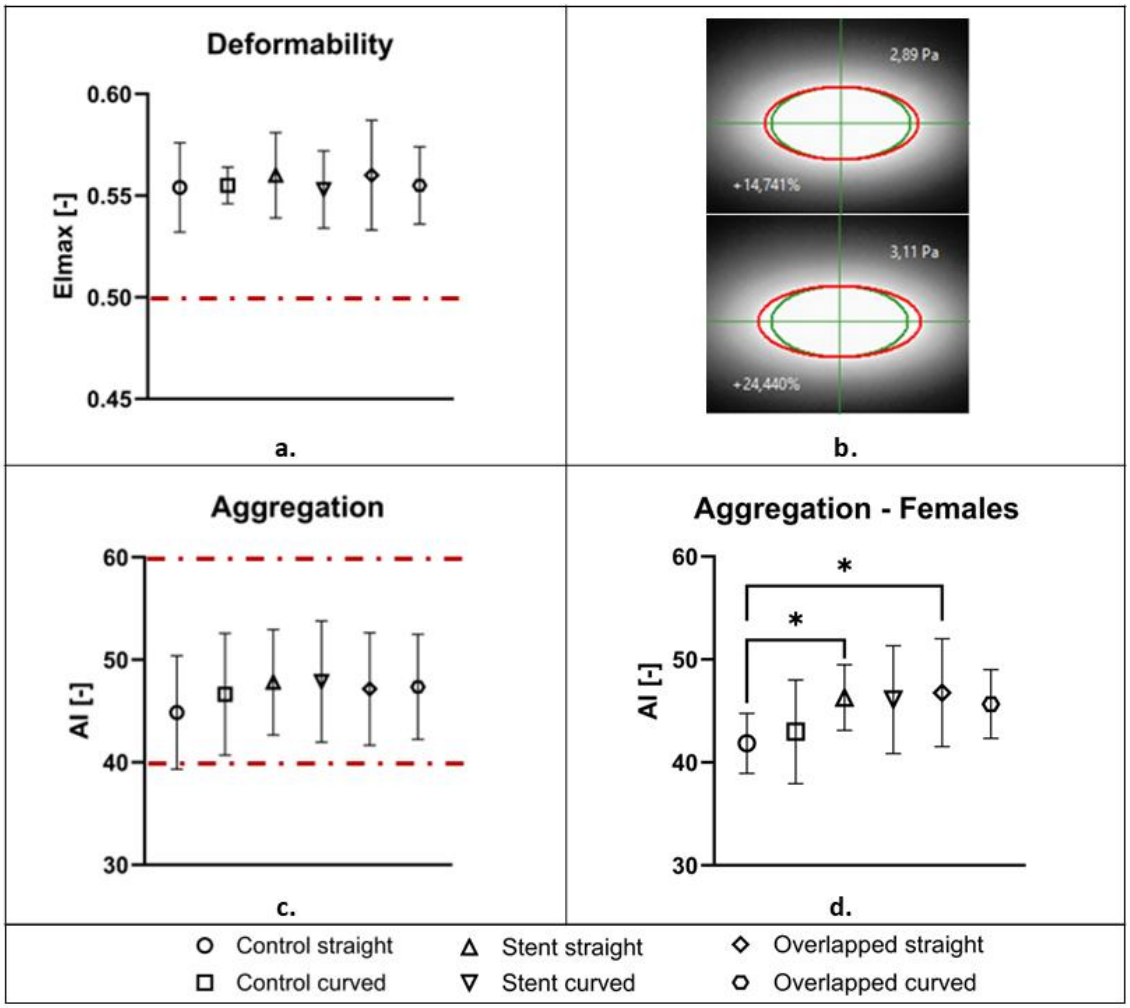

Figure 7.6: Effect of stent and geometry for the high-exposure conditions in RBC deformability (panel a) and aggregation (panel c). The physiological values for each parameter are indicated by the red dashed lines. Panel b: Images of the diffraction pattern resulted from the deformed RBCs at comparable shear stresses (2.89 and 3.11 Pa) for the Control Straight (top image) and the Overlapped Curved (bottom image). In green colour the expected physiological elliptical pattern for the specific stresses. The percent differences from the physiological pattern are given as the difference in the ellipse area for each case. Panel d): AI index for the female population of the study (* for $p<0.05$; two-way ANOVA).

The aggregation index shown in Figure 7.6c seems unchanged for the abovementioned cases (stented and overlapping), however, AI is found to be increased in all the stented samples compared to the control cases, and also when comparing the control-straight configuration, to the control-curved case. These findings imply that the stent presence within a vessel may have a small, albeit noticeable, effect on the aforementioned hemorheological properties of blood. This

tendency of RBC aggregation to be increased in the stented cases was found to be mainly due to the female participants of the study (n=4). Figure 7.6d shows that statistically significant differences are found between the Control Straight and the straight Stented and Overlapping cases ($p<0.05$). A comprehensive hemorheological gender analysis is presented in Appendix III. Furthermore, when adopting the more inclusive level of significance at 10%, another distinct difference ($p\approx0.1$) appears for the kinetics of the RBC aggregation ($T_{1/2}$ index) between the Control Straight and the Stented Straight of the overall population data (data not shown here).

The normalized (η^*) viscosity data, grouped for the single-stented and overlapping stent setups, are shown in Figure 7.7, for a shear rate range of 15.82 to 252.2 s^{-1}. The general observation from Figure 5 is that, in most cases, the non-Newtonian part for all configurations, and in both exposure, regimes is suppressed compared to the control cases. This decrease in viscosity could be attributed to geometry and configuration effects on the hemorheological parameters discussed earlier. The slight increase in deformability, seen in Figure 7.5 for the stented cases collectively, may have positively affected the viscosity of the samples. However, the increase in HCT and RBC aggregation (see Figure 7.4 and Figure 7.6), although very small, is expected to counterbalance the influence of deformability and negatively affect the viscosity of the samples.

As regards the viscosity differences between the various configurations, it can be observed from the overlapped-stent cases in Figure 7.7, that the viscosity is more profoundly closer to the control cases for the curved geometry samples, which could be linked to the increased RBC aggregation seen in those cases (see Figure 7.4). Nevertheless, no statistical significance is observed for the η^* differences between the samples.

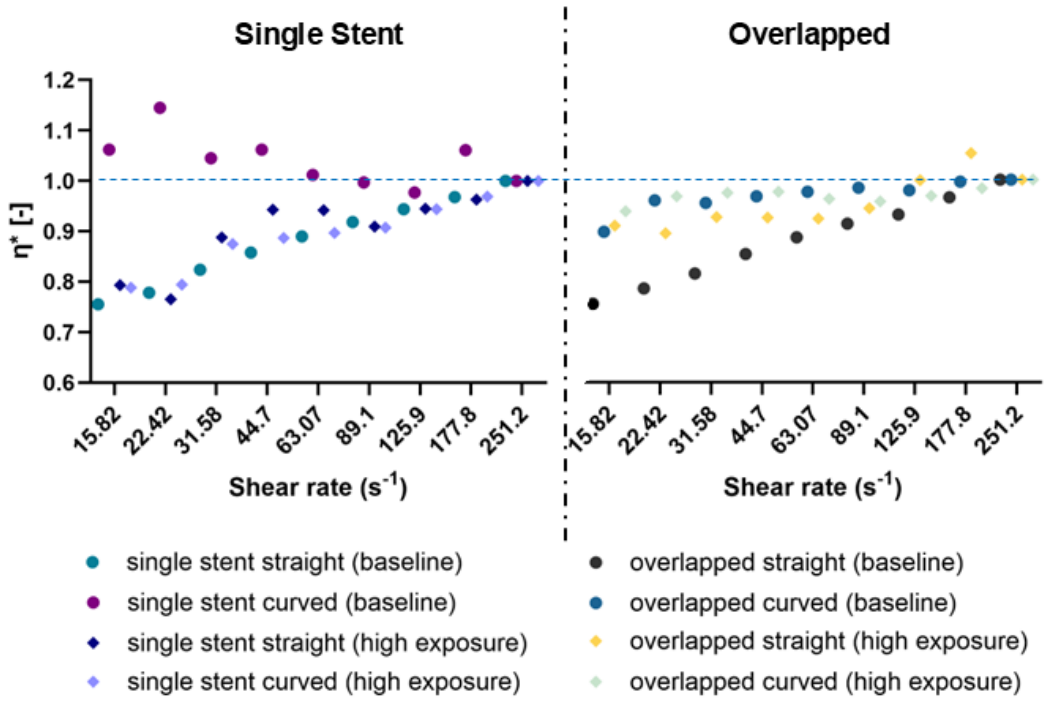

Figure 7.7: Viscosity alterations η* in single stented and overlapped cases.

7.3.3 Hemodynamics

Results for the pressure drop across the stented area are shown in Figure 7.8. $\overline{\overline{\Delta P}}$ is expressed as a mean value for the two perfusion parts in the reciprocating mode, averaged for all volunteers (n=7) in the high-exposure tests. Figure 6 designates the existing trends between the control cases and the different stenting configurations. A statistically significant difference in $\overline{\overline{\Delta P}}$ was observed between the control cases (grouped together) and the overlapped stenting configurations. That is the overlapping stent setups resulted in a greater $\overline{\overline{\Delta P}}$ value compared to the control groups, suggesting that stent overlapping and tube curvature have a measurable effect on the local pressure developed inside the tube. When comparing the curved configurations between them, an additional statistically significant difference is observed between the control and the overlapped configurations. This suggests that the curved geometry, along with further flow obstacles (overlapped stent), affects the pressure drop differently than the single stent configuration.

No statistically significant difference in $\overline{\overline{\Delta P}}$ was found between the control cases and the single stent configurations when grouped together, suggesting a small effect of the latter on the hemodynamics of the flow.

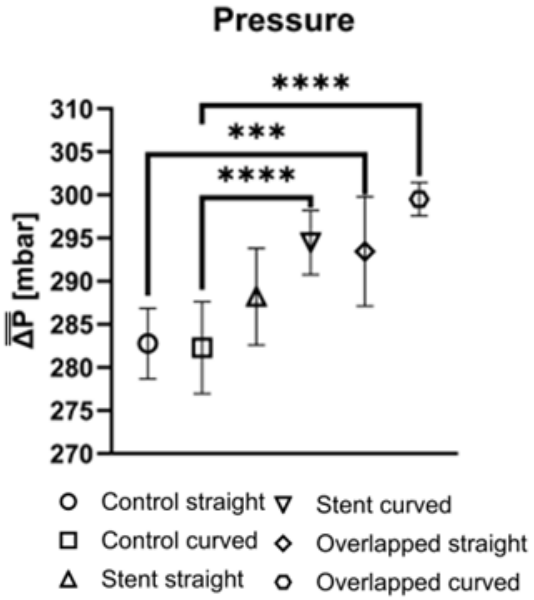

Figure 7.8: Mean Pressure $\overline{\overline{\Delta P}}$ from all volunteers for every stent configuration. (*** for p<0.001; **** for p<0.0001; one-way ANOVA).

7.4 Analysis and discussion

The results of the present study showed an observable increasing tendency between baseline and high-exposure conditions, mainly on RBC and HCT. Simultaneously, MCV seems reduced after exposure to high compared to baseline conditions. This pattern agrees with previous studies, indicating that mechanical stresses and altered flow dynamics, may impact RBC morphology and volume [168]. In human biology, rising RBC count and HCT indicate a physiological response to the altered hemodynamic environment, potentially functioning as an adaptive mechanism to maintain adequate oxygen delivery under varying shear stress conditions [169]. HCT is directly linked to the RBC mechanism of erythropoietin, which stimulates the bone marrow to produce mature RBCs, leading to an increase in hematocrit levels [170]. In the *in vitro* model of the present study, however, the increase in RBC count and

HCT could only be attributed to fluid mechanics and experimental factors. Factors such as the shear stress generated by fluid flow, the geometry of the experimental setup, and the blood handling procedures, can impact the results [171]. The MCV reduction seen in Figure 7.4 could be explained by the increased flow rate and repeated passage in the high-exposure case, resulting in RBC cells becoming more compact and deformable. Wiegmann et al., [171], observed that MCV decreases after exposure to high pressures. The combination of increased RBC and decreased MCV may have led to the observed increase in RDW-CV.

7.4.1 Hemorheological parameters

Experimental evidence has established the concept of active regulation of RBC deformability, which is primarily associated with altered interactions between membrane skeletal proteins and the integral proteins of the lipid bilayer. Consequently, it has been hypothesized that shear stress induces changes in RBC deformability; Meram et al., [172], investigated the transient improvement in RBC deformability using a Couette-type shearing system and showed that increased levels of shear stress (within 5-20 Pa) improved tissue perfusion by enhancing nitric oxide (NO) production by endothelial cells. Simmonds et al., [173], demonstrated that by applying consistent mechanical stress within the physiological range of 5–20 Pa, RBC deformability can be improved. However, it should be noted that shear stress can also impact circulating platelets, causing their activation and aggregation and thereby increasing the risk of thrombosis [172]. In the present study, the maximum shear stress is expected to appear in the region of the stent, where the flow dimensions decrease further, and the geometry becomes complex. For a steady and fully developed flow of a non-Newtonian (Power-Law) fluid in a uniform geometry, the maximum shear stress at the walls is estimated to reach approximately 4 Pa. Therefore, moderate stress levels are expected to affect the deformability of RBCs accordingly.

Blood oxygenation may be another parameter affecting the deformability of RBCs. The effects of oxygenation on erythrocyte flow velocity and shear-induced deformability were assessed through microfluidic flows, with different channel dimensions (5 μm, 20 μm) [169]. Enhanced RBC deformability was associated with

enhanced erythrocyte velocity in a microchannel flow, resulting however, in a reduced oxygen supply. In the present work, the fluid-air interface at the open front of the flow could introduce blood re-oxygenation, however, this is expected to have a small and systematic effect on all samples and cases tested. Since the deformability seems altered in the higher, compared to the low-exposure mode, it could be argued that oxygen supply could be inhibited in an in-vivo situation due to the velocity in the arterioles and capillaries being increased.

RBC membrane properties, such as cytoskeleton elasticity, and the viscosity of the cytoplasm contribute to the speed and degree of membrane relaxation, which denotes the return to the normal cell shape after deformation. It has been shown that the phosphorylation of beta spectrin by Casein kinase II, and protein kinase C-catalysed phosphorylation of protein 4.1, are correlated with elevated RBC deformability through specific receptors. The mechanical properties of blood are also affected by the fluctuations of serine phosphorylation of spectrin [174]. In the present work, any effects of stress exposure on the biochemistry of the RBC membrane could not be accounted for and perhaps will be the subject of another study.

RBC aggregation is another parameter affecting blood rheology and hemodynamics of the tube flow. In the *in vitro* setup, increased RBC aggregation has been associated with decreased flow resistance in vertical capillaries, while increased flow resistance is observed in horizontal capillaries [175]. Another similar study, on experiments conducted in vertical and horizontal glass tubes, revealed that in horizontal tubes, cell sedimentation on the lower wall increases hydrodynamic resistance, forming a nearly stagnant cell mass [176]. Plasma flows over this mass, entraining corpuscles from the upper layers. Knisely et al., [177], termed this phenomenon "sludging" and attributed it solely to pathological conditions, noting its absence in healthy individuals and animals [176]. Nader et al., [51], showed that RBC aggregates can persist in large arteries and affect flow dynamics [51]. Further, increased RBC aggregation promotes RBC axial migration, increasing the cell-free layer width, which in turn decreases the wall shear stresses, NO production, vasodilation, and blood viscosity [51,178]. The aforementioned RBC aggregation related phenomena are intense mostly in low flow rates, and therefore low shear rates. In the present study, blood was subjected to moderate to higher shear rates, and such effects are

expected not to influence the flow significantly. This is also apparent in Figure 4, showing normal aggregation levels. The statistically significant differences in the RBC aggregation observed in the present study for both levels of significance (0.05 and 0.1) in the female and the overall population, may indicate a potential influence of the stent in the phenomenon, however, all values remain in the physiological levels.

RBCs are the main determinant of blood viscosity and therefore affect the frictional forces exerted by the circulating blood on the arterial wall [179]. The results in the present study indicate that stenting may have a tracible positive influence on the viscosity of the fluids and that this may be the result of changes in the RBC properties. More specifically, the non-Newtonian behavior of blood viscosity measured for the samples of the stented configurations collectively seems to be reduced at low shear rates, when compared to the control cases (in both baseline and high-exposure cases in Figure 5). This could be attributed to the improved deformability of the RBCs, observed between the control and the stented cases (see Figures 3a and 4a). On the other hand, RBC aggregation seems to be slightly increased in the high-exposure stented cases, compared to their control samples (Figure 3b and 4b). As mentioned earlier this increase in RBC aggregation might be the result of altered deformability. As related studies have indicated, the elongation index EI_{max} and RBC shape recovery time are positively correlated with the aggregation index AI [167].

The hematocrit of the samples in the baseline and high-exposure cases, seem largely unaltered (Figure 2). In the high-exposure cases, a slight increase could be detected for the stented configurations when compared collectively to the control cases (38.90 and 38.15 respectively), however, this difference is considered to be insignificant and therefore has a negligible effect on the viscosity of the samples.

7.4.2 Local hemodynamics

Local geometrical characteristics of the stented area are expected to influence the local flow in a complex manner [68]. For instance, secondary frictional losses due to diameter reduction in the stent area and curvature of the tube are expected to influence the total pressure drop in the tube. The results of the present study illustrate

the impact of stenting, particularly of the overlapping case, and tube curvature on pressure drop inside the tube. Stenoses typically occur in curved arterial segments and bifurcations due to the strong relationship between the vascular atherogenesis process and recirculating zones induced by geometric conditions [180]. The statistically significant difference in $\overline{\overline{\Delta P}}$ between the control and overlapping stent groups suggests that both the presence of vessel curvature and the use of overlapping stents contribute to altering the hemodynamic behavior within the tube. This finding is consistent with previous studies indicating that stent overlap can create additional resistance or flow disturbances and as a result, blood flow and pressure profiles are affected [181]. Furthermore, the curvature of the vessel likely worsens these effects, as it may amplify the mechanical stress on the stent and the surrounding vessel walls, leading to higher pressure changes. In contrast, the absence of significant differences in pressure drop between the control and single stent groups suggests that single stent applications, regardless of whether the vessel is curved, do not influence the flow significantly.

7.4.3 Relationships and gender differences

Of particular importance are also the relationships between the resulting hemodynamic and hemorheological factors derived in the study, specifically the effect of stenting on blood viscosity.

The overall effect of the stent-produced pressure drop on the measured viscosity of the blood samples is seen in the correlation graph of Figure 7.9a. The pressure-drop ΔP* in this graph is the $\overline{\overline{\Delta P}}$ normalized in the same manner as the viscosity, i.e. the stented geometry $\overline{\overline{\Delta P}}$ values have been normalized with their corresponding control values, with unity implying the control cases. The viscosity values for the shear rate of 15.82 s^{-1} are used for the analysis. The graph in Figure 7.9a indicates a non-linear relationship, with two distinct features: a) an overall decreasing effect of the (stenting-produced) pressure drop, and b) an increasing tendency of the viscosity as the pressure drop increases.

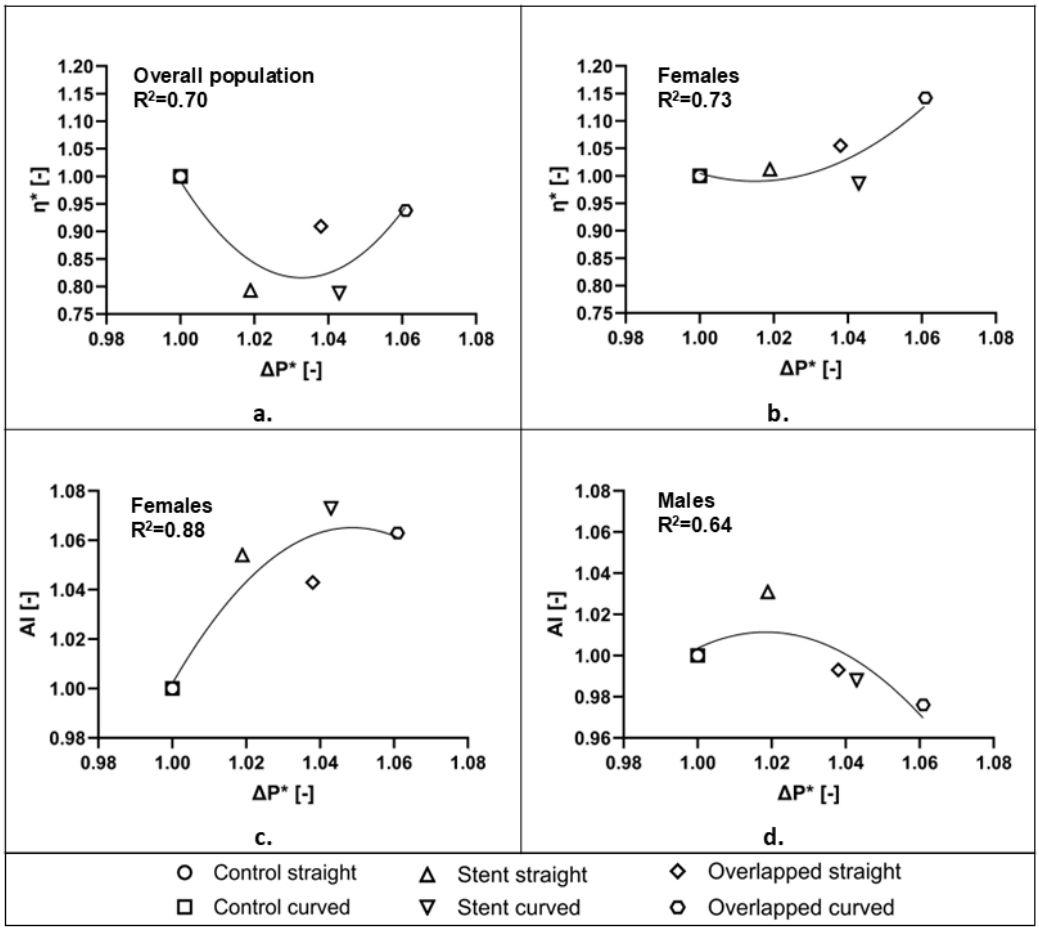

Figure 7.9: Correlation analysis. (a) Correlation between the stent-induced pressure-drop (ΔP*) and the measured viscosity (η*) of blood samples at a shear rate of 15.82 s^{-1} in the overall population. (b) Correlation between ΔP* and η* in the female group. (c) Correlation between ΔP* and aggregation index (AI) in females and (d) Correlation between ΔP* and AI in males.

The relation of η* with ΔP* shows a complex behavior, as it is not in line with the monotonic increase expected for a Newtonian or non-Newtonian flow. Figure 7.9b illustrates a clearer relation between viscosity and pressure drop for the female population. This increasing tendency can be explained by considering the RBC aggregation behavior for the female samples seen in Figure 7.6d, which is a statistically significant increasing trend against the stented configurations ($p<0.05$, $n=4$). RBC aggregation is the main determinant of the non-Newtonian nature of blood and is expected to affect negatively (i.e. increase) the effective viscosity of the fluid. This is in the absence of any slip effects (cell-free layers) that RBC aggregation

produces, due to synaeresis or other migration phenomena [182]. Increased RBC aggregation in females compared to males is expected [183], however, the present results show also a sensitivity to the local hemodynamics, namely the resulting pressure-drop increase and stress exposure.

As differences in the female RBC aggregation (Figure 7.6c) and overall pressure drop (Figure 7.8), between control and stented configurations are statistically significant, the correlation of AI* (normalized AI with corresponding control values) against ΔP* is also of particular interest. Figure 7.9c shows that the increasing trend between AI* and ΔP* in the females, follows the general AI dependency on the stent configuration, seen in Figure 7.9d. In contrast, the RBC aggregation behavior of the male population of the study (Figure 7.9d) follows a different pattern: after an initial increase of AI* with ΔP*, a slight decrease follows.

The correlation coefficients seen in Figure 7.9 indicate potential relationships between viscosity, RBC aggregation, and pressure drop. Perhaps of particular importance is the information extracted regarding the female population, as the study indicates a tendency of increasing viscosity as a result of the stent usage. This should be further investigated with more focused, and perhaps *in vivo* studies. As a general conclusion, it could be said that in clinical settings where minimizing pressure changes is crucial, single stent configurations may be preferred, particularly in cases where vessel curvature is not severe or complex.

PAPT V: General Discussion, Synopsis and Conclusions

Chapter 8: General Discussion

In the sections below a summary of the observations is provided, accompanied by a conclusive discussion on the most important topics covered in the study. This general/conclusive discussion stems from the detailed discussion of the results provided in the specific research work described in Chapters 5, 6 and 7, in which a comprehensive connection to the relevant literature work was already provided. In this part the discussion emphasizes on the most important issues unveiled in the present study. The limitations of the study are also discussed in the last section of the chapter.

8.1 *In vitro* observations

In the *in vitro* part of the study, the influence of various stent configurations on the hematological, hemorheological and hemodynamical properties of blood was investigated, for two different flow conditions. In terms of hematology, the results showed no significant influence of the setups on RBC count, HCT and MCV, with tendencies observed for exposure to more intense flow conditions. Regarding hemorheology effects, the results illustrated an influence on RBC aggregation and to a lesser degree on deformability and HCT, which consequently may have affected the non-Newtonian behavior of the blood samples of the stented cases. Hemodynamic effects produced by the presence of stents were also revealed in the pressure measurements as expected, with the overlapping stenting in the curved geometry being the most pronounced. Gender differences in RBC aggregation and viscosity effects were also revealed, which may aid in improving clinical practices. Further studies on local hemorheology and hemodynamics should contribute to a better understanding and refinement of the stenting practices.

While RBC aggregation remained within physiological limits, variations across exposure durations and configurations suggest that altered deformability indirectly modulates aggregation behavior, potentially through changes in membrane structure and intercellular adhesion.

The *in vitro* study provides detailed insights into the hemodynamic consequences of stenting. Overlapping stents and curved vessel geometries significantly increase pressure drop and flow resistance, whereas single stent implantation does not result in notable hemodynamic alterations. Overlapping stents generate complex flow fields and elevated wall shear stress, creating a biomechanical environment that could exacerbate endothelial dysfunction and promote inflammatory or thrombotic responses.

A key contribution of this work is the identification of overlapping stent configurations as a risk factor for adverse hemodynamic and hemorheological changes. These findings support clinical recommendations to prioritize single stenting whenever feasible, particularly in anatomically curved or narrow vessels, to minimize turbulence, pressure drops and inflammatory response. This insight informs interventional strategies and device selection in clinical cardiology and vascular surgery.

8.2 *In vivo* observations

The hematological analysis demonstrated a systemic response to stent implantation, characterized by increased RBC counts and HCT, particularly at later time points. This trend likely reflects erythropoiesis in response to localized hypoxia within the stented region [124]. The elevated WBCs and RDW-CV further indicated an inflammatory and oxidative stress-mediated reaction, both established contributors to adverse outcomes such as restenosis and stent thrombosis [131]. Hemorheological evaluation showed a significant reduction in RBCs deformability, especially in the late post-stenting. Reduced deformability impairs microvascular perfusion, which is correlated with elevated RDW and reflects morphological heterogeneity and mechanical stress damage.

Notably, increased RDW-CV and stiffness of lymphocytes, detected through nanomechanical profiling, highlight systemic cellular remodeling resulting from localized vascular intervention.

The *in vivo* work provided quantitative evidence of systemic cellular biomechanical remodeling post-stenting, an area that has received limited attention in literature. AFM has so far been used to determine the surface Young's modulus of VSMCs of stented New Zealand rabbits [184] and to study cross sections of coronary arteries and showed that it may serve as a useful tool for tracking atherosclerosis progression in the arterial wall tissue [185]. Observed nanomechanical alterations in lymphocyte stiffness indicate that immune cell function and vascular healing processes may be influenced by the mechanical environment introduced by the implant. Taking into account that AFM experiments can be performed the same day of cell collection and the technique is sensitive enough to assess even small alterations in cells' stiffness represented by Youngs modulus, the study's findings facilitate that AFM measurements can be used as a novel diagnostic biomarker for vascular health evaluation, peri-implant inflammation and possibly early stage of ISR.

Additionally, the study indicates that hemorheological parameters, including RDW-CV, RBC deformability and lymphocyte stiffness, may serve as effective biomarkers for post-stenting monitoring. These parameters could aid in the early detection of vascular complications and provide insights into the progression of vascular healing. The observed changes in immune cell stiffness also highlight the potential development of nanomechanical assessments as diagnostic tools. Such measurements could enable monitoring of systemic responses to vascular implants or inform immunomodulatory treatment strategies tailored to individual patients. Moreover, integrating local hemodynamic data with specific cellular behavior supports the advancement of personalized vascular modelling. Computational simulations based on patient-specific vascular geometry and flow characteristics could allow clinicians to assess the mechanical and biological implications of various stent designs prior to intervention, enabling more precise and individualized therapeutic planning.

These findings underscore the need to expand biomechanical sector. The complex interplay between mechanical stress and cellular signaling remains a critical area of investigation, especially in understanding how mechanical forces influence endothelial repair, inflammatory regulation and long-term vessel remodeling. A more comprehensive understanding of these mechanisms could pave the way for

innovative therapeutic strategies that integrate mechanical and biological principles to promote more effective and durable vascular healing.

8.3 Study limitations

Various sources of uncertainty have been identified in this study starting with the relatively small sample size, which is an inherent limitation as it did not allow extensive hematology and hemorheological analysis.

In the present work, citrate was used as an anticoagulant, although reports in the literature suggest that EDTA is the preferred anticoagulant for most automated analyzers [8]. Further, human-automated analyzers may not provide accurate results for mice, as various physiological parameters are different and can affect the efficacy of the automated analysis, such as the smaller size of RBC and variable leukocyte morphology compared to humans [128].

Hemorheological measurements were performed at room temperature (25°C with small deviations), which differs from the normal mice physiological range. Regarding the viscosity readings, the sensitivity of the viscometer did not allow us to examine results at very low shear rates with confidence, where the RBC aggregation and deformability have a greater influence. Other parameters, such as plasma viscosity, which can help in the explanation of the viscosity behavior, were not possible to obtain due to the limited amount of blood.

The presence of outliers was dealt with by applying an outlier exclusion criterion objectively and without any preconceived bias toward specific specimens or subgroups, solely based on the significant deviation of the data from the acceptable measured range of each parameter.

Chapter 9: Conclusions and future work

9.1 Concluding summary

This study emphasizes that vascular stenting induces both local mechanical alterations and extensive biological responses, which together determine the success or failure of the intervention. Integrating hematological, hemorheological and hemodynamic perspectives provides a comprehensive understanding of the post-stenting environment. The evidence presented strong support for minimizing overlapping stent configurations, as single stent deployment strategies are more effective in preserving physiological flow, reducing shear-induced damage, and preventing adverse vascular remodeling. These findings could also provide useful information for optimizing clinical practice guidelines in interventional procedures and the optimization of stent design to improve therapeutic efficacy and vascular compatibility.

By connecting mechanical design parameters with biological outcomes, this research study advances the field of cardiovascular medicine toward biomechanically informed, patient-specific and biologically compatible therapeutic strategies. Moreover, the study demonstrates that alterations in blood cell mechanics, including deformability and immune cell stiffness, serve as significant indicators of vascular stress and systemic remodelling. Although the observed gender-based trends, are preliminary, they indicate that personalized vascular therapy tailored to patient gender and biological profile may enable more targeted, personalized and effective interventions.

The findings of this study suggest several directions for future research and clinical innovation. A key implication is the potential refinement of stent deployment strategies. The evidence supports minimizing the use of overlapping stents, especially in curved vascular regions, as these configurations are associated with adverse hemodynamic effects. This insight may inform revisions to clinical guidelines and best practices in stent placement, thereby enhancing patient outcomes.

9.2 Future work

Further research is necessary to develop a comprehensive understanding of the physiological and biomechanical consequences of stent implantation. Although the present study demonstrates that stents influence hematological, hemorheological and hemodynamic parameters, several critical areas require deeper investigation to elucidate underlying mechanisms and facilitate the translation of findings into improved clinical outcomes.

Large-scale studies are warranted to further investigate these findings and signify potential clinical application. Also, in larger volume experiments, evaluating plasma viscosity, which plays a determinant role in viscosity, can help further explain viscosity behavior.

A critical direction for future research involves integrating computational fluid dynamics (CFD) models with experimental data. CFD simulations of wall shear stress and flow disturbances in various stent configurations, particularly those with overlapping or curved geometries, can help predict regions susceptible to thrombosis or endothelial injury. Such investigations may inform improvements in stent design to minimize flow disruption and enhance biomechanical compatibility.

Moreover, future work should aim to incorporate molecular and cellular analyses to investigate the biological pathways driving changes in RBC deformability, immune cell stiffness, and systemic inflammation. In this context, interleukin-6 (IL-6) should be investigated as a key pro-inflammatory cytokine. IL-6 is known to be involved in the acute-phase response and recent studies demonstrated that IL-6 promotes the development and rupture of atherosclerotic plaques and accelerating the progression of atherosclerosis. Also, IL-6 contributes to endothelial dysfunction, and post-stenting inflammatory complications. Assessing IL-6 levels in plasma, as well as IL-6 expression in vascular tissues, could provide critical insights into the link between stent-induced mechanical stress and immune activation.

Additionally, future studies should incorporate molecular and cellular analyses to investigate the biological pathways underlying changes in RBCs' deformability, immune cell stiffness and systemic inflammation. Especially, Interleukin-6 (IL-6) warrants investigation as a key pro-inflammatory cytokine. IL-6 is involved in the

acute-phase response and recent studies have demonstrated that IL-6 promotes the development and rupture of atherosclerotic plaques, thereby accelerating the progression of atherosclerosis. Furthermore, IL-6 contributes to endothelial dysfunction and post-stenting inflammatory complications. Assessing IL-6 levels in plasma and IL-6 expression in vascular tissues could provide critical insights into the relationship between stent-induced mechanical stress and immune activation.

Finally, the development of biomechanical and hemorheological biomarkers, including RDW-CV, RBC deformability indices, lymphocyte nanomechanics and circulating IL-6 levels, could facilitate the creation of novel diagnostic and monitoring tools for post-stent evaluation. These biomarkers may enable early identification of high-risk cases and support the implementation of individualized therapeutic strategies.

BIBLIOGRAPHY

1. Timmis A, Townsend N, Gale CP, Torbica A, Lettino M, Petersen SE, et al. European Society of Cardiology: CardiovascularDisease Statistics 2019.
2. Gaidai O, Cao Y, Loginov S. Global Cardiovascular Diseases Death Rate Prediction. Curr Probl Cardiol. 2023 May 1;48(5):101622.
3. Al-Kindi S, Motairek I, Khraishah H, Rajagopalan S. Cardiovascular disease burden attributable to non-optimal temperature: analysis of the 1990–2019 global burden of disease. Eur J Prev Cardiol. 2023 Apr 28;
4. Levenson JW, Skerrett PJ, Gaziano JM. Reducing the Global Burden of Cardiovascular Disease: The Role of Risk Factors. Prev Cardiol. 2002 Oct 1;5(4):188–99.
5. Wang J, Jin X, Huang Y, Ran X, Luo D, Yang D, et al. Endovascular stent-induced alterations in host artery mechanical environments and their roles in stent restenosis and late thrombosis. 2015;
6. Gori T. Vascular Wall Reactions to Coronary Stents—Clinical Implications for Stent Failure. 2021 Jan 1;11(1):1–13.
7. Grube E, Buellesfeld L. BioMatrix® Biolimus A9®-eluting coronary stent: a next-generation drug-eluting stent for coronary artery disease. http://dx.doi.org/101586/1743444036731. 2014 Nov;3(6):731–41.
8. Pan C, Han Y, Lu J. Structural Design of Vascular Stents: A Review. Micromachines 2021, Vol 12, Page 770. 2021 Jun 29;12(7):770.
9. Borhani S, Hassanajili S, Ahmadi Tafti SH, Rabbani S. Cardiovascular stents: overview, evolution, and next generation. Prog Biomater. 2018 Sep 1;7(3):175.
10. Van Der Hoeven BL, Pires NMM, Warda HM, Oemrawsingh P V., Van Vlijmen BJM, Quax PHA, et al. Drug-eluting stents: Results, promises and problems. Vol. 99, International Journal of Cardiology. Elsevier Ireland Ltd; 2005. p. 9–17.

11. Ahadi F, Azadi M, Biglari M, Bodaghi M, Khaleghian A. Evaluation of coronary stents: A review of types, materials, processing techniques, design, and problems. 2023 [cited 2023 Jul 8]; Available from: http://creativecommons.org/licenses/by/4.0/

12. Reinthaler M, Jung F, Landmesser U, Lendlein A. Trend to move from permanent metals to degradable, multifunctional polymer or metallic implants in the example of coronary stents. Vol. 13, Expert Review of Medical Devices. Taylor and Francis Ltd; 2016. p. 1001–3.

13. Van Der Hoeven BL, Pires NMM, Warda HM, Oemrawsingh P V., Van Vlijmen BJM, Quax PHA, et al. Drug-eluting stents: Results, promises and problems. Int J Cardiol. 2005 Mar 10;99(1):9–17.

14. Goodacre CJ, Bernal G, Rungcharassaeng K, Kan JYK. Clinical complications with implants and implant prostheses. Journal of Prosthetic Dentistry [Internet]. 2003 Aug 1 [cited 2023 Jul 8];90(2):121–32. Available from: http://www.thejpd.org/article/S0022391303002129/fulltext

15. Scafa Udris A, Niculescu AG, Mihai Grumezescu A, Bădilă E, Vitoria B, Ciurana Gay J, et al. materials Cardiovascular Stents: A Review of Past, Current, and Emerging Devices. 2021 [cited 2023 Jul 8]; Available from: https://doi.org/10.3390/ma14102498

16. Wang R, Lu J, Yin J, Chen H, Liu H, Xu F, et al. A TEMPOL and rapamycin loaded nanofiber-covered stent favors endothelialization and mitigates neointimal hyperplasia and local inflammation. 2022 [cited 2023 Jul 8]; Available from: http://creativecommons.org/licenses/by-nc-nd/4.0/

17. Hiebl B, Nennig E, Schiestel S, Kovacs A, Jung F, Fischer H. Biocompatibility of a novel zinc stent with a closed-cell-design. Clin Hemorheol Microcirc. 2015 Sep 5;61(2):205–11.

18. Kapnisis KK, Pitsillides CM, Prokopi MS, Lapathitis G, Karaiskos C, Eleftheriou PC, et al. In vivo monitoring of the inflammatory response

in a stented mouse aorta model. J Biomed Mater Res A. 2016;104(1):227–38.

19. Franke RP, Fuhrmann R, Krüger A, Jung F. Reaction of arterial endothelial cells to stent impression: In vitro study using a model of the human artery wall. J Cell Biotechnol. 2015 Jul 16;1(1):119–30.

20. Wang J, Jin X, Huang Y, Ran X, Luo D, Yang D, et al. Endovascular stent-induced alterations in host artery mechanical environments and their roles in stent restenosis and late thrombosis. Regen Biomater. 2018;5(3):177–87.

21. Klopfleisch R, Jung F. The pathology of the foreign body reaction against biomaterials. Vol. 105, Journal of Biomedical Materials Research - Part A. John Wiley and Sons Inc.; 2017. p. 927–40.

22. Tepe G, Schmehl J, Wendel HP, Schaffner S, Heller S, Gianotti M, et al. Reduced thrombogenicity of nitinol stents - In vitro evaluation of different surface modifications and coatings. Biomaterials. 2006 Feb;27(4):643–50.

23. Kim J, Park JK, Kim HK, Unnithan AR, Kim CS, Park CH. Optimization of electropolishing on NiTi alloy stents and its influence on corrosion behavior. J Nanosci Nanotechnol. 2017;17(4):2333–9.

24. Tré C, Tabrizian M, Yahia H, Bilodeau L, Piron DL. Effect of Modification of Oxide Layer on NiTi Stent Corrosion Resistance. Inc J Biomed Mater Res (Appl Biomater) [Internet]. 1998;43:433–40. Available from: https://onlinelibrary.wiley.com/doi/10.1002/

25. Kapnisis K, Stylianou A, Kokkinidou D, Martin A, Wang D, Anderson PG, et al. Multilevel Assessment of Stent-Induced Inflammation in the Adjacent Vascular Tissue. ACS Biomater Sci Eng. 2023 Jul 21;

26. Geng N, Su G, Wang S, Zou D, Pang W, Sun Y. High red blood cell distribution width is closely associated with in-stent restenosis in

patients with unstable angina pectoris. BMC Cardiovasc Disord. 2019;19(1):175.

27. Kastrati A, Mehilli J, Dirschinger J, Pache J, Ulm K, Schühlen H, et al. Restenosis After Coronary Placement of Various Stent Types.

28. Holmes DR, Shaughnessy CO, Caputo RP, Kereiakes DJ, Williams DO, Teirstein PS, et al. new england journal. 2003;1315–23.

29. Hayashi SI, Yamamoto A, You F, Yamashita K, Ikegame Y, Tawada M, et al. The stent-eluting drugs sirolimus and paclitaxel suppress healing of the endothelium by induction of autophagy. American Journal of Pathology. 2009;175(5):2226–34.

30. Shlofmitz E, Iantorno M, Waksman R. Restenosis of Drug-Eluting Stents: A New Classification System Based on Disease Mechanism to Guide Treatment and State-of-The-Art Review. Circ Cardiovasc Interv. 2019;12(8):1–8.

31. Baskurt OK, Meiselman HJ. Blood Rheology and Hemodynamics. Semin Thromb Hemost. 2003 Oct;29(5):435–50.

32. Foresto P et. al. Evaluation of red blood cell aggregation in diabetes by computerized image analysis - PubMed [Internet]. [cited 2022 Sep 20]. Available from: https://pubmed.ncbi.nlm.nih.gov/11188894/

33. O'Connell KE, Mikkola AM, Stepanek AM, Vernet A, Hall CD, Sun CC, et al. Practical Murine Hematopathology: A Comparative Review and Implications for Research. Comp Med [Internet]. 2015 Apr 1 [cited 2022 Feb 9];65(2):96. Available from: /pmc/articles/PMC4408895/

34. Kokkinidou D, Kaliviotis E, Shammas C, Anayiotos A, Kapnisis K. An in vivo investigation on the effects of stent implantation on hematological and hemorheological parameters. Clin Hemorheol Microcirc. 2024 Jan 1;87(1):39–53.

35. Kokkinidou D, Kapnisis K, Chrysostomou M, Shammas C, Anayiotos A, Kaliviotis E. In Vitro Evaluation of the Effect of Stenting on

Hematological, Hemorheological and Hemodynamic Parameters, in Various Stent Configurations and Flow Conditions. Cardiovasc Eng Technol [Internet]. 2025 Oct 1 [cited 2025 Nov 25];16(5):525. Available from: https://pmc.ncbi.nlm.nih.gov/articles/PMC12528324/

36. Dean L. Blood and the cells it contains. 2005;

37. Ian Peate. Muralitharan N. Fundament als of Anatomy and Physiology. Blackwell Publishing. 2015;3:103–11.

38. Chaudhry R, Miao JH, Rehman A. Physiology, Cardiovascular. StatPearls. 2022 Oct 16;

39. Tucker WD, Arora Y, Mahajan K. Anatomy, Blood Vessels. StatPearls. 2023 Aug 8;

40. Ross Ethier C, Simmons CA. Introductory Biomechanics: From Cells to Organisms.

41. U.S. Department of Health and Human Services. erythrocyte [Internet]. [cited 2024 Sep 15]. Available from: https://nci-media.cancer.gov/pdq/media/images/503952.jpg

42. Zabolotzky SM, Walker DB. Peripheral Blood Smear. Cowell and Tyler's Diagnostic Cytology and Hematology of the Dog and Cat. 1990 Jan 1;438–67.

43. Panteleev MA, Korin N, Koen |, Reesink D, David |, Bark L, et al. Wall shear rates in human and mouse arteries: Standardization of hemodynamics for in vitro blood flow assays: Communication from the ISTH SSC subcommittee on biorheology. 2020;

44. Monteiro Júnior JG de M, de Oliveira Cipriano Torres D, Filho DCS. Hematological Parameters as Prognostic Biomarkers in Patients with Cardiovascular Diseases. Curr Cardiol Rev. 2019 Feb 25;15(4):274.

45. Bogdanova A, Cabrales P, Yalcin O, Nader E, Skinner S, Romana M, et al. Blood Rheology: Key Parameters, Impact on Blood Flow, Role in Sickle Cell Disease and Effects of Exercise. 2019;

46. Brugaletta S, Sabate M. A longer look at trial evidence of bioresorbable vascular scaffolds. Heart. 2017 Jul 1;103(14):1061–2.

47. Beris AN, Horner JS, Jariwala S, Armstrong MJ, Wagner NJ. Recent advances in blood rheology: a review. Soft Matter [Internet]. 2021 Dec 8 [cited 2025 Nov 25];17(47):10591–613. Available from: https://pubs.rsc.org/en/content/articlehtml/2021/sm/d1sm01212f

48. Stephanou PS, Georgiou GG. A nonequilibrium thermodynamics perspective of thixotropy. J Chem Phys [Internet]. 2018 Dec 28 [cited 2025 Nov 25];149(24). Available from: https://pubmed.ncbi.nlm.nih.gov/30599698/

49. Pratumwal Y, Limtrakarn W, Muengtaweepongsa S, Phakdeesan P, Duangburong S, Eiamaram P, et al. Whole blood viscosity modeling using power law, Casson, and Carreau Yasuda models integrated with image scanning U-tube viscometer technique. Songklanakarin Journal of Science and Technology. 2017 Sep 1;39(5):625–31.

50. Gijsen FJH, Allanic E, Van De Vosse FN, Janssen JD. The influence of the non-Newtonian properties of blood on the flow in large arteries: unsteady flow in a 90° curved tube. J Biomech. 1999 Jul 1;32(7):705–13.

51. Nader E, Skinner S, Romana M, Fort R, Lemonne N, Guillot N, et al. Blood Rheology: Key Parameters, Impact on Blood Flow, Role in Sickle Cell Disease and Effects of Exercise. Front Physiol. 2019;10(OCT).

52. Rouleaux – Sonographic Tendencies [Internet]. [cited 2025 Feb 2]. Available from: https://sonographictendencies.com/2016/11/05/rouleaux/

53. Baskurt OK, Meiselman HJ. Erythrocyte aggregation: Basic aspects and clinical importance. Clin Hemorheol Microcirc. 2013;53(1–2):23–37.

54. Bogdanova A, Cabrales P, Yalcin O, Nader E, Skinner S, Romana M, et al. Blood Rheology: Key Parameters, Impact on Blood Flow, Role in Sickle Cell Disease and Effects of Exercise. 2019;

55. Hamlin SK, Benedik PS. Basic Concepts of Hemorheology in Microvascular Hemodynamics. Crit Care Nurs Clin North Am. 2014;26(3):337–44.

56. Chien S, Usami S, Dellenback RJ, Gregersen MI. Shear-dependent deformation of erythrocytes in rheology of human blood. Am J Physiol. 1970;219(1):136–42.

57. Cardiovascular diseases (CVDs) [Internet]. [cited 2024 Sep 3]. Available from: https://www.who.int/news-room/fact-sheets/detail/cardiovascular-diseases-(cvds)

58. Shahjehan RD, Bhutta BS. Coronary Artery Disease. Medical Nursing. 2023 Aug 17;110–4.

59. Atherosclerosis - Treatment | NHLBI, NIH [Internet]. [cited 2024 Sep 22]. Available from: https://www.nhlbi.nih.gov/health/atherosclerosis/treatment

60. Cardiology ES of. Coronary stents per million people, 2016 [Internet]. [cited 2024 Nov 2]. Available from: https://ourworldindata.org/grapher/coronary-stents-per-million-people

61. Maisel WH, Laskey WK. Drug-eluting stents. Circulation. 2007;115(17):426–7.

62. Lovely Chhabra; Muhammad A. Zain; Waqas J. Siddiqui. Coronary Stents - StatPearls - NCBI Bookshelf [Internet]. 2024 [cited 2024 Sep 21]. Available from: https://www.ncbi.nlm.nih.gov/books/NBK507804/?report=reader#_NBK507804_pubdet_

63. Baura GD. Catheters, Bare Metal Stents, and Synthetic Grafts. Medical Device Technologies. 2012 Jan 1;165–92.

64. Palmaz JC, Bailey S, Marton D, Sprague E. Influence of stent design and material composition on procedure outcome. J Vasc Surg. 2002;36(5):1031–9.

65. Bønaa KH, Mannsverk J, Wiseth R, Aaberge L, Myreng Y, Nygård O, et al. Drug-Eluting or Bare-Metal Stents for Coronary Artery Disease. New England Journal of Medicine. 2016 Sep 29;375(13):1242–52.

66. Andreou I, Stone PH, Ikonomidis I, Alexopoulos D, Sabaté M. Recurrent atherosclerosis complications as a mechanism for stent failure. Hellenic Journal of Cardiology. 2020 Jan 1;61(1):9–14.

67. Sabaté M, Brugaletta S, Cequier A, Iñiguez A, Serra A, Jiménez-Quevedo P, et al. Clinical outcomes in patients with ST-segment elevation myocardial infarction treated with everolimus-eluting stents versus bare-metal stents (EXAMINATION): 5-year results of a randomised trial. The Lancet. 2016 Jan 23;387(10016):357–66.

68. Kapnisis K, Seidner H, Prokopi M, Pasias D, Pitsillides C, Anayiotos A, et al. The effects of stenting on hemorheological parameters: An in vitro investigation under various blood flow conditions. Clin Hemorheol Microcirc. 2019;72(4):375–93.

69. Noad RL, Hanratty CG, Walsh SJ. Clinical Impact of Stent Design. Interventional Cardiology Review [Internet]. 2014 [cited 2022 May 23];9(2):89. Available from: /pmc/articles/PMC5808536/

70. Mcclean DR, Eigler NL. Stent Design: Implications for Restenosis. Vol. 3, Reviews in Cardiovascular Medicine. 2002.

71. Sakamoto A, Jinnouchi H, Torii S, Virmani R, Finn A V. Understanding the impact of stent and scaffold material and strut design on coronary artery thrombosis from the basic and clinical points of view. Bioengineering. 2018;5(3):1–19.

72. Kolandaivelu K, Swaminathan R, Gibson WJ, Kolachalama VB, Nguyen-Ehrenreich KL, Giddings VL, et al. Stent thrombogenicity early in high-risk interventional settings is driven by stent design and

deployment and protected by polymer-drug coatings. Circulation. 2011 Apr 5;123(13):1400–9.

73. Condello F, Spaccarotella C, Sorrentino S, Indolfi C, Stefanini GG, Polimeni A. Stent Thrombosis and Restenosis with Contemporary Drug-Eluting Stents: Predictors and Current Evidence. J Clin Med. 2023 Feb 1;12(3):1238.

74. Zhang X, Yang L, Ju H, Zhang F, Wu J, He B, et al. Prevalence and prognosis of coronary stent gap detected by multi-detector CT: a follow-up study. Eur Radiol. 2012 Sep;22(9):1896–903.

75. Ng CKJ, Paradies V, Vlachojannis GJ, Toh HW, Leo HL, Wong EHP, et al. Provisional Stenting for the Treatment of Bifurcation Lesions: In Vitro Insights. J Cardiovasc Transl Res. 2021;14(4):595–7.

76. Lu S, Ng J, Ang H, Paradies V, Wong PE, Al-Lamee R, et al. Is There Light at the End of the Thin-Strut Tunnel?: In Vitro Insights on Strut Thickness Impact on Thrombogenicity in Bioresorbable Stents or Scaffolds. JACC Cardiovasc Interv. 2018;11(7):714–6.

77. Shlofmitz E, Iantorno M, Waksman R. Restenosis of Drug-Eluting Stents: A New Classification System Based on Disease Mechanism to Guide Treatment and State-of-The-Art Review. Circ Cardiovasc Interv. 2019;12(8):1–8.

78. Palmerini T, Barozzi C, Tomasi L, Riva D Della, Marengo M, Cicoria G, et al. In vitro thrombogenicity of drug-eluting and bare metal stents. Thromb Res. 2020;185(November 2019):43–8.

79. Koppara T, Cheng Q, Yahagi K, Mori H, Sanchez OD, Feygin J, et al. Thrombogenicity and early vascular healing response in metallic biodegradable polymer-based and fully bioabsorbable drug-eluting stents. Circ Cardiovasc Interv. 2015;8(6):1–9.

80. Zhang Z, An L, Du D, Lai X, Wang F, Li Y. The change in platelet count in patients with acute coronary syndrome 6 months after coronary stent implantation. Blood Coagulation & Fibrinolysis

[Internet]. 2015 Sep 1 [cited 2022 May 19];26(6):661. Available from: /pmc/articles/PMC4527681/

81. Qian H, Luo Z, Xiao C, Chen J, Li D, Xu H, et al. Red cell distribution width in coronary heart disease: Prediction of restenosis and its relationship with inflammatory markers and lipids. Postgrad Med J. 2018 Sep 1;94(1115):489–94.

82. Geng N, Su G, Wang S, Zou D, Pang W, Sun Y. High red blood cell distribution width is closely associated with in-stent restenosis in patients with unstable angina pectoris. BMC Cardiovasc Disord. 2019 Jul 24;19(1):175.

83. Kassaian S, Salarifar M, Raissi Dehkordi M, Alidoosti M, Nematipour E, PoorhosseiniI H, et al. Cardiovascular topics outcomes of stenting with overlapping drug-eluting stents versus overlapping drug-eluting and bare-metal stents for the treatment of diffuse coronary lesions [Internet]. Vol. 21, Cardiovascular Journal of Africa. Available from: www.cvja.co.za

84. Lominadze D, Dean WL. Involvement of fibrinogen specific binding in erythrocyte aggregation. FEBS Lett [Internet]. 2002 Apr 24 [cited 2025 Mar 23];517(1–3):41. Available from: https://pmc.ncbi.nlm.nih.gov/articles/PMC2819362/

85. Szapary L, Bagoly E, Kover F, Feher G, Pozsgai E, Koltai K, et al. The effect of carotid stenting on rheological parameters, free radical production and platelet aggregation. Clin Hemorheol Microcirc. 2009;43(3):209–17.

86. Gergely F, Edit B, Ferenc K, Katali K, Katalin H, Éva P, et al. [The effect of carotid stenting on rheological parameters, free radical production and platelet aggregation]. Orv Hetil [Internet]. 2007 Dec 16 [cited 2022 May 10];148(50):2365–70. Available from: https://pubmed.ncbi.nlm.nih.gov/18055360/

87. Benard N, Coisne D, Donal E, Perrault R. Experimental study of laminar blood flow through an artery treated by a stent implantation:

Characterisation of intra-stent wall shear stress. J Biomech. 2003 Jul 1;36(7):991–8.

88. Zhu T, Zhou M, Gao W, Fang D, Liu Z, Wu G, et al. Coronary Stents Decorated by Heparin/NONOate Nanoparticles for Anticoagulant and Endothelialized Effects. Langmuir. 2020;36(11):2901–10.

89. Toth C, Ii ZK, Toth E, Hargitai Z, Nemeth N, Md V. Early postoperative changes in hematological, erythrocyte aggregation and blood coagulation parameters after unilateral implantation of polytetrafluoroethylene vascular graft in the femoral artery of beagle dogs 1. Took part in laboratory measurements, evaluating results. Acta Cir Bras. 2014;29(5):2014–321.

90. Osenberg CW, Sarnelle O, Cooper SD. Effect size in ecological experiments: the application of biological models in meta-analysis. Am Nat [Internet]. 1997 [cited 2025 Nov 25];150(6):798–812. Available from: https://pubmed.ncbi.nlm.nih.gov/18811337/

91. Reinhart WH, Piety NZ, Goede JS, Shevkoplyas SS. Effect of osmolality on erythrocyte rheology and perfusion of an artificial microvascular network. Microvasc Res [Internet]. 2015 Mar 1 [cited 2025 Nov 29];98:102. Available from: https://pmc.ncbi.nlm.nih.gov/articles/PMC4361376/

92. Alves MM, Rocha C, Gonçalves MP. Study of the rheological behaviour of human blood using a controlled stress rheometer. Clin Hemorheol Microcirc. 2013;53(4):369–86.

93. Baskurt OK, Boynard M, Cokelet GC, Connes P, Cooke BM, Forconi S, et al. New guidelines for hemorheological laboratory techniques *. Clin Hemorheol Microcirc [Internet]. 2009 [cited 2025 Nov 28];42:75–97. Available from: http://www.akdeniz.edu.tr/~baskurt.

94. Stuart J. Guidelines for measurement of blood viscosity and erythrocyte deformability. Clin Hemorheol. 1986;6(5):439–53.

95. Hill VL, Simpson VZ, Higgins JM, Hu Z, Stevens RA, Metcalf JA, et al. Evaluation of the performance of the sysmex XT-2000i hematology analyzer with whole blood specimens stored at room temperature. Lab Med. 2009;40(12):709–18.

96. McKinnon KM. Flow Cytometry: An Overview. Curr Protoc Immunol. 2018 Feb 1;120:5.1.1.

97. Imazu M. General Description of the Automated Hematology Analyzer , XT-2000 i. Sysmex Journal International. 2002;12(1):13–7.

98. Kala PS, Zubair M. Flow Cytometry Blood Cell Identification. StatPearls. 2024 Sep 11;

99. Adan A, Alizada G, Kiraz Y, Baran Y, Nalbant A. Flow cytometry: basic principles and applications. Crit Rev Biotechnol. 2017 Feb 17;37(2):163–76.

100. Kapnisis K, Seidner H, Prokopi M, Pasias D, Pitsillides C, Anayiotos A, et al. The effects of stenting on hemorheological parameters: An in vitro investigation under various blood flow conditions. Clin Hemorheol Microcirc. 2019;72(4):375–93.

101. Horobin JT, Sabapathy S, Simmonds MJ. Red blood cell tolerance to shear stress above and below the subhemolytic threshold. Biomech Model Mechanobiol. 2020 Jun 1;19(3):851–60.

102. Baskurt OK, Uyuklu M, Ulker P, Cengiz M, Nemeth N, Alexy T, et al. Comparison of three instruments for measuring red blood cell aggregation. Clin Hemorheol Microcirc. 2009;43(4):283–98.

103. Semenov A, Lugovtsov A, Ermolinskiy P, Lee K, Priezzhev A. Problems of Red Blood Cell Aggregation and Deformation Assessed by Laser Tweezers, Diffuse Light Scattering and Laser Diffractometry. Photonics. 2022 Apr 1;9(4):238.

104. Hemorheology Test Assessment of Deformability, Aggregation, and Critical Shear Stress of RBCs Innovative technology of diabetic complication screening assay.

105. Kim J, Lee H, Shin S. Advances in the measurement of red blood cell deformability: A brief review. J Cell Biotechnol. 2015;1:63–79.

106. Koutsiaris AG. A velocity profile equation for blood flow in small arterioles and venules of small mammals in vivo and an evaluation based on literature data. Clin Hemorheol Microcirc [Internet]. 2009 [cited 2026 Jan 17];43(4):321–34. Available from: /doi/pdf/10.3233/CH-2009-1243?download=true

107. Koutsiaris AG, Tachmitzi S V., Batis N, Kotoula MG, Karabatsas CH, Tsironi E, et al. Volume flow and wall shear stress quantification in the human conjunctival capillaries and post-capillary venules in vivo. Biorheology [Internet]. 2007 [cited 2026 Jan 17];44(5–6):375–86. Available from: /doi/pdf/10.1177/0006355X2007044005006008?download=true

108. Microfluidic Pressure sensor - Elveflow [Internet]. [cited 2025 Mar 29]. Available from: https://www.elveflow.com/microfluidic-products/microfluidics-flow-measurement-sensors/pressure-sensor/

109. Demosthenous E. Development of a microfludics system for the examination of the effects of cardiovascular stenting on blood fluid mechanics and physiology: System validation study. 2021.

110. Baars T, Kahlert P, Baars A, Preibsch H, Rassaf T, Heusch G, et al. Influence of stent implantation on erythrocyte aggregation in human native coronary arteries and saphenous vein grafts. Microcirculation [Internet]. 2016 Nov 1 [cited 2023 Mar 5];23(8):637–45. Available from: https://onlinelibrary.wiley.com/doi/full/10.1111/micc.12326

111. Kouvelos GN, Patelis N, Antoniou GA, Lazaris A, Matsagkas MI. Meta-analysis of the effect of stent design on 30-day outcome after carotid artery stenting. Journal of Endovascular Therapy. 2015 Oct 1;22(5):789–97.

112. Diez-Silva M, Dao M, Han J, Lim CT, Suresh S. 382 MRS BULLETIN • VOLUME 35 • MAY 2010 • www.mrs.org/bulletin

Shape and Biomechanical Characteristics of Human Red Blood Cells in Health and Disease.

113. Stroobach M, Haya L, Fenech M. Effects of red blood cell aggregation on microparticle wall adhesion in circular microchannels. Med Eng Phys. 2019 Jul 1;69:100–8.

114. Szapary L, Bagoly E, Kover F, Feher G, Pozsgai E, Koltai K, et al. The effect of carotid stenting on rheological parameters, free radical production and platelet aggregation. Clin Hemorheol Microcirc. 2009;43(3):209–17.

115. Gamage PT, Dong P, Lee J, Gharaibeh Y, Zimin VN, Dallan LAP, et al. Hemodynamic alternations following stent deployment and post-dilation in a heavily calcified coronary artery: In silico and ex-vivo approaches. Comput Biol Med. 2021 Dec 1;139.

116. Saylor DM, Buehler PW, Brown RP, Malinauskas RA. Predicting plasma free hemoglobin levels in patients due to medical device-related hemolysis. Vol. 65, ASAIO Journal. Lippincott Williams and Wilkins; 2019. p. 207–18.

117. Braune S, Latour RA, Reinthaler M, Landmesser U, Lendlein A, Jung F. In Vitro Thrombogenicity Testing of Biomaterials. Vol. 8, Advanced Healthcare Materials. Wiley-VCH Verlag; 2019.

118. Simsekyilmaz S, Schreiber F, Weinandy S, Gremse F, Sönmez TT, Liehn EA. A Murine Model of Stent Implantation in the Carotid Artery for the Study of Restenosis. J Vis Exp. 2013;(75):50233.

119. Öner A, Moerke C, Wolff A, Kischkel S, Schmidt W, Grabow N, et al. A preclinical animal model for evaluating the sealing capacity of covered stent grafts in acute vessel perforation. Eur J Med Res [Internet]. 2020 Jul 29 [cited 2022 May 23];25(1):1–7. Available from: https://eurjmedres.biomedcentral.com/articles/10.1186/s40001-020-00429-y

120. Alexy T, Detterich J, Connes P, Toth K, Nader E, Kenyeres P, et al. Physical Properties of Blood and their Relationship to Clinical Conditions. Vol. 13, Frontiers in Physiology. Frontiers Media S.A.; 2022.

121. Simmonds MJ, Meiselman HJ. Prediction of the level and duration of shear stress exposure that induces subhemolytic damage to erythrocytes. Biorheology. 2016 Jan 1;53(5–6):237–49.

122. Simmonds MJ, Atac N, Baskurt OK, Meiselman HJ, Yalcin O. Erythrocyte deformability responses to intermittent and continuous subhemolytic shear stress. Biorheology. 2014 Jan 1;51(2–3):171–85.

123. Ananthaseshan S, Bojakowski K, Sacharczuk M, Poznanski P, Skiba DS, Prahl Wittberg L, et al. Red blood cell distribution width is associated with increased interactions of blood cells with vascular wall. Sci Rep. 2022 Dec 1;12(1).

124. Tarbell J, Mahmoud M, Corti A, Cardoso L, Caro C. The role of oxygen transport in atherosclerosis and vascular disease. J R Soc Interface [Internet]. 2020 Apr 1 [cited 2022 Sep 22];17(165). Available from: https://royalsocietypublishing.org/doi/10.1098/rsif.2019.0732

125. Baars T, Kahlert P, Baars A, Preibsch H, Rassaf T, Heusch G, et al. Influence of stent implantation on erythrocyte aggregation in human native coronary arteries and saphenous vein grafts. Microcirculation. 2016 Nov 1;23(8):637–45.

126. Cornelissen A, Guo L, Fernandez R, Kelly MC, Janifer C, Kuntz S, et al. Endothelial Recovery in Bare Metal Stents and Drug-Eluting Stents on a Single-Cell Level. Arterioscler Thromb Vasc Biol. 2021 Aug 1;41(8):2277–92.

127. Ochijewicz D, Tomaniak M, Opolski G, Kochman J. Inflammation as a determinant of healing response after coronary stent implantation. Vol. 37, International Journal of Cardiovascular Imaging. Springer Science and Business Media B.V.; 2021. p. 791–801.

128. O'Connell KE, Mikkola AM, Stepanek AM, Vernet A, Hall CD, Sun CC, et al. Practical Murine Hematopathology: A Comparative Review and Implications for Research. Comp Med [Internet]. 2015 Apr 1 [cited 2022 May 16];65(2):96. Available from: /pmc/articles/PMC4408895/

129. Nemzek JA, Bolgos GL, Williams BA, Remick DG. Differences in normal values for murine white blood cell counts and other hematological parameters based on sampling site. Inflammation Research. 2001;50(10):523–7.

130. Bolliger AP, Everds N. Haematology of the Mouse. The Laboratory Mouse. 2012;331–47.

131. Rajagopal V, Gurm HS, Bhatt DL, Lincoff AM, Tcheng JE, Kereiakes DJ, et al. Relation of an elevated white blood cell count after percutaneous coronary intervention to long-term mortality. Am J Cardiol [Internet]. 2004 Jul 15 [cited 2022 Mar 28];94(2):190–2. Available from: https://pubmed.ncbi.nlm.nih.gov/15246898/

132. Bao D, Luo G, Kan F, Wang X, Luo J, Jiang C. Prognostic value of red cell distribution width in patients undergoing percutaneous coronary intervention: a meta-analysis. [cited 2022 Mar 14]; Available from: http://bmjopen.bmj.com/

133. Osadnik T, Strzelczyk J, Hawranek M, Lekston A, Wasilewski J, Kurek A, et al. Red cell distribution width is associated with long-term prognosis in patients with stable coronary artery disease. BMC Cardiovasc Disord [Internet]. 2013 Dec 10 [cited 2022 Mar 14];13(1):1–8. Available from: https://bmccardiovascdisord.biomedcentral.com/articles/10.1186/1471-2261-13-113

134. Grygorczyk R, Orlov SN. Effects of Hypoxia on Erythrocyte Membrane Properties—Implications for Intravascular Hemolysis and Purinergic Control of Blood Flow. Front Physiol. 2017 Dec 22;8(DEC):1110.

135. Li N, Zhou H, Tang Q. Red Blood Cell Distribution Width: A Novel Predictive Indicator for Cardiovascular and Cerebrovascular Diseases. Dis Markers [Internet]. 2017 [cited 2022 May 23];2017. Available from: /pmc/articles/PMC5606102/

136. Xanthopoulos A, Giamouzis G, Dimos A, Skoularigki E, Starling RC, Skoularigis J, et al. Red Blood Cell Distribution Width in Heart Failure: Pathophysiology, Prognostic Role, Controversies and Dilemmas. J Clin Med [Internet]. 2022 Mar 31;11(7):1951. Available from: https://www.mdpi.com/2077-0383/11/7/1951

137. Lazari D, Freitas Leal JK, Brock R, Bosman G. The Relationship Between Aggregation and Deformability of Red Blood Cells in Health and Disease. Front Physiol [Internet]. 2020 Apr 15 [cited 2022 Feb 9];11:288. Available from: /pmc/articles/PMC7174766/

138. Tunçez A, Çetin MS, Çetin EHÖ, Yilmaz S, Korkmaz A, Uçar FM. Association between RDW and stent thrombosis in patients with ST-elevation myocardial infarction undergoing primary percutaneous coronary intervention. Medicine [Internet]. 2017 Feb 1 [cited 2022 Mar 14];96(5). Available from: /pmc/articles/PMC5293455/

139. Simmonds MJ, Meiselman HJ. Prediction of the level and duration of shear stress exposure that induces subhemolytic damage to erythrocytes. Biorheology. 2016 Jan 1;53(5–6):237–49.

140. Cahalan SM, Lukacs V, Ranade SS, Chien S, Bandell M, Patapoutian A. Piezo1 links mechanical forces to red blood cell volume. Elife [Internet]. 2015 May 22 [cited 2023 Mar 5];4(MAY). Available from: /pmc/articles/PMC4456639/

141. Straat M, van Bruggen R, de Korte D, Juffermans NP. Red Blood Cell Clearance in Inflammation. Transfusion Medicine and Hemotherapy [Internet]. 2012 Oct [cited 2022 Feb 9];39(5):353. Available from: /pmc/articles/PMC3678279/

142. Baskurt OK. In vivo correlates of altered blood rheology. Biorheology. 2008 Jan 1;45(6):629–38.

143. Messmer K, H, Schmid-Schonbein. Hemodilution: Theoretical Basic and Clinical Application by Messmer, K. & H. Schmid-Schonbein; editors: Very Good Hard Cover (1972) First Edition. | Bookworks [MWABA, IOBA] [Internet]. [cited 2023 Nov 4]. Available from: https://www.abebooks.com/first-edition/Hemodilution-Theoretical-Basic-Clinical-Application-Messmer/1403687320/bd

144. Ohta M, Wetzel SG, Dantan P, Bachelet C, Lovblad KO, Yilmaz H, et al. Rheological changes after stenting of a cerebral aneurysm: A finite element modeling approach. Cardiovasc Intervent Radiol. 2005;28(6):768–72.

145. Baskurt OK, Meiselman HJ. Blood rheology and hemodynamics. undefined. 2003 Oct;29(5):435–50.

146. Chen RYZ, Carlin RC, Simchon S, Jan KM, Chien S. Effects of dextran-induced hyperviscosity on regional blood flow and hemodynamics in dogs. https://doi.org/101152/ajpheart19892563H898 [Internet]. 1989 [cited 2023 Mar 5];256(3). Available from: https://journals.physiology.org/doi/10.1152/ajpheart.1989.256.3.H898

147. Tscharre M, Lee S, Kopp CW, Panzer S, Gremmel T. Mean Corpuscular Volume Predicts Adverse Outcomes Following Peripheral Angioplasty With Stenting and Is Associated With On-Treatment Platelet Reactivity. Angiology. 2021 Jan 1;72(1):16–23.

148. Vijayan S, Barmby DS, Pearson IR, Davies AG, Wheatcroft SB, Sivananthan M. Assessing Coronary Blood Flow Physiology in the Cardiac Catheterisation Laboratory. Curr Cardiol Rev. 2017;13(3):232–43.

149. Goodwill AG, Dick GM, Kiel AM, Tune JD. Regulation of Coronary Blood Flow HHS Public Access. Compr Physiol [Internet]. 2018;7(2):321–82. Available from: https://www.ncbi.nlm.nih.gov/pmc/articles/PMC5966026/pdf/nihms966471.pdf

150. Systems Inc T. T400-Series Surgical Protocol Volume Flow Rat & Mouse Carotid Artery: Acute Blood Flow Measurement APPLICATION BASICS.

151. Oyre S, Ringgaard S, Kozerke S, Paaske WP, Erlandsen M, Boesiger P, et al. Accurate Noninvasive Quantitation of Blood Flow, Cross-Sectional Lumen Vessel Area and Wall Shear Stress by Three-Dimensional Paraboloid Modeling of Magnetic Resonance Imaging Velocity Data. 1998;

152. Panteleev MA, Korin N, Koen |, Reesink D, David |, Bark L, et al. Wall shear rates in human and mouse arteries: Standardization of hemodynamics for in vitro blood flow assays: Communication from the ISTH SSC subcommittee on biorheology. 2020;

153. Cheng C, Helderman F, Tempel D, Segers D, Hierck B, Poelmann R, et al. Large variations in absolute wall shear stress levels within one species and between species. Atherosclerosis. 2007;195:225–35.

154. Cho DH, Aguayo S, Cartagena-Rivera AX. Atomic force microscopy-mediated mechanobiological profiling of complex human tissues. Biomaterials. 2023;303(October):122389.

155. Stylianou A, Kontomaris SV, Grant C, Alexandratou E. Atomic Force Microscopy on Biological Materials Related to Pathological Conditions. Scanning [Internet]. 2019 [cited 2025 Mar 23];2019:8452851. Available from: https://pmc.ncbi.nlm.nih.gov/articles/PMC6535871/

156. Gibson CT. Atomic force microscopy applied to biological systems: Novel applications and advanced experimental methods. Comprehensive Nanoscience and Nanotechnology. 2019 Jan 1;1–5:83–104.

157. Technologies Inc S. RosetteSepTM Human Total Lymphocyte Enrichment Cocktail. 2018;

158. SepMateTM PBMC Isolation Tubes [Internet]. [cited 2025 Feb 6]. Available from: https://www.stemcell.com/products/brands/sepmate-pbmc-isolation.html

159. Wei L, Leo HL, Chen Q, Li Z. Structural and Hemodynamic Analyses of Different Stent Structures in Curved and Stenotic Coronary Artery. Front Bioeng Biotechnol [Internet]. 2019 Dec 6 [cited 2025 Mar 8];7:366. Available from: https://pmc.ncbi.nlm.nih.gov/articles/PMC6908811/

160. Forouzandeh F, Fatouraee N. Effects of Cardiac Motion on the Flow Rate of the Left Coronary Artery Considering Different Blood Viscosities. 2017 24th Iranian Conference on Biomedical Engineering and 2017 2nd International Iranian Conference on Biomedical Engineering, ICBME 2017. 2018 Aug 8;

161. Johnson K, Sharma P, Oshinski J. Coronary Artery Flow Measurement Using Navigator Echo Gated Phase Contrast Magnetic Resonance Velocity Mapping at 3.0 Tesla. J Biomech. 2008;41(3):595.

162. Shin S, Yang Y, Suh JS. Measurement of erythrocyte aggregation in a microchip stirring system by light transmission. Clin Hemorheol Microcirc. 2009;41(3):197–207.

163. Shin S, Hou JX, Suh JS, Singh M. Validation and application of a microfluidic ektacytometer (RheoScan-D) in measuring erythrocyte deformability. Clin Hemorheol Microcirc. 2007;37(4):319–28.

164. Gómez-De-Mariscal E, Guerrero V, Sneider A, Jayatilaka H, Phillip JM, Wirtz D, et al. Use of the p-values as a size-dependent function to address practical differences when analyzing large datasets. Scientific Reports | [Internet]. 123AD [cited 2025 Mar 9];11:20942. Available from: www.nature.com/scientificreports

165. Sherwood JM, Kaliviotis E, Dusting J, Balabani S. Hematocrit, viscosity and velocity distributions of aggregating and non-aggregating blood in a bifurcating microchannel. Biomech Model

Mechanobiol [Internet]. 2014 [cited 2025 Mar 9];13(2):259–73. Available from: https://pubmed.ncbi.nlm.nih.gov/23114881/

166. Connes P, Uyuklu M, Tripette J, Boucher JH, Beltan E, Chalabi T, et al. Sampling time after tourniquet removal affects erythrocyte deformability and aggregation measurements. Clin Hemorheol Microcirc. 2009;41(1):9–15.

167. Lazari D, Freitas Leal JK, Brock R, Bosman G. The Relationship Between Aggregation and Deformability of Red Blood Cells in Health and Disease. Front Physiol. 2020 Apr 15;11:288.

168. Budzianowski J, Pieszko K, Burchardt P, Rzeźniczak J, Hiczkiewicz J. The Role of Hematological Indices in Patients with Acute Coronary Syndrome. Dis Markers. 2017;2017:3041565.

169. Grygorczyk R, Orlov SN. Effects of hypoxia on erythrocyte membrane properties-Implications for intravascular hemolysis and purinergic control of blood flow. Front Physiol. 2017 Dec 22;8(DEC).

170. Suresh S, Rajvanshi PK, Noguchi CT. The Many Facets of Erythropoietin Physiologic and Metabolic Response. Front Physiol. 2020 Jan 17;10:497186.

171. Wiegmann L, de Zélicourt DA, Speer O, Muller A, Goede JS, Seifert B, et al. Influence of standard laboratory procedures on measures of erythrocyte damage. Front Physiol. 2017;8(SEP).

172. Meram E, Yilmaz BD, Bas C, Atac N, Yalcin O, Meiselman HJ. Shear stress-induced improvement of red blood cell deformability. Biorheology. 2013;50(3–4):165–76.

173. Simmonds MJ, Atac N, Baskurt OK, Meiselman HJ, Yalcin O. Erythrocyte deformability responses to intermittent and continuous subhemolytic shear stress. Biorheology. 2014 Jan 1;51(2–3):171–85.

174. Cluitmans JCA, Hardeman MR, Dinkla S, Brock R, Bosman GJCGM. Red blood cell deformability during storage: Towards functional

proteomics and metabolomics in the Blood Bank. Blood Transfusion. 2012;10(SUPPL. 2).

175. Baskurt OK, Meiselman HJ. RBC aggregation: More important than RBC adhesion to endothelial cells as a determinant of in vivo blood flow in health and disease. Microcirculation. 2008;15(7):585–90.

176. Cokelet GR, Goldsmith HL. Decreased hydrodynamic resistance in the two-phase flow of blood through small vertical tubes at low flow rates. Circ Res. 1991;68(1):1–17.

177. Knisely MH. Intravascular erythrocyte aggregation (blood sludge). In: Handbook of Physiology, Section 2: Circulation, Volume III. American Physiological Society; 1965. p. 2249–92.

178. Sherwood JMJM, Kaliviotis E, Dusting J, Balabani S. Hematocrit, viscosity and velocity distributions of aggregating and non-aggregating blood in a bifurcating microchannel. Biomech Model Mechanobiol. 2014;13(2):259–73.

179. Michel JB, Martin-Ventura JL. Red blood cells and hemoglobin in human atherosclerosis and related arterial diseases. Int J Mol Sci. 2020;21(18):1–20.

180. Benard N, Perrault R, Coisne D. Computational approach to estimating the effects of blood properties on changes in intra-stent flow. Ann Biomed Eng. 2006;34(8):1259–71.

181. Rikhtegar F, Wyss C, Stok KS, Poulikakos D, Müller R, Kurtcuoglu V. Hemodynamics in coronary arteries with overlapping stents. J Biomech. 2014 Jan 22;47(2):505–11.

182. Sherwood JM, Dusting J, Kaliviotis E, Balabani S. The effect of red blood cell aggregation on velocity and cell-depleted layer characteristics of blood in a bifurcating microchannel. Biomicrofluidics [Internet]. 2012 Apr 26 [cited 2025 Mar 9];6(2). Available from: /aip/bmf/article/6/2/024119/924990/The-effect-of-red-blood-cell-aggregation-on

183. Zeltser D, Rogowski O, Berliner S, Mardi T, Justo D, Serov J, et al. Sex differences in the expression of haemorheological determinants in individuals with atherothrombotic risk factors and in apparently healthy people. Heart. 2004;90(3):277–81.

184. Zhao Y, Zang G, Yin T, Ma X, Zhou L, Wu L, et al. A novel mechanism of inhibiting in-stent restenosis with arsenic trioxide drug-eluting stent: Enhancing contractile phenotype of vascular smooth muscle cells via YAP pathway. Bioact Mater [Internet]. 2021 Feb 1 [cited 2025 Nov 30];6(2):375–85. Available from: https://www.sciencedirect.com/science/article/pii/S2452199X20301912?via%3Dihub

185. Timashev PS, Kotova SL, Belkova G V, Gubar'kova E V, Timofeeva LB, Gladkova ND, et al. Atomic Force Microscopy Study of Atherosclerosis Progression in Arterial Walls. Microsc Microanal [Internet]. 2016 [cited 2025 Nov 30];22:311–25. Available from: https://academic.oup.com/mam/article/22/2/311/6896758

APPENDIX

Appendix I: *In vivo*- Results

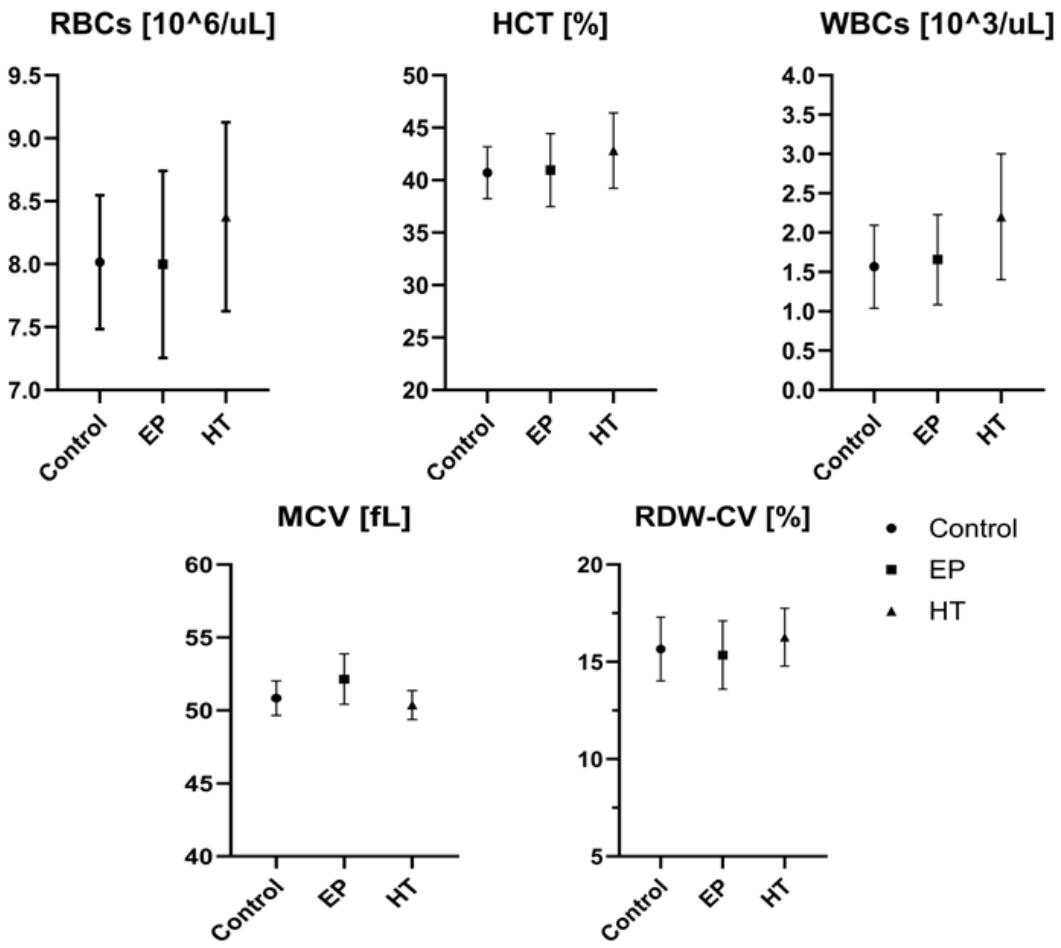

Figure Appendix I.1: Effect of different surface treatment stenting (EP, HT) on hematological parameters.

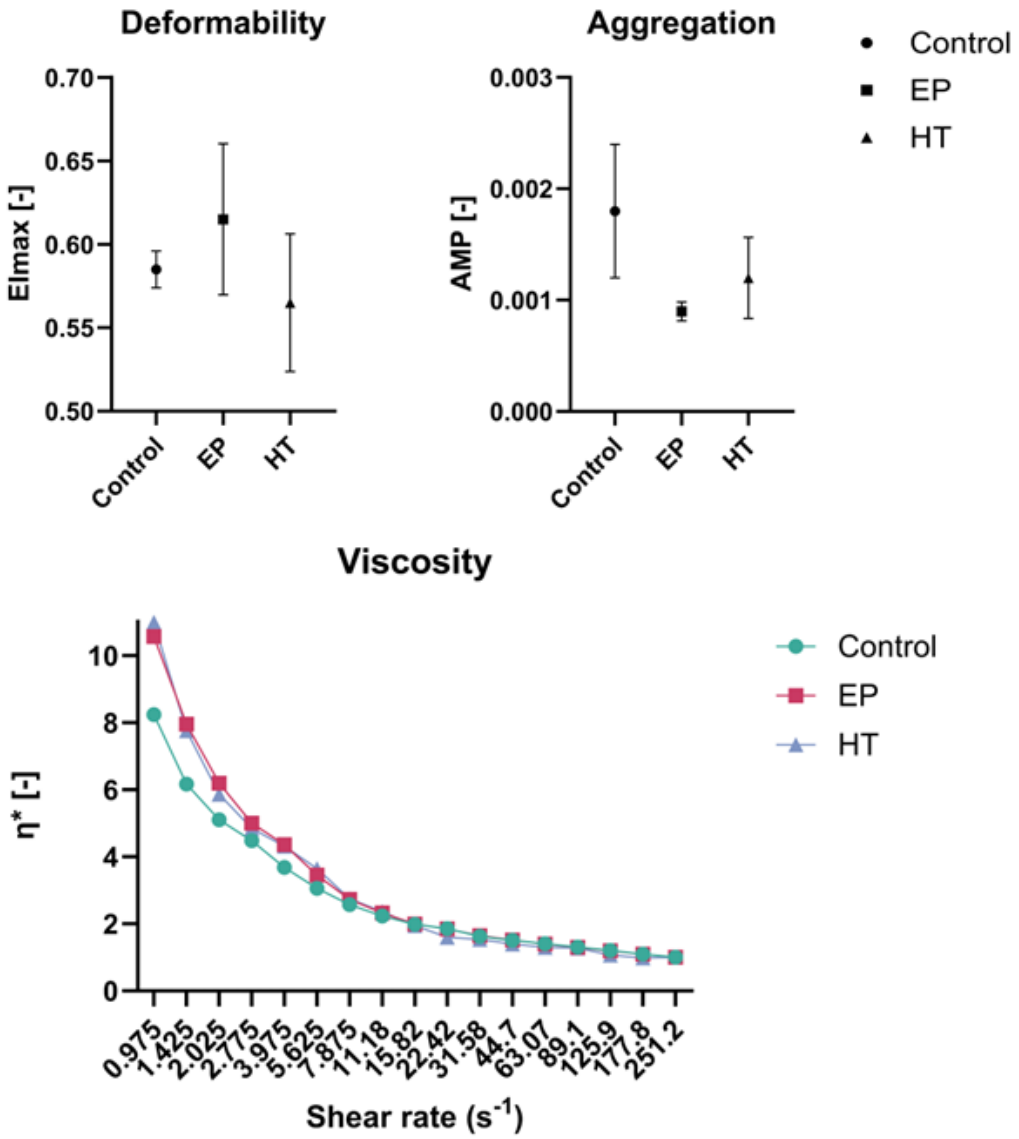

Figure Appendix I.2: Effect of different surface treatment stenting (EP, HT) in RBC aggregation, deformability and normalised viscosity η* against shear rate.

Appendix II: *In vivo*: Lymphocytes - Results

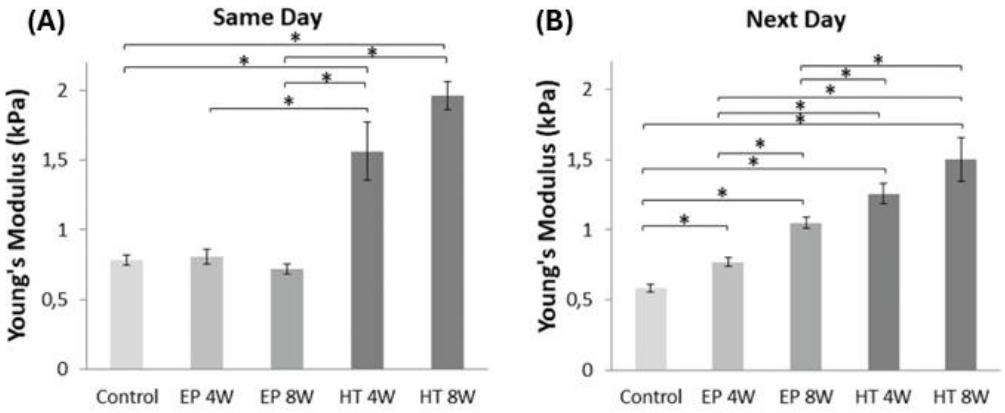

Figure Appendix II.1:Lymphocyte elasticity expressed in Young's modulus values (kPa). (A) Control vs stented ApoE and CD1 mice (same day and 24 h after isolation). (B, C) Normal vs corroded stented CD1 mice, same and next day measurements, respectively (* indicates $p < 0.05$).

Appendix III: *In vitro*-Results

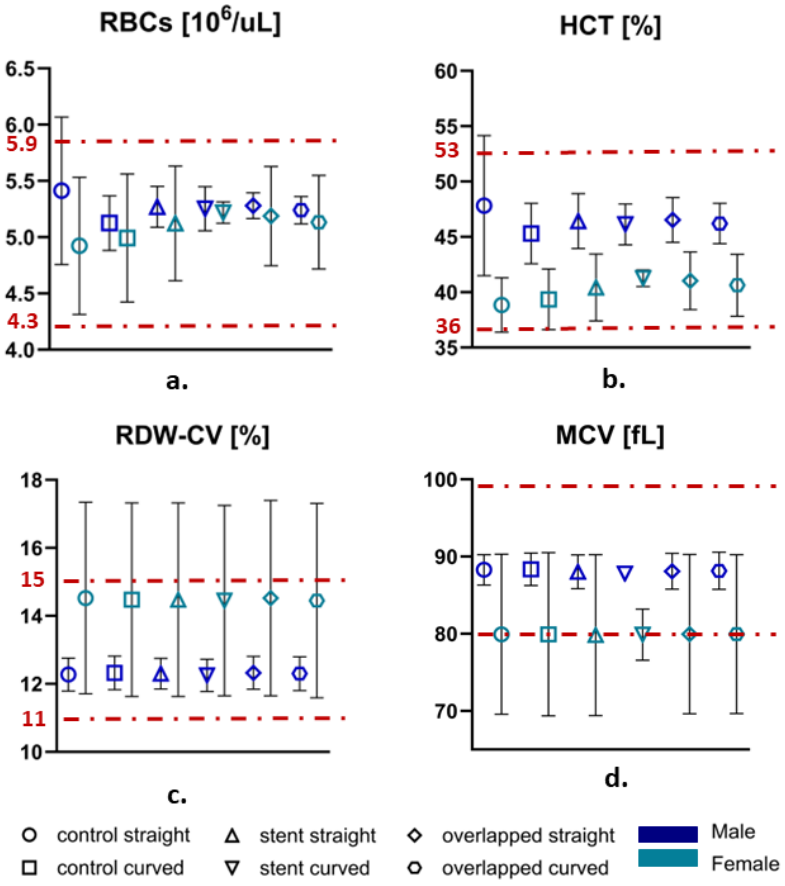

Figure Appendix III. 1: Impact of stenting on various hematological parameters across different experimental groups (female vs. male). The panels represent: (a) red blood cell (RBC) count, (b) hematocrit, (c) red cell distribution width (RDW), and (d) mean corpuscular volume (MCV). Data are presented as mean ± standard deviation (SD). Red dashed lines indicate the physiological reference range for each parameter.

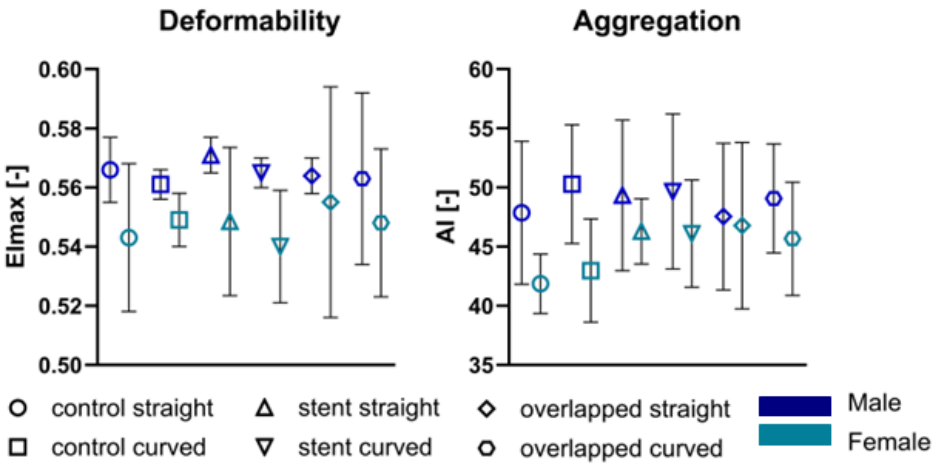

Figure Appendix III. 2: Effect of different experimental setups on red blood cell (RBC) deformability and aggregation in male and female groups.

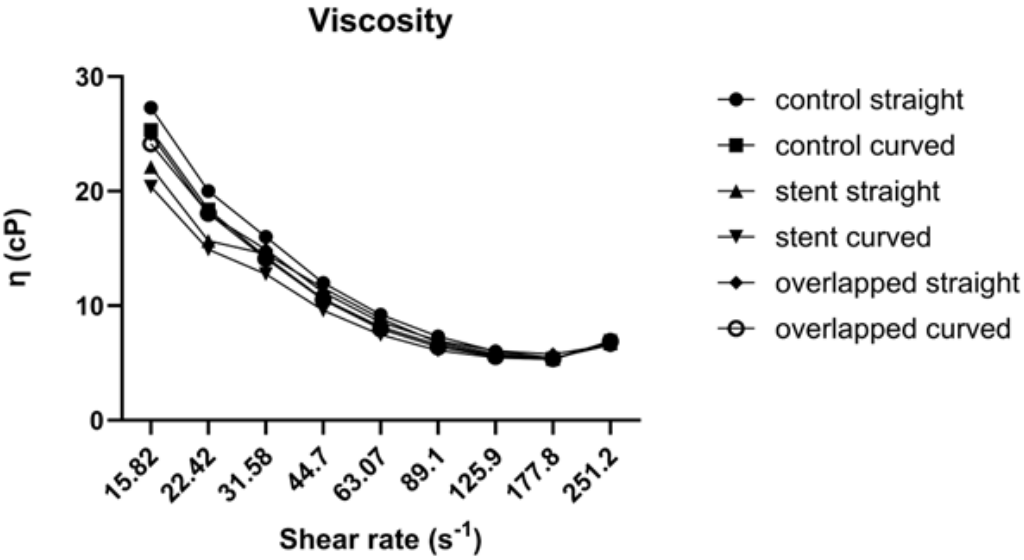

Figure Appendix III. 3:Viscosity (η) against different shear rate (s^{-1}) across different experimental conditions.

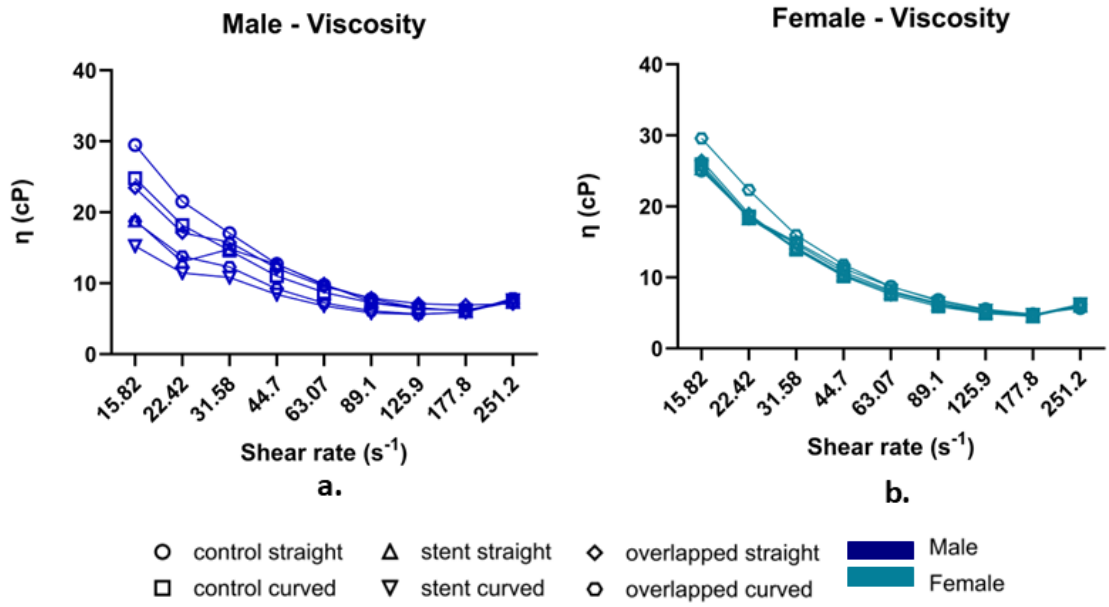

Figure Appendix III. 4: Viscosity (η) against shear rate (s^{-1}) for male (a) and female (b) across different experimental conditions. The results for each gender are shown in panels (a) and (b), respectively.

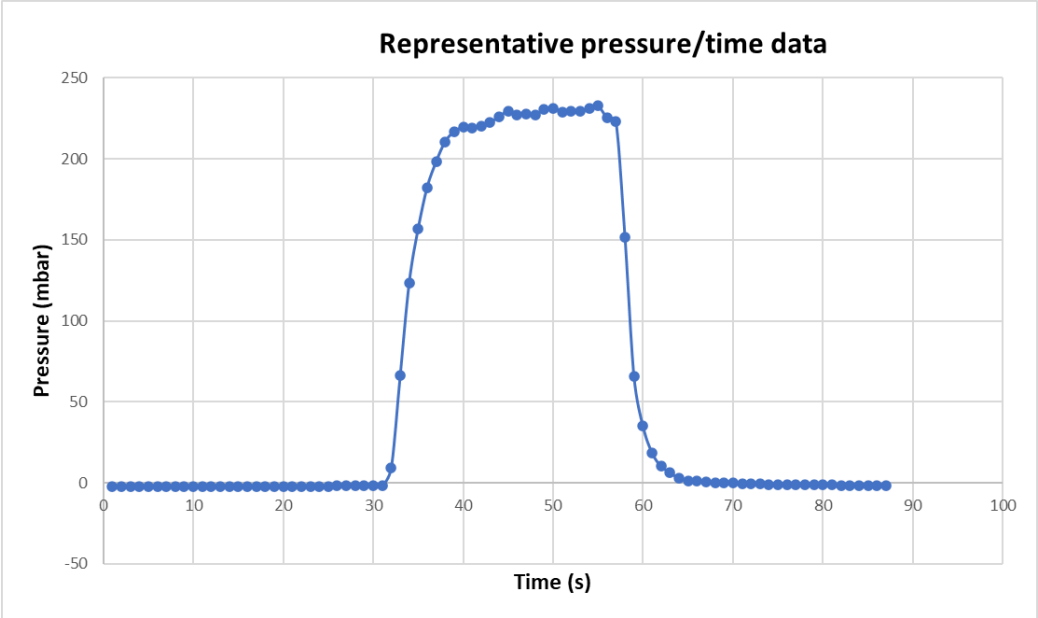

Figure Appendix III. 5: Representative pressure/time data for the single mode.

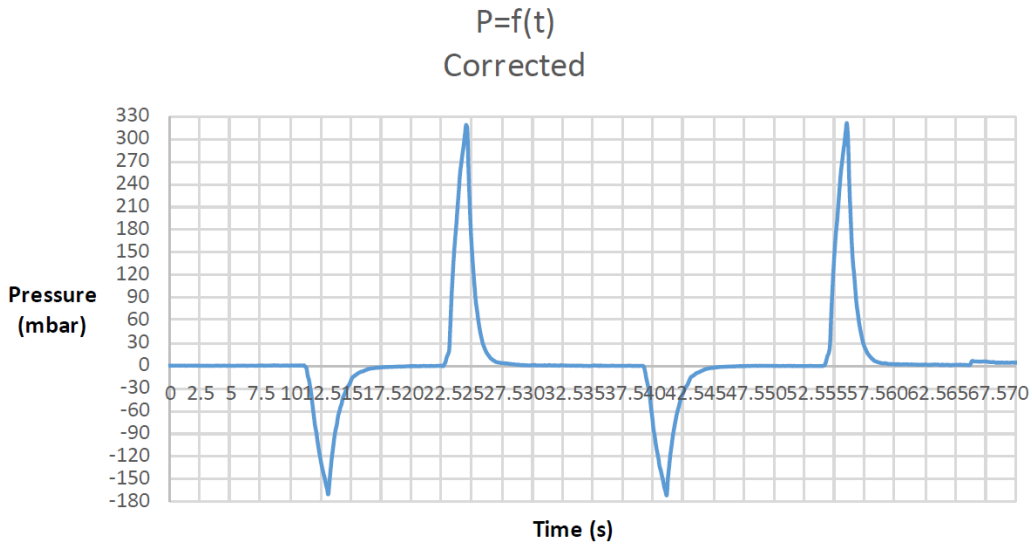

Figure Appendix III. 6 Representative pressure/time data for the quadruple mode.